Determination of hadron emitter radii in Z^0 decays to hadrons at LEP

Marcin Kucharczyk

Henryk Niewodniczański Institute of Nuclear Physics,
Polish Academy of Sciences,
Cracow, Poland

A thesis submitted for the Doctor of Philosophy degree
prepared under the supervision of Assoc. Prof. Tadeusz Lesiak

Cracow, February 2005

Abstract

The present thesis concerns the studies on the Bose-Einstein correlations for pions and Fermi-Dirac correlations for antiprotons and protons. The spatial transverse radius of the pion source was determined at $R_\perp = 0.591 \pm 0.015(stat) \pm 0.034(syst)$ fm, while the source radius for antiprotons at $R = 0.16 \pm 0.04(stat) \pm 0.03(syst)$ fm. The measurements under consideration were performed using data collected by the DELPHI experiment at LEP. The results of both the author's analyses and other LEP studies established strong dependence of the correlation radius on hadron rest mass. The correlation radii for pions, kaons, protons and Λ hyperons were estimated on the basis of correlation functions, which were determined within the model by A. Białas and K. Zalewski describing the above dependence. Predictions of the model proved to be consistent with the experimental results.

Streszczenie

W rozprawie przedstawiono wyniki doświadczalnych badań korelacji Bosego-Einsteina dla par naładowanych mezonów π oraz korelacji Fermiego-Diraca dla par antyprotonów i protonów, uzyskując wartość poprzecznego promienia korelacji dla pionów $R_\perp = 0.591 \pm 0.015(stat) \pm 0.034(syst)$ fm oraz wartość promienia korelacji dla antyprotonów $R = 0.16 \pm 0.04(stat) \pm 0.03(syst)$ fm. Pomiary wykonano w oparciu o dane zebrane przez eksperyment DELPHI pracujący przy akceleratorze LEP. Otrzymane rezultaty, wraz z wynikami uzyskanymi przez inne współprace LEP, potwierdzają silną zależność promienia korelacji od masy spoczynkowej hadronów. W ramach zaproponowanego przez A. Białasa i K. Zalewskiego modelu opisującego powyższą zależność wyznaczono funkcje korelacji, na podstawie których oszacowano promienie korelacji dla pionów, kaonów, protonów i hiperonów Λ. Stwierdzono zgodność wyników eksperymentalnych z przewidywaniami modelu.

Contents

Chapter 1

Introduction

Many aspects of multiparticle production are still practically unknown even though they have been studied for forty years. Among them we may count the space-time properties of the hadron emission volume. The Hanbury Brown-Twiss (HBT) intensity interferometry is the only available source of information on these properties in particle physics experiments. It relies on quantum interference effect between indistinguishable particles emitted by a finite-size source. The interference results in correlations between their four-momenta. In the case of bosons it is referred to as Bose-Einstein Correlations (BEC), while in the case of fermions as Fermi-Dirac Correlations (FDC). Both types of correlations are examined by measuring a two-particle correlation function, defined as a ratio of the inclusive density distribution for two particles and the so-called reference density. The latter is a two-particle density distribution which approximates the distribution without the BEC or FDC effects.

In particular, the HBT interferometry is applied in the analysis of hadron emitter radii in the process $e^+e^-\to Z^0\to$hadrons for pions, kaons, protons and Λ hyperons[1] using the data collected by four experiments (ALEPH, DELPHI, L3, OPAL) working at LEP storage ring. These studies have been described in chapter 4.

The results of one- and three-dimensional Bose-Einstein correlation radius analyses for pions suggest the longitudinal source elongation, i.e. the component of the correlation radius ($R_{||}$) longitudinal with respect to the thrust axis is greater than transversal one ($R_\perp$). Although the BEC effect for pions has been clearly established in the LEP data, the determined values of the correlation radius vary considerably amongst the experiments. The spread of the measured values indicates the occurrence of systematic errors related to the choice of the reference sample as well as to other details of the analyses. That is why the R_{BEC} determination using independent method seems to be crucial to verify an inequality $R_{||} > R_\perp$. A part of this thesis (chapter 6) is devoted to this kind of measurement performed by the author via analysis of the correlation function for two charged pions in the differences of their azimuthal angles, rapidities and transverse momentum magnitudes using data collected by the DELPHI experiment.

All available experimental results point to the hadron source radius of $\sim(0.5-1.0)$ fm[2] when measured by the Bose-Einstein interference of pions and kaons and the radius of $\sim(0.10-0.16)$ fm when measured by the Fermi-Dirac interference of Λ's (three results by ALEPH, DELPHI and OPAL) and protons (one result by OPAL). A new measurement

[1] Charge-conjugate modes are included everywhere, unless otherwise specified.

[2] 1 fm $= 10^{-15}$ m

of the correlation radius for protons performed by the author, as presented in this thesis (chapter 7), is based on the analysis of $\bar{p}\bar{p}$ and pp correlations in DELPHI data.

The above-mentioned significant decrease in the correlation radius with a particle rest mass is striking and no explanation has been provided so far. One of the approaches aiming at interpretation of the observed dependence of the correlation radius on the hadron mass is the quantum-mechanical model by A. Białas and K. Zalewski. The author of this thesis conducted studies on the above-mentioned model and compared its predictions to the LEP results (chapters 8 and 9).

The other parts of the thesis are organised in the following way: chapter 2 is devoted to the intensity interferomentry and the aspects of its application in particle physics. Chapter 3 gives an overview of the methodology used in BEC and FDC. Chapter 5 provides a short description of the LEP accelerator, DELPHI detector and the selection of data sample.

Chapter 2

Intensity interferometry

Intensity interferometry was developed in the 1950s by Hanbury Brown and Twiss (HBT interferometry) [1–3] as a method of measuring the angular diameters of then discovered bright radio-sources. At that time the only technique of determining diameters of distant sources was conventional Michelson interferometry (amplitude or phase interferometry) which was unsuitable to measure small diameters of radio-sources. Intensity interferometry relies on the observation that a pair of photons emitted independently from two different points on the source surface and observed in a separate pair of detectors is correlated due to a second order quantum interference effect. The shape of the intefrerence pattern in a function of the detector separation is directly related to the angular size of the emission region.

The approach proposed by Hanbury Brown and Twiss is nowadays also applied in the studies on aspects of non-perturbative Quantum Chromodynamics (QCD) [4]. The analysis of the particle source features on the basis of the quantum interferometry constitutes the subject of the present thesis.

To illustrate how the above-mentioned method works, let us consider the following simple model [5]: two distant random point sources of light, a and b, with the same frequencies (Fig.2.1). The distance between the sources is denoted by R, while the distance between detectors by d. Suppose that the distance between the sources and detectors (L) is much larger than R and d. Assuming that bosons propagate as free particles after leaving the production area, source a produces a spherical electromagnetic wave with amplitude $\alpha e^{ik|\vec{r}-\vec{r_a}|+i\phi_a}/|\vec{r}-\vec{r_a}|$, and source b a wave with amplitude $\beta e^{ik|\vec{r}-\vec{r_b}|+i\phi_b}/|\vec{r}-\vec{r_b}|$, where ϕ_a and ϕ_b denote random phases. Total amplitudes in detectors 1 and 2 are:

$$A_1 = \frac{1}{L}(\alpha e^{ikr_{a1}+i\phi_a} + \beta e^{ikr_{b1}+i\phi_b}), \tag{2.1}$$

$$A_2 = \frac{1}{L}(\alpha e^{ikr_{a2}+i\phi_a} + \beta e^{ikr_{b2}+i\phi_b}), \tag{2.2}$$

where r_{a1} and r_{a2} represent distances between source a and detectors 1 and 2, while r_{b1} and r_{b2} are distances between source b and detectors 1 and 2. Total intensities at detectors 1 and 2 are as follows:

$$I_1 = \frac{1}{L^2}(|\alpha|^2 + |\beta|^2 + \alpha^*\beta e^{i[k(r_{b1}-r_{a1})+\phi_b-\phi_a]} + \alpha\beta^* e^{-i[k(r_{b1}-r_{a1})+\phi_b-\phi_a]}), \tag{2.3}$$

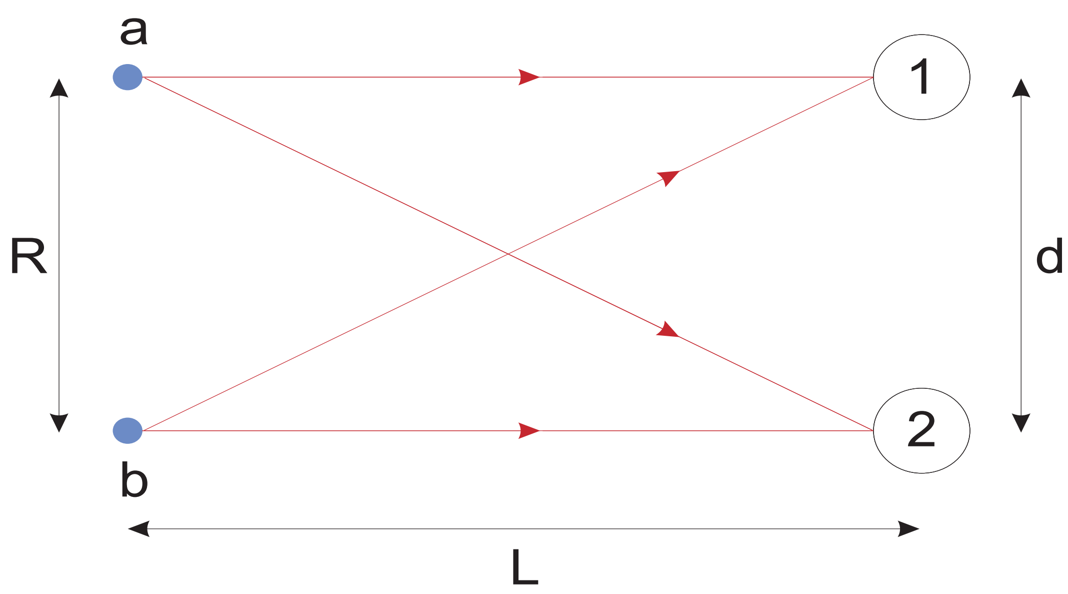

Figure 2.1: Scheme illustrating the principle of intensity interferometry. Arrows represent the emission of light from distant random sources **a** and **b**. Its intensity is measured in independent detectors **1** and **2**.

$$I_2 = \frac{1}{L^2}(|\alpha|^2 + |\beta|^2 + \alpha^*\beta e^{i[k(r_{b2}-r_{a2})+\phi_b-\phi_a]} + \alpha\beta^* e^{-i[k(r_{b2}-r_{a2})+\phi_b-\phi_a]}). \qquad (2.4)$$

After averaging over the phases the latter exponential factors go to zero. Therefore average intensities amount to:

$$\langle I_1 \rangle = \langle I_2 \rangle = \frac{1}{L^2}(\langle|\alpha|^2\rangle + \langle|\beta|^2\rangle). \qquad (2.5)$$

Thus, the product of the averaged intensities does not depend on the distance between detectors. The product $I_1 I_2$ includes an extra term $2(\alpha^*\beta)(\alpha\beta^*)\cos(k(r_{a1}-r_{a2}-r_{b1}+r_{b2}))$ which does not vanish when the average $\langle I_1 I_2 \rangle$ is calculated:

$$\langle I_1 I_2 \rangle = \langle I_1 \rangle \langle I_2 \rangle + \frac{2}{L^4}|\alpha|^2|\beta|^2 \cos(k(r_{a1} - r_{a2} - r_{b1} + r_{b2})). \qquad (2.6)$$

Thus the correlation function takes the following form:

$$C(d) = \frac{\langle I_1 I_2 \rangle}{\langle I_1 \rangle \langle I_2 \rangle} = 1 + 2\frac{\langle|\alpha|^2\rangle + \langle|\beta|^2\rangle}{(\langle|\alpha|^2\rangle + \langle|\beta|^2\rangle)^2}\cos(k(r_{a1} - r_{a2} - r_{b1} + r_{b2})). \qquad (2.7)$$

For $L \gg R$ the following approximation can be made: $k(r_{a1} - r_{a2} - r_{b1} + r_{b2}) \approx k\theta d$, where $\theta = R/L$ is the angular size of the source and θd is the wavelength of the light.

Angular size of the source can be estimated by varying the distance between detectors and studying respective wavevectors and the angle between the two sources.

2.1 Quantum statistics aspects of intensity interferometry

HBT effect in quantum mechanics is the result of the symmetrisation of the wave functions of bosons. The particles described by Bose-Einstein statistics can occupy the same quantum states: they can bunch in the phase-space. The phenomenon of an increased probability for the emission of identical bosons from close region of space-time is called the Bose-Einstein Correlation (BEC) effect.

Intensity interferometry was rediscovered and developed in particle physics in 1959 by G. Goldhaber et al. [6, 7]. They studied angular correlations of identically charged pions emerging from $p\bar{p}$ annihilation which are nearly at rest. The BEC enhancement at small opening angle of $\pi^+\pi^+$, $\pi^-\pi^-$ pairs was observed.

In the 1990s the intensity interferometry based on Fermi-Dirac statistics was also pursued. Two identical fermions cannot occupy the same quantum state because of the Pauli exclusion principle – they are described by the antisymmetric wave function. This fact manifests itself by the decrease of the probability of emission of identical fermions which are close in space-time and it is called the Fermi-Dirac Correlation (FDC) effect.

2.2 Bose-Einstein correlations

Let us consider a system of two identical bosons emitted from a source with three-momentum vectors $\vec{q_1}$ and $\vec{q_2}$ (the derivation presented below follows [6–8]). The second order correlation function is defined as:

$$C_2(\vec{q_1}, \vec{q_2}) = \frac{\mathcal{P}(\vec{q_1}, \vec{q_2})}{\mathcal{P}(\vec{q_1})\mathcal{P}(\vec{q_2})} = \frac{\mathcal{P}(\vec{q_1}, \vec{q_2})}{\mathcal{P}_{ref}(\vec{q_1}, \vec{q_2})}, \tag{2.8}$$

where $\mathcal{P}(\vec{q_1}, \vec{q_2})$ denotes the probability density distribution of two particles with momenta $\vec{q_1}$, $\vec{q_2}$, and $\mathcal{P}(\vec{q_1})$, $\mathcal{P}(\vec{q_2})$ represent probability density distributions of one particle with respective momentum $\vec{q_1}$ or $\vec{q_2}$. The denominator in formula (2.8) is usually replaced by certain two-particle density distribution $\mathcal{P}_{ref}$ which approximates the distribution without BEC.

Assume that the two identical bosons with three-momentum vectors $\vec{q_1}$, $\vec{q_2}$ are emitted from points $\vec{r_1}$ or $\vec{r_2}$ within the source area. A crucial fact underlying the BEC effect is the *chaoticity* or the *total incoherence* of the source, which means that the phases of wave function amplidudes describing the boson production fluctuate freely in every point of space. In this case all the phases can be fixed to zero. To simplify the description the plane wave function is taken into account where, in an incoherent case, the phase term disappears.

Hence the symmetrised coincidence amplitude of the observation of two bosons with momenta $\vec{q_1}$, $\vec{q_2}$ is given as follows (upper index s refers to the symmetrisation):

$$\psi^s_{1,2}(\vec{r_1}, \vec{r_2}; \vec{q_1}, \vec{q_2}) = \frac{1}{\sqrt{2}}\Big(\psi_{11}\psi_{22} + \psi_{12}\psi_{21}\Big), \tag{2.9}$$

where ψ_{ij} denotes the plane wave function for a boson produced at point $\vec{r_j}$ $(j = 1, 2)$ and observed with momentum $\vec{q_i}$ $(i = 1, 2)$.
Thus the probability density of the observation of two bosons with momenta $\vec{q_1}$, $\vec{q_2}$ is:

$$|\psi^s_{1,2}|^2 = 1 + e^{i(\vec{q_1} - \vec{q_2})(\vec{r_1} - \vec{r_2})} = 1 + \cos[\Delta\vec{q}(\vec{r_1} - \vec{r_2})], \tag{2.10}$$

where $\Delta\vec{q} = \vec{q_1} - \vec{q_2}$.

Assuming the spherically symmetric spatial distribution of the particle sources, $\rho(\vec{r})$, the total probability of observing a particle with momentum $\vec{q}$ emitted from point $\vec{r}$ is defined as:

$$\mathcal{P}(\vec{q}) = \int |\rho(\vec{r})|^2 d^3\vec{r}. \tag{2.11}$$

The probability of detecting a particle emitted from point $\vec{r_1}$ with momentum $\vec{q_1}$ and another, emitted from point $\vec{r_2}$ with momentum $\vec{q_2}$ can be expressed by the following formula:

$$\mathcal{P}(\vec{q_1}, \vec{q_2}) = \int |\psi^s_{1,2}(\vec{r_1}, \vec{r_2}; \vec{q_1}, \vec{q_2})|^2 |\rho(\vec{r_1})|^2 |\rho(\vec{r_2})|^2 d^3\vec{r_1} d^3\vec{r_2}. \tag{2.12}$$

On the condition that the emission is completely incoherent, the phases in $|\psi^s_{1,2}|^2$ drop out from formula (2.12).

Applying equations (2.10), (2.11) and (2.12) to formula (2.8) one can express the two particle correlation function as follows:

$$C_2(\vec{q_1}, \vec{q_2}) = 1 + \frac{\int \cos[\Delta\vec{q}(\vec{r_1} - \vec{r_2})] |\rho(\vec{r_1})|^2 |\rho(\vec{r_2})|^2 d^3\vec{r_1} d^3\vec{r_2}}{\mathcal{P}(\vec{q_1})\mathcal{P}(\vec{q_2})}. \tag{2.13}$$

The Fourier transformation of the above formula gives:

$$C_2(\Delta\vec{q}) = 1 + |\tilde{\rho}(\Delta\vec{q})|^2, \tag{2.14}$$

where

$$\tilde{\rho}(\Delta\vec{q}) = \int \rho(\vec{r}) e^{-i\vec{r}\Delta\vec{q}} d\vec{r} \tag{2.15}$$

is the Fourier transform of $\rho(\vec{r})$. For momenta measured in the two-boson rest frame the momentum difference $\Delta\vec{q}$ may be replaced by the four-momentum difference

$$Q = \sqrt{-(q_1 - q_2)^2} \equiv \sqrt{M^2 - 4\mu^2}, \tag{2.16}$$

a variable traditionally employed in the BEC effect studies, where M represents the two boson invariant mass, and μ denotes boson rest mass. Replacing $\Delta\vec{q}$ by Q in formulae (2.14) and (2.15) we get:

$$C_2(Q) = 1 + |\tilde{\rho}(Q)|^2, \qquad \tilde{\rho}(Q) = \int \rho(r) e^{-irQ} dr. \tag{2.17}$$

Assume now that the source is described by the Gaussian density distribution of emitting centres:

$$\rho(r) = \rho(0) e^{-\frac{r^2}{2R^2}}, \tag{2.18}$$

where $\rho(0) = 1/(4\pi^2 R^2)$ and R (in GeV^{-1})[1] indicate the radius of the sphere describing the source shape. Following the formulae (2.17) and (2.18) the correlation function assumes the form:

$$C_2(Q) = 1 + e^{-R^2 Q^2}. \tag{2.19}$$

In order to account for partial incoherence of the source an additional parameter is required. This parameter is called the chaoticity parameter and is denoted by λ. It can

[1]Unless otherwise stated, the natural unit system is employed, i.e. $\hbar = c = 1$. In particular, 1 GeV^{-1} = 0.197 fm.

vary from the value of 0, in the case of completely coherent source, to the value of 1 when the source is entirely chaotic.

In this way the final formula for the correlation function is expressed as:

$$C_2(Q) = N(1 + \lambda e^{-R^2Q^2}), \tag{2.20}$$

where the factor N accounts for normalisation.

The quality of experimental data influences to a great extent the strength of the BEC correlations, that is why parameter λ is also very often interpreted as the BEC strength parameter. R parameter can be considered as a geometrical radius of the spherical symmetric source of bosons.

2.3 Fermi-Dirac correlations

The total wave function describing indistinguishable fermions has to be antisymmetric with respect to the interchange of two of those fermions. The antisymmetrisation requirement for the total wave function of identical fermions yields the parametrisation of their correlation function:

$$C_2(Q) = N(1 - \lambda e^{-R^2Q^2}), \tag{2.21}$$

analogous to formula (2.20). Contrary to the Bose-Einsten analyses of two identical spinless bosons, in the Fermi-Dirac analysis not only spatial but also spin wave function have to be taken into account. Fermions have non-zero spin, therefore there are four possible states for each pair of spin-1/2 fermions. For large Q (and $l = 0$), there are no restrictions on the number of states. In the case of $Q \to 0$, the Fermi-Dirac statistics affected by the Pauli exclusion principle causes the decrease of the number of possible states to one: an asymmetric singlet state ($S = 0$). Let us consider the system of two identical spin-1/2 fermions emitted from an interaction region with four-momenta q_1 and q_2. The probability of the observation of the above system is related to the square of the total wave function $\Psi_{1,2}$ which contains two parts: the orbital wave function $\psi_{1,2}$ and the spin wave function. In the system of identical fermions the total wave function is required to be antisymmetric in the case of the interchange of two of those fermions. Assuming plane waves and a completely incoherent source with a spherical symmetric Gaussian density distribution, the probability densities of symmetric and antisymmetric orbital wave functions take the following forms:

$$|\psi^s_{1,2}|^2 = 1 + e^{-R^2Q^2}, \qquad |\psi^a_{1,2}|^2 = 1 - e^{-R^2Q^2}. \tag{2.22}$$

The Fermi-Dirac statistics causes the coupling between the symmetric orbital part of the two-fermion system ($|\psi^s_{1,2}|^2$) and the antisymmetric spin part ($S = 0$). On the other hand, the antisymmetric orbital part ($|\psi^a_{1,2}|^2$) implies the symmetric spin part ($S = 1$). On the assumption that $Q \to \infty$, the probability that the two-fermion system is in S state is proportional to $2S + 1$, therefore the probability density $|\Psi_{1,2}|^2$ is expressed by [9]:

$$|\Psi_{1,2}(Q)|^2 = \frac{1}{4}\Big[1 + e^{-R^2Q^2} + 3\Big(1 - e^{-R^2Q^2}\Big)\Big] = 1 - \frac{1}{2}e^{-R^2Q^2}. \tag{2.23}$$

On the basis of the above formula the 50% depletion of the correlation function value at $Q = 0$ limit may be expected.

2.4 Lund model and Bose-Einstein correlations

Since the hadronisation process is not perturbative, its properties are described by phenomenological models. One of the most succesful approaches is the Lund Model [10–12]. In order to describe the string fragmentation model let us consider a pair composed of quark and antiquark which are denoted by q and $\bar{q}$, respectively (cf Fig.2.2). When quark and antiquark propagate in opposite directions in the center-of-mass system of the pair, the energy of the colour field between them grows up. This enhancement is linear with increasing separation between the quarks. The colour field in this model is approximated by a homogeneous relativistic string, which is massless and characterised by the so-called string constant $\kappa \sim 1$ GeV. The energy density is proportional to the string length L:

$$E = \kappa L. \tag{2.24}$$

The end-points of the string represent q and $\bar{q}$, while the gluons are presumed to be transverse excitations of the string.

If the distance between quark (q_1) and antiquark ($\bar{q}_1$) grows, the potential energy accumulated in the string increases and the string may break up as a result of the production of another quark-antiquark pair ($q_2\bar{q}_2$) whose mass arises from the potential energy of the string. After the breakdown the emerging quarks start to separate and form two pairs ($q_1\bar{q}_2$) and ($q_2\bar{q}_1$) which are colour neutral and establish new end-points of the strings. If the invariant mass of the produced pairs is sufficient, subsequent partitions may follow.

Each meson is formed by a quark and antiquark being the outcome of adjacent string partitions (adjacent vertices (Fig.2.2)).

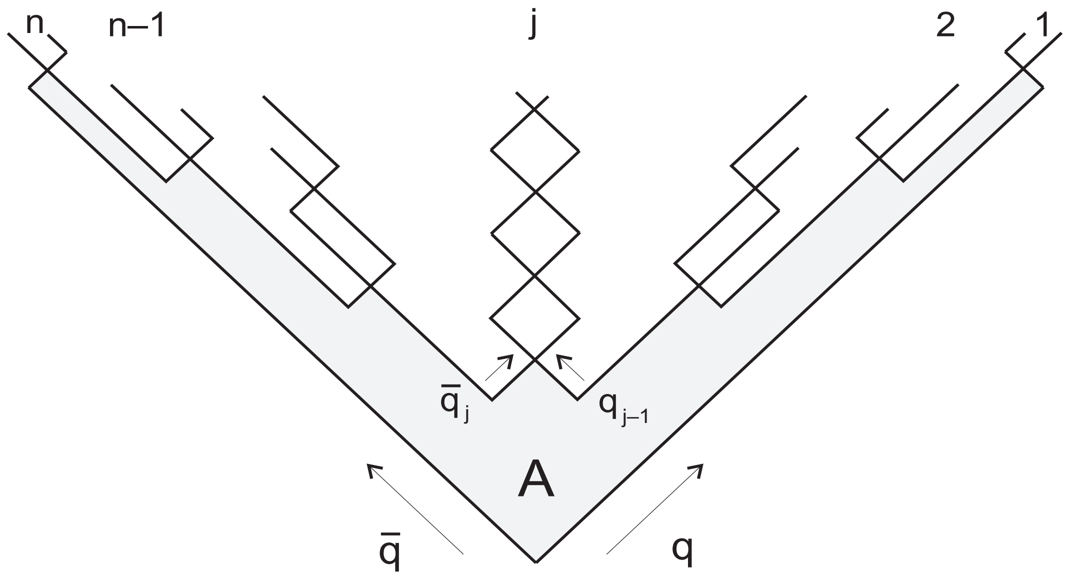

Figure 2.2: Space-time diagram of the Lund Model string decay.

In the colour-string model the probability for a string to decay into an n-particle state of distinguishable particles with energy-momenta $u_1, ..., u_n$ amounts to:

$$d\mathcal{P}(u_1, ..., u_n) = \left[\prod_{j=1}^{n} N du_j \delta(u_j^2 - m_j^2) \right] \delta \left(\sum_{j=1}^{n} u_j - U \right) \exp\left(-bA\right), \tag{2.25}$$

where A denotes the total space-time area of the break-up region [11], N corresponds to the mean multiplicity, b is the correlation length in rapidity and U is the total energy-momentum of the state.

A central assumption underlying this approach is that the probability amplitude of the event is proportional to:

$$\exp\left[(i\kappa - b/2)A\right], \tag{2.26}$$

hence the real part of the amplitude contributes the following factor to the probability of the process:

$$\exp(-bA), \tag{2.27}$$

The amplitude of producing n particles with given momenta can be expressed as the sum of all amplitudes differing only as far as the exchange of pair of identical particles is concerned. Thus the final state of n particles is described by $n!$ ways, which correspond to all different permutations of particles. Each permutation of identical particles results from changes in the break-up area, which cause modifications in the probability amplitude for the production process. The total amplitude may now be expressed in the following way:

$$\mathcal{M} = \sum_D \mathcal{M}_D, \tag{2.28}$$

where $\mathcal{M}_D$ is the amplitude corresponding to permutation D. The probability of a given final state is proportional to the square of the above symmetrised amplitude:

$$|\mathcal{M}|^2 = \sum_D |\mathcal{M}_D|^2 \omega_D, \tag{2.29}$$

where the weight factors are:

$$\omega_D = 1 + \sum_{D \neq D'} \frac{2Re(\mathcal{M}_D \mathcal{M}^*_D)}{|\mathcal{M}_D|^2 + |\mathcal{M}_{D'}|^2}. \tag{2.30}$$

In order to observe the effect of symmetrisation of the hadron production amplitude let us consider two identical bosons (1,2), where the state between them is denoted by I. The configurations of the production of the entire state are: $(..., 1, I, 2, ...)$ and $(..., 2, I, 1, ...)$ (Fig.2.3). It is clear that these configurations correspond to different space-time areas. Let us describe the break-up region corresponding to the first configuration by A_D and to the second by $A_{D'}$. Thus the area difference is:

$$\Delta A_{DD'} = A_D - A_{D'}. \tag{2.31}$$

The weight factors can be formulated as [13, 14]:

$$\omega_D = 1 + \sum_{D \neq D'} \frac{\cos \frac{\Delta A_{DD'}}{2\kappa}}{\cosh\left(\frac{b\Delta A_{DD'}}{2} + \frac{\Delta(\sum k_\perp^2)_{DD'}}{4\sigma^2}\right)}, \tag{2.32}$$

where the second component of the sum in denominator is the total probability of producing a parton with a transverse momentum $k_\perp$ and σ^2 is a constant of the order $\kappa/(2\pi)$. The first contribution to the sum in denominator is only important if the change of region A, going from permutation D to D', is comparable to b^{-1}. The $\Delta A_{DD'}$ vanishes with increasing four-momentum difference and the contribution to the weight, coming from the configuration D', disappears as the area $A_{DD'}$ expands. Thus, there is a contribution to the weight only when pairs with a small Δq and small Δx are exchanged.

In the Lund Model approach the correlation function is defined as the ratio between the two-particle probability density with (ρ_2^w) and without (ρ_2) BEC weights, correspondingly:

$$C_2(Q) = \frac{\rho_2^w(q_1, q_2)}{\rho_2(q_1, q_2)}. \tag{2.33}$$

It is worthwhile to note that this model, contrary to the description of the HBT correlations covered by previous sections, is not based on random phases or any explicit assumptions about incoherence. There is no rigorous proof of the assumed basic relation (2.26) but there are very strong arguments for its correctness [11–14].

The Bose-Einstein effect between identical bosons produced in hadronic interaction may not be easily included in the event generator programs for high-energy physics. The JETSET 7.3 PS generator [15], based on the Lund model dynamics and frequently used for the Z^0 decay, is constructed on the basis of classical stochastic processes. It produces a probability weight for an event with disregard for quantum mechanical effects.

The algorithm employed in the simulation of the BEC effect is implemented in the LUBOEI subroutine [16, 17]. It does not represent a true model and involves many assumptions. The Bose-Einstein effect is interpreted as an almost classical force, influencing the final state particles, rather than being a quantum mechanical phenomenon affecting the production amplitude. Therefore, the BEC algorithm implemented in the JETSET should be used cautiously and treated only as a first approximation of what the meaning of the Bose-Einstein effect may be.

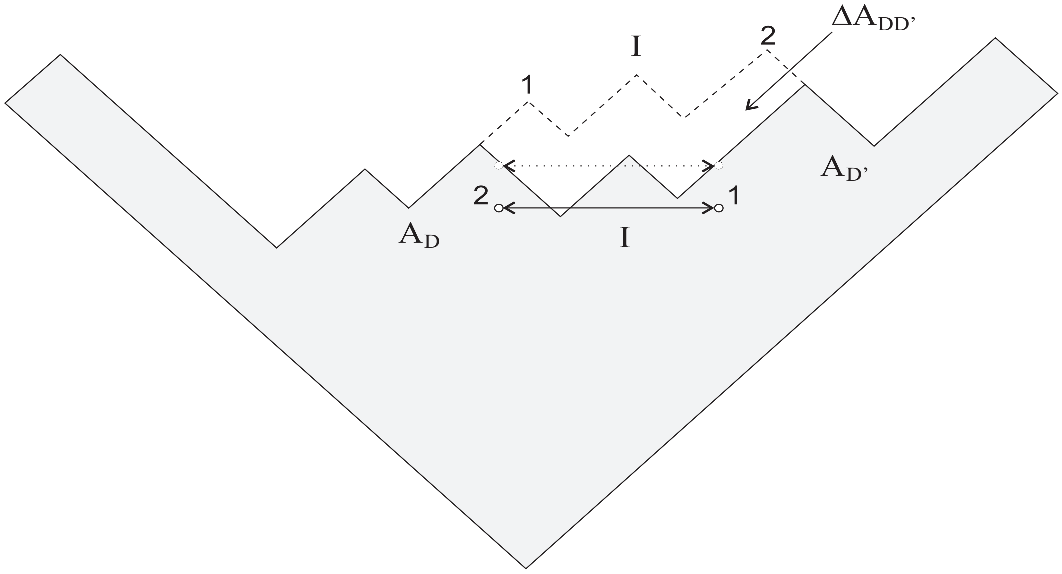

Figure 2.3: Space-time diagram explaining two possible ways of producing two identical bosons in the colour-string picture of the Lund model.

2.5 Field theory approach to the intensity interferometry

The models based on the field theory assume that the off-diagonal (two-particle distribution) and diagonal (one-particle distribution) terms of the single particle density matrix in the momentum representation correspond to the ratio of two-particle momentum distribution with and without quantum-mechanical interference.

Applying this approach, the so-called 'source function' S is constructed, which is related to the source density matrix in momentum space [18–20] by the Fourier transform [21–23]:

$$\rho(q, q') = \int d^4X e^{iQX} S(P, X), \tag{2.34}$$

where the source function $S(P, X)$ stands for a generalised Wigner function [19, 24], $P = (q + q')/2$, $Q = q - q'$ and q, q' denote particle four-momenta. $X = (x + x')/2$ is the variable related to the position of the source in space-time, where x and x' indicate the position four-vectors. In order to provide its physical interpretation, one can express the single-particle distribution in space coordinate (by analogy with the standard Wigner function) as follows:

$$\rho(X) \equiv \rho(\vec{x}, t) = \int d^4P S(P, X). \tag{2.35}$$

Formula (2.34) relates to the well-known formula based on the Wigner function $W(\vec{P}, \vec{X})$:

$$\rho(\vec{q}, \vec{q'}) = \int d^3\vec{X} e^{-i\vec{Q}\cdot\vec{X}} W(\vec{P}, \vec{X}). \tag{2.36}$$

Contrary to the standard Wigner function [25, 26], which relates to the particle wave functions at different position but at the same moment of time, the source function $S(P, X)$ describes the particle production amplitudes at different positions and different moments of time. Similarly to the standard Wigner function, one may give approximate derivation of the single-particle distribution in momentum and space-time on the basis of $S(P, X)$.

One of the possible realisations of the source function takes the form:

$$S(P, X) = W(\vec{P}, \vec{X})\delta(X = 0). \tag{2.37}$$

The source function in formula (2.37) describes only the situation when all particles are produced simultaneously at point $X = 0$.

Chapter 3

Methodology of studies on the intensity interferometry

The present chapter focuses on the choice of the so-called 'reference distribution', which is essential to the derivation of the correlation function. It also describes the specific construction of the reference frame which allows for the study of deviations from the Gaussian-symmetric shape of the particle emission region and its time evolution. Moreover, the chapter provides a short description of the corrections coming from the so-called 'long-range correlations' and final state interactions.

The quantum interference is usually analysed employing the variable defined as the difference between the two indistinguishable particle four-momenta Q (cf formula 2.16). By applying measured Q distributions it is feasible to construct the correlation function and estimate the correlation radius. The correlation function for two-particle correlations can be formulated as follows [27]:

$$C_2(Q) = \frac{\rho_2(Q)}{\rho_2(Q)^{REF}}, \tag{3.1}$$

where $\rho_2(Q)$ represents the inclusive density distribution of two particles with the four-momenta difference Q. The denominator in (3.1) is usually referred to as the reference sample, as it reflects approximately the distribution without the Bose-Einstein or Fermi-Dirac effects. However, the reference distribution should involve all possible correlations, except for those due to the Bose-Einstein or Fermi-Dirac ones. In particular, ρ_2^{REF} should encompass correlations which arise e.g. from the charge, energy-momentum or baryon number conservation, particle decays and event topology, present also in the numerator of (3.1). There is a number of different methods to obtain the reference sample. None of them is an ideal solution to the above requirement [28]. One way to construct the reference sample is based on experimental data itself, another uses Monte Carlo (MC) generators with full simulation of the experiment.

3.1 Overview of reference samples

The simplest reference sample frequently used in many analyses of the Bose-Einstein correlations for identically charged pion pairs ($\pi^{\pm}\pi^{\pm}$) is formed by unlike-sign charged pions. The main advantage of this approach is that the reference distribution is derived from the data sample, while the main disadvantage lies in the fact that the $\pi^{\pm}\pi^{\mp}$ pairs may also originate from resonances (with $\rho(770)$ giving a dominant contribution). Moreover, correlations arising from the attraction of opposite charges may also manifest themselves [29–31]. Another crucial problem rests in the choice of the normalisation point for the data far away from the interference region.

The second approach applied for the construction of the reference sample is to employ the Monte Carlo simulated distribution without the BEC or FDC effects. In this case the crucial requirement concerns an acceptable agreement between data and Monte Carlo samples in distributions of crucial variables such as particle momenta or opening angle of the pair. Moreover, the absence of the Coulomb effects in generators based on the Lund model may impinge on the correctness of this method. In addition, no spin effects are simulated. Hence the Monte Carlo reference sample should be treated cautiously.

Another method, used to produce the so-called 'event-mixing' reference sample, is based on the choice of two identical hadrons, each originating from a different data event [28] considered in the thrust reference frame, which naturally does not contain the BEC or FDC effects. The thrust reference frame is defined as follows: the z axis is oriented along the thrust axis [32], the x axis is perpendicular to both the thrust axis and z axis in the laboratory frame, and $\hat{y} = \hat{z} \times \hat{x}$. The main drawback of the event-mixing method lies in the fact that not only the BEC or FDC effect is removed from the data sample but many other correlations can be eliminated in this way. Instead of choosing two identical hadrons, each originating from a different event, one may split each event into two hemispheres along the plane perpendicular to the sphericity [32] or the thrust axis. Then the reference sample is obtained by constructing identical hadron pairs where each hadron belongs to a different hemisphere. In this kind of approach the problem of event rotation, present in the event-mixing method, no longer exists. These two procedures may be suitable only for the analysis of low energy data where the distribution of particles is more or less isotropic. In the case of higher energies, the particles form jets, therefore the event-mixing technique or the method based on drawing the tracks from different hemispheres can only be applicable in two-jets events where the mixing takes place between two events with a similar thrust axis orientation.

As regards the reference distributions derived from the data (the unlike and event-mixed distributions), the so-called 'double ratio' is generally used to account for imperfections in the reference distribution:

$$R(Q) = \frac{\rho_2(Q)^{data}}{\rho_2(Q)^{ref,data}} \Bigg/ \frac{\rho_2(Q)^{MC}}{\rho_2(Q)^{ref,MC}}, \tag{3.2}$$

where $\rho_2(Q)^{data}$, $\rho_2(Q)^{MC}$ indicate the Q distributions for the data and MC respectively, $\rho_2(Q)^{ref,data}$, $\rho_2(Q)^{ref,MC}$ denote the unlike or event-mixed Q distributions for the data and MC, correspondingly.

3.2 Effects of Bose-Einstein and Fermi-Dirac correlations in two and three dimensions

In most of the HBT interferometry analyses it is assumed that the source shape is a sphere with a Gaussian density distribution. The possibility that space-time evolution of the hadron emission region may differ from a sphere is covered by the analyses of the BEC or FDC phenomena in more than one dimension [33, 34]. To probe the shape of a particle source the BEC or FDC correlations have to be studied in terms of the components of the particles' four-vector momenta difference. The decomposition of the above variable is frequently performed using the so-called Longitudinal Centre-of-Mass System (LCMS) [13, 14, 35].

LCMS is defined for each pair of particles as a system where the sum of three-vector momenta of two particles is orthogonal to the reference axis (Fig.3.1), which is the axis of the physical process, for example the direction of the corresponding jet in the e^+e^- annihilation or the thrust axis. The two-particle system is then rotated in the plane perpendicular to the $\vec{q_1}+\vec{q_2}$ until the sum of longitudinal components of three-vector momenta amounts to zero. In this coordinate system the variable $\vec{Q} = \vec{q_1} - \vec{q_2}$ is decomposed into three parts Q_{long}, $Q_{t,out}$ and $Q_{t,side}$. The component $Q_{long} \equiv Q_z$ is parallel to the reference axis and $Q_{t,out}$ is parallel to the axis collinear with the sum of the paricles' three-vector momenta. $Q_{t,side}$ is perpendicular to both Q_{long} and $Q_{t,side}$.

An important feature of the LCMS frame is that the projection of the total three-vector momentum of the particle pair is equal to 0 in both *longitudinal* and *side* directions.

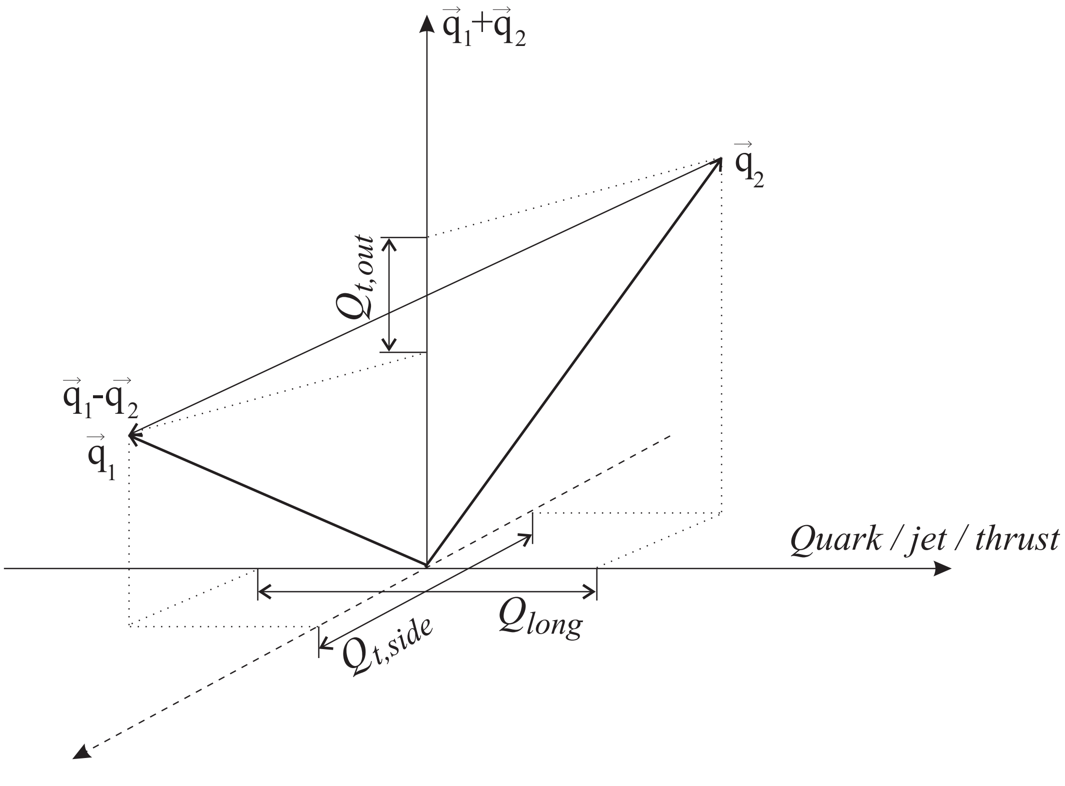

Figure 3.1: Longitudinal Centre-of-Mass System.

The total Q^2 assumes the form:

$$Q^2 = Q_{long}^2 + Q_{t,side}^2 + Q_{t,out}^2(1 - \beta^2); \qquad \beta = \frac{q_{t,out}^1 + q_{t,out}^2}{E_1 + E_2}, \tag{3.3}$$

where indices 1 and 2 denote the first and second particle from the pair. Since $q_{long}^1 + q_{long}^2 = 0$, the longitudinal component Q_{long} may be expressed by the formula:

$$Q_{long} = q_{long}^1 - q_{long}^2 = 2q_{long}^1 = 2q_{long} = 2q_z. \tag{3.4}$$

The LCMS frame makes possible the separation between spatial and temporal dimensions. This is caused by the fact that the energy difference of the particles, which implies also the difference in the emission time of the bosons, i.e. temporal dimension of the source, appears only in the $Q_{t,out}$ component. The Q_{long} and $Q_{t,side}$ fractions are assigned to the direction of motion of the initial partons.
The three-dimensional correlation function is defined as follows:

$$C_2(Q_{t,out}, Q_{t,side}, Q_{long}) = 1 + \lambda e^{-Q_{t,out}^2 R_{t,out}^2 - Q_{t,side}^2 R_{t,side}^2 - Q_{long}^2 R_{long}^2}. \tag{3.5}$$

In many cases the studies of C_2 in three dimensions are statistically limited, which calls for the reduction in the number of parameters considered in the fit to the correlation function. Therefore, the two-dimensional projection of the LCMS frame is often used in analyses, with longitudinal component $Q_{\|} \equiv Q_{long}$ and transverse component $Q_{\perp}^2 = Q_{t,out}^2 + Q_{t,side}^2$. The parametrisation of the correlation function C_2 in the two-dimensional case takes the form:

$$C_2(Q_{\|}, Q_{\perp}) = 1 + \lambda e^{-Q_{\|}^2 R_{\|}^2 - Q_{\perp}^2 R_{\perp}^2}, \tag{3.6}$$

where $R_{\|}$ is the longitudinal geometrical radius of the source and $R_{\perp}$ represents the composition of the transverse radius and emission time difference. They may be determined from the fits to projections of the two-dimensional correlation function.

3.3 Long-range correlations

In order to account for the so-called 'long-range correlation', caused primarily by energy-momentum conservation, an additional term usually appears in the parametrisations (2.20) and (2.21), namely [8, 9]:

$$C_2(Q) = N(1 \pm \lambda e^{-R^2 Q^2})(1 + \alpha_1 Q + \alpha_2 Q^2), \tag{3.7}$$

where sign '+' corresponds to the BEC and '−' to the FDC effect. α_1 and α_2 denote free parameters that have to be extracted from the fit to the experimental data. The empirical term $(1+\alpha_1 Q+\alpha_2 Q^2)$ accounts not only for two-particle long-range correlations in $C_2(Q)$ at high Q values, but also for other effects, such as imperfections in the Monte Carlo simulation.

3.4 Final state interactions

The final state interactions (FSI) involving both electromagnetic (Coulomb) and strong forces, are present in the Bose-Einstein and Fermi-Dirac correlation regions and may potentially affect the distributions of analysed observables. Strong final state interactions are present in both charged and neutral hadron systems, while the Coulomb interactions exert an influence only on the charged hadron systems.

At small Q, the Coulomb repulsion between two identically charged hadrons is presumed to alter the correlation function $C_2(Q)$ by reducing the enhancement signal. For that reason the so-called 'effective correlation function' is frequently employed:

$$C_2^{eff}(Q) = C_2(Q) \times G_2(Q), \tag{3.8}$$

where $C_2(Q)$ represents the correlation function constructed on the assumption that Coulomb interactions are absent, while $G_2(Q)$ denotes the Gamov penetration factor [36], defined as follows:

$$G_2(Q) = \frac{2\pi\alpha m\epsilon_1\epsilon_2}{Q} \cdot \frac{1}{\exp(2\pi\alpha m) - 1}. \tag{3.9}$$

In the above formula m and α denote the particle mass and the fine structure constant, respectively. The ϵ_1 and ϵ_2 indicate charges of hadrons (in electron charge magnitude units). According to formula (3.9), the Coulomb effect increases with $Q \to 0$. It should be noted that the corrections proportional to $1/G_2(Q)$, introduced to the real data, may cause an unwanted surplus of the signal [37]. Since the Coulomb corrections are significant only in the low Q region, they have to be considered only in a few first bins of measured data distributions.

The majority of the reported BEC or FDC analyses take into account the Coulomb interaction effect, whereas the strong final state interactions are usually unaccounted for because of its complexity and insignifficant influence on the fit parameters.

Chapter 4

Correlation radii measurements at LEP

This chapter summarises briefly measurements of the correlation radii performed by four LEP experiments: ALEPH [38], DELPHI [39], L3 [40] and OPAL [41]. The results of one-dimensional analyses are discussed separately from two- and three-dimensional studies. The LEP accelerator and the DELPHI apparatus are described in chapter 5.

4.1 Results of one-dimensional analyses

Table 4.1 lists source radii and chaoticity parameters as determined by one-dimensional BEC analyses of two identical pions in e^+e^- annihilation, performed by LEP experiments. The results are divided into two groups according to the type of reference sample used. The first method relies on the unlike reference sample. In the second case, either a full detector Monte Carlo simulation or a sample obtained by using event-mixing technique has been taken as a reference sample.

Table 4.1: The values of the source emitter radius R and the chaoticity parameter λ, as given by formula (2.20), obtained from Bose-Einstein correlation studies for $\pi^\pm\pi^\pm$ and $\pi^0\pi^0$ pairs, as performed by LEP experiments. The errors represent quadratic sum of statistical and systematic errors. The Coulomb corrections have not been included.

Hadron-hadron	Reference sample				Experiment
	Unlike		MC or event-mixed		
	R [fm]	λ	R [fm]	λ	
$\pi^\pm\pi^\pm$ (BEC)	0.82 ± 0.04	0.48 ± 0.03	0.52 ± 0.02	0.30 ± 0.01	ALEPH [42]
	0.83 ± 0.03	0.31 ± 0.02	0.47 ± 0.03	0.24 ± 0.02	DELPHI [43]
	–	–	0.46 ± 0.02	0.29 ± 0.03	L3 [44]
	0.96 ± 0.02	0.67 ± 0.03	0.79 ± 0.02	0.58 ± 0.01	OPAL [45]
$\pi^0\pi^0$ (BEC)	–	–	0.31 ± 0.10	0.16 ± 0.09	L3 [44]
	–	–	0.59 ± 0.11	0.55 ± 0.15	OPAL [46]

The values of the source radius R collected in Table 4.1 clearly exhibit a significant dependence on the choice of reference sample. Measurements of the emitter source radius generally give higher values for the technique based on the unlike reference sample as compared to the ones based on the MC or event-mixed reference sample. The measured values of parameter λ are to a lesser extent dependent on the choice of reference sample. The second important conclusion is that the results of R concentrate around the value ~ 0.85 fm for the first technique, whereas they are less stable and spread widely within the range from $\sim$0.5 fm to $\sim$0.8 fm for the second technique.

The BEC analyses for the $\pi^0\pi^0$ system has also been performed [44, 46], but experimental difficulties in identifying two neutral pions are a central problem of such studies. According to the Lund model, the correlation radius for $\pi^0\pi^0$ is expected to be smaller as compared to the $\pi^\pm\pi^\pm$ radius, while the chaoticity parameter is predicted to be larger. The OPAL measurement for $\pi^0\pi^0$ yielded R and λ compatible with $\pi^\pm\pi^\pm$, whereas the values of R and λ determined by L3 experiment were lower.

Multiplicity of pions in a hadronic event produced in e^+e^- annihilation is high, therefore a sufficient amount of data is available at the disposal of $\pi^\pm\pi^\pm$ studies. The BEC analysis for the $K^\pm K^\pm$ system suffers from smaller rate as compared to pions. Moreover, this rate is further reduced by kaon identification efficiency (typical values for DELPHI are included in chapter 5), which is usually dependent on the momentum. The above restriction introduces momentum dependent limitations to the available phase-space. The results of the $K^\pm K^\pm$ analysis are quoted in Table 4.2.

Table 4.2: The values of the source emitter radius R and the chaoticity parameter λ obtained from Bose-Einstein and Fermi-Dirac correlation studies for identical hadron pairs, as performed by LEP experiments.

Hadron-hadron	R [fm]	λ	Experiment
$K^\pm K^\pm$ (BEC)	$0.48 \pm 0.04 \pm 0.07$	$0.82 \pm 0.11 \pm 0.25$	DELPHI [47]
	$0.56 \pm 0.08 \; ^{+0.07}_{-0.06}$	$0.82 \pm 0.22 \; ^{+0.17}_{-0.12}$	OPAL [48]
$K^0_S K^0_S$ (BEC)	$0.65 \pm 0.07 \pm 0.15$	$0.96 \pm 0.21 \pm 0.40$	ALEPH (MC ref.) [49]
	$0.57 \pm 0.04 \pm 0.14$	$0.63 \pm 0.06 \pm 0.14$	ALEPH (mix ref.) [50]
	$0.55 \pm 0.08 \pm 0.12$	$0.61 \pm 0.16 \pm 0.16$	DELPHI [47]
	$0.76 \pm 0.10 \pm 0.11$	$1.14 \pm 0.23 \pm 0.32$	OPAL [51]
$\bar{p}\bar{p}$ (FDC)	$0.11 \pm 0.01 \pm 0.01$	$0.49 \pm 0.04 \pm 0.08$	ALEPH [50]
	$0.142 \pm 0.035 \pm 0.047$	$0.76 \pm 0.16 \pm 0.29$	OPAL [52]
$\Lambda\Lambda$ (FDC)	$0.11 \pm 0.02 \pm 0.01$	–	ALEPH [53]
$\Lambda\Lambda$ (FDC)	$0.17 \pm 0.13 \pm 0.04$	–	ALEPH [53]
(spin analyses)	$0.11 \; ^{+0.05}_{-0.03} \pm 0.01$	–	DELPHI [54]
	$0.19 \; ^{+0.37}_{-0.07} \pm 0.02$	–	OPAL [55]

$K^0_S K^0_S$ pairs originating from K^0K^0 as well as from $K^0\bar{K}^0$ productions [56] were also used to determine the BEC radius. One of the drawbacks of these measurements is that a part of the BEC enhancement may result from decays of the sub-threshold $f_0(980)$ scalar resonance.

The analyses of Fermi-Dirac correlations have been performed at LEP for proton and Λ pairs. The correlation radius for $\bar{p}\bar{p}$ has been determined by OPAL [52]. At the time this thesis was being prepared, the second measurement by ALEPH [50] was announced. The correlation radius for $\Lambda\Lambda$ was measured by ALEPH [53], DELPHI [54] and OPAL [55]. Owing to the fact that the Λ decays weakly to $p\pi$, the Λ spin state may be determined, making possible the absolute measurement of the correlation radius based on the spin-spin correlations, without resorting to the reference distribution.

4.2 Results of two- and three-dimensional analyses

LEP collaborations performed also two- and three-dimensional analyses for pion pairs. The L3 and OPAL analyses were conducted by examining three components ($R_{t,out}$, $R_{t,side}$, $R_{\|}$) in the LCMS frame, whereas the ALEPH and DELPHI experiments carried out the BEC studies in two dimensions, determining correlation radii corresponding to $Q_{\perp}^2 = Q_{t,side}^2 + Q_{t,out}^2$ ($R_{\perp}$) and to Q_{long}^2 ($R_{\|}$). The results of these studies are listed in Table 4.3.

Table 4.3: The values of correlation radii for two- (ALEPH, DELPHI) and three-dimensional (L3, OPAL) BEC analyses for identically charged pion pairs $\pi^{\pm}\pi^{\pm}$.

$R_{t,out}$ [fm]	$R_{t,side}$ [fm]	$R_{\perp}$ [fm]	$R_{\|}$ [fm]	Experiment
–	–	0.47 ± 0.01	0.77 ± 0.01	ALEPH [57] (mix ref.)
–	–	0.79 ± 0.01	0.87 ± 0.02	ALEPH [57] (unlike ref.)
–	–	$0.53 \pm 0.02 \pm 0.07$	$0.85 \pm 0.02 \pm 0.07$	DELPHI [58]
$0.53 \pm 0.02^{+0.05}_{-0.06}$	$0.59 \pm 0.01^{+0.03}_{-0.13}$	–	$0.74 \pm 0.02^{+0.04}_{-0.03}$	L3 [59]
$0.65 \pm 0.01^{+0.02}_{-0.12}$	$0.81 \pm 0.01^{+0.02}_{-0.03}$	–	$0.99 \pm 0.01^{+0.03}_{-0.02}$	OPAL [60]

The spread of the above results is broad and may be due to unaccounted systematic errors related to different methods used. The value of longitudinal component of the correlation radius ($R_{\|}$) in each experiment is greater than that of components corresponding to the transvese direction ($R_{t,out}$, $R_{t,side}$, $R_{\perp}$). Such elongation of the source is expected from the Lund string model, but quantitative interpretation of the effect is still missing.

The most remarkable outcome of the studies outlined in previous paragraphs is the evident dependence of the correlation radius on hadron mass. Namely, the radius is inversely proportional to the hadron mass ($\partial R/\partial m < 0$), while the Lund string model gives a contrary prediction $\partial R/\partial m > 0$ [10]. Other explanations of the above-mentioned dependence are discussed in detail in Sect. 8.1-8.3.

Chapter 5

Experimental apparatus

The thesis investigates the Bose-Einstein and Fermi-Dirac correlation effects using data recorded in the DELPHI detector which was operating at the LEP accelerator at CERN. Therefore, the description of LEP collider as well as the parts of DELPHI detector which were crucial from the perspective of the analysis are presented below.

5.1 LEP accelerator

LEP (Large Electron-Positron) collider [61] (cf Fig.5.1) with the circumference of 26.7 km was the largest accelerator built so far. It was located at CERN (European Organization for Nuclear Research), on the border between Switzerland and France, and was operating in the years 1989−2000. LEP was a type of particle accelerator which stored and accelerated counter-rotating beams of electrons and positrons and then brought them into collision. Since the total momentum of the initial state amounted to zero, all the energy of collision was converted into the masses and four-momenta of final state particles. Bunches of particles were injected into the LEP ring until a sufficiently high intensity was accumulated in each beam. Next, the two beams were accelerated simultaneously. After reaching the required beam energy, the beams were brought into collision. Collisions took place at four points in the ring, namely at the particle detectors (ALEPH, DELPHI, L3 and OPAL) locations. Detectors measured the properties of the e^+e^- annihilation products. Each LEP detector was optimised differently to allow for studying various physical aspects of the interactions.

5.1.1 Accelerating system

Accelerators built earlier at CERN played the role of injectors to LEP in a complex, interconnected system [62]. First, the linear accelerator produced bunches of electrons and positrons at the energy of 600 MeV and fed them into the 28 GeV Proton Synchrotron (PS) to be accelerated to the value of 3.5 GeV and then transferred to the Super Proton Synchrotron (SPS). In SPS these bunches were accelerated to 20 GeV before being injected into the LEP collider. There, electrons and positrons were accelerated in a vacuum pipe surrounded by magnets and 128 five-cell copper accelerating cavities powered by sixteen 1 MW klystrons.

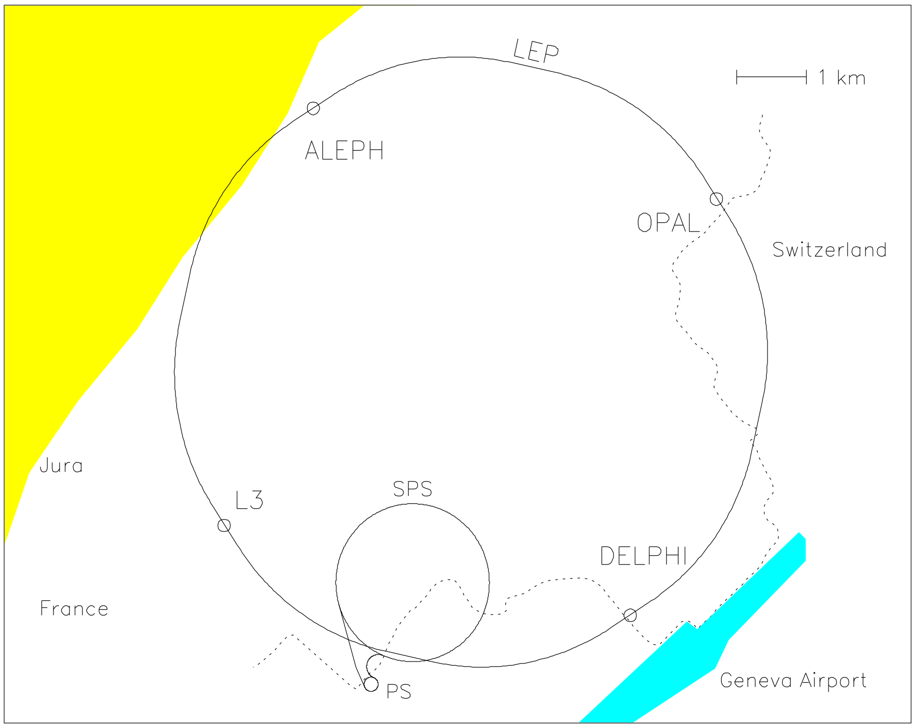

Figure 5.1: Scheme of LEP collider.

5.1.2 LEP characteristics

The beam energy and the luminosity constitute the crucial parameters of an individual accelerator. Relevant characteristics of the above parameters for LEP are presented below.

The data sample analysed in this thesis was collected in the so-called LEP1 phase (1989−1995) when the beam energy amounted to 45.6 GeV. It corresponded to the center-of-mass energy for e^+e^- collision of 91.2 GeV, i.e. the mass of Z^0 resonance. In the second running period, LEP2 (1995−2000), the center-of-mass energy varied in the range (131−209) GeV.

As has been mentioned above, another important parameter of the collider is the luminosity L which characterises event production rates:

$$L = R/\sigma, \tag{5.1}$$

where σ denotes the interaction cross section and R stands for the event production rate. At colliders, the luminosity is measured by counting the number of events in a process with a clear experimental signature, a high statistics and a cross section which can be calculated with a great precision. The process satisfying the above conditions, chosen in the case of LEP, was $e^+e^- \to e^+e^-(\gamma)$ Bhabha scattering at small angles. The value of the luminosity for LEP1 amounted to 2.4×10^{31} cm^{-2} s^{-1}, while in the case of LEP2 to the value of 1.0×10^{32} cm^{-2} s^{-1}. The luminosity integrated over time is directly related to the total data volume. The integrated luminosity of the DELPHI detector for LEP1 amounted to 270 pb^{-1}, whereas for LEP2 to 650 pb^{-1}.

5.1.3 Physics at LEP

In the LEP1 running period the data were collected around the Z^0 energy (91 GeV). Extensive tests of the validity of the Standard Model (SM) were performed with an unprecedented degree of accuracy. High precision measurements of the electroweak (EW) parameters [63, 64] of the SM were carried out at the level of few permils, including Z^0 mass and width. These studies excluded the existance of any further family of light neutrinos beyond the three already known. Precise EW measurements allowed for the prediction of the top quark mass. Extensive studies on the fragmentation mechanism of quarks and gluons provided a precise test of Quantum Chromodynamics.

During the LEP2 running period, a higher energy range was investigated in order to find new particles with masses up to the order of 100 GeV, study the production of intermediate boson pairs i.e. W^+W^- and Z^0Z^0, as well as to search for new particles, such as Higgs bosons and supersymmetric particles. LEP2 also contributed to the precision measurements of the SM parameters through an accurate determination of the W boson mass.

In 2000 LEP was dismantled so as to make room for the Large Hadron Collider (LHC) [65] installation.

5.2 DELPHI detector

DELPHI (DEtector with Lepton, Photon and Hadron Identification) [66, 67] was one of four general purpose detectors for e^+e^- physics working at LEP collider. It provided three-dimensional information about charged particle tracks and energy deposited by neutral particles. DELPHI was designed and built with a special focus on hadron identification over nearly full solid angle. A general view of the detector is shown in Fig.5.2.

The detector's coordinate system was defined as follows: the z axis was oriented along the electron direction, the x axis pointed towards the centre of LEP collider, and the y axis pointed upwards. The polar angle to the z axis was called θ and the azimuthal angle around the z axis was called ϕ. The radial coordinate was defined as $R = \sqrt{x^2 + y^2}$.

The DELPHI detector, situated about 100 m under the ground, consisted of a cylindrical part (barrel) surrounding the interaction point, and two end-caps covering the small polar angle regions (cf Fig.5.2). The end-caps could be moved to gain access to the subdetectors. The total length and diameter of the apparatus were over 10 m each and the total weight amounted to 3,500 tons. The superconducting solenoid (7.4 m long, with the inner diameter of 5.2 m) provided a highly uniform magnetic field of 1.23 T, parallel to the beam pipe, throughout the central tracking volume. It contained the following barrel detectors: the Vertex Detector (VD), the Inner Detector (ID), the Time Projection Chamber (TPC) and the Outer Detector (OD), and also the forward tracking chambers (Forward Chambers A and B).

The Ring Imaging Cherenkov (RICH) detectors allowed for charged particle identification in both the barrel (BRICH) and forward (FRICH) regions. Electron and photon identification was mainly performed by the High density Projection Chamber (HPC) located in the barrel region and by the Forward Electromagnetic Calorimeter (FEMC) placed in the end-caps. Smaller polar angles, crucial for detecting e^+ and e^- from $\gamma\gamma$ processes and for luminosity measurement from Bhabha events, were covered by the Small angle Tile Calorimeter (STIC) (which had replaced the Small Angle Tagger (SAT) in

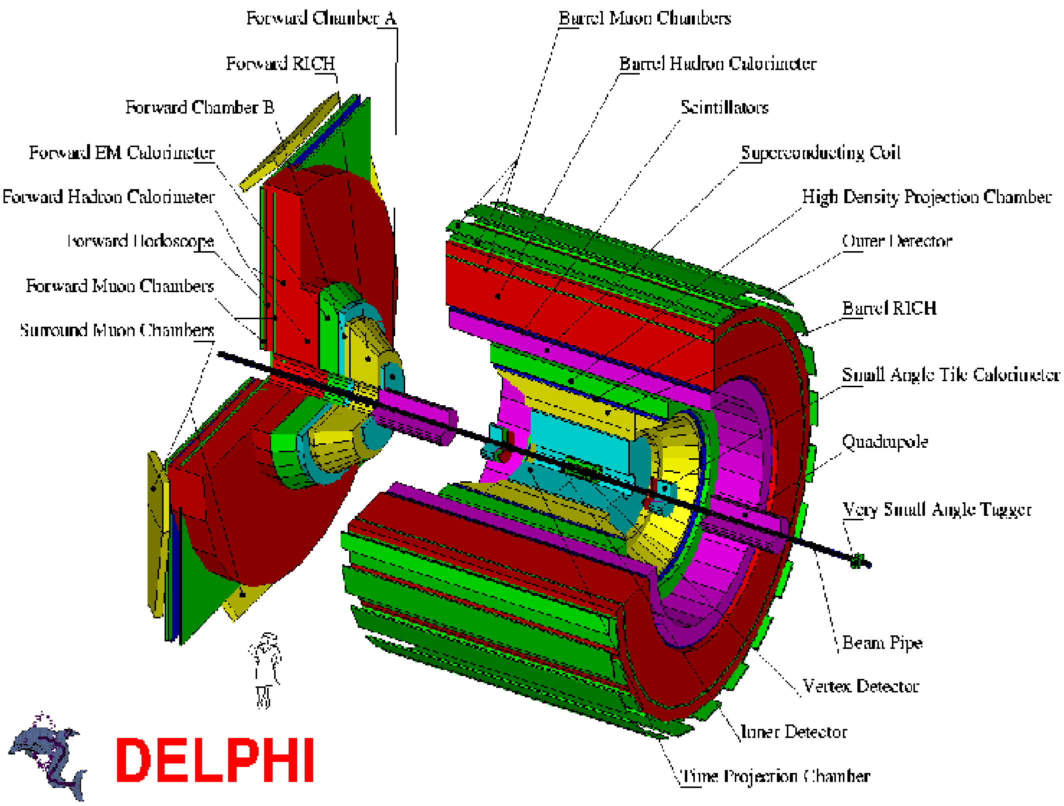

Figure 5.2: Layout of the DELPHI detector (only one end-cap is shown).

April 1994), and the Very Small Angle Tagger (VSAT). In order to achieve more complete hermeticity for high energy photon detection, additional scintillators were installed in the cable duct regions between the barrel and each end-cap, and in the small gaps between the HPC modules, which were not adequately covered for this purpose by the Time Of Flight (TOF) scintillators. The iron return yoke of the magnet was equipped with limited streamer mode detector to create a sampling gas calorimeter, the Hadron Calorimeter (HAC). Muon identification was provided by the Barrel (MUB) and Forward (MUF) muon drift chambers. A layer of Surrounding Muon Chamber (SMC) based on limited streamer tubes was installed to fill the gap between the barrel and forward regions.

The below description concerns only these parts of the apparatus which were essential for the analyses performed in this thesis.

5.2.1 Tracking system

The function of the tracking detectors is a precise determination of directions and momenta of the charged particles. The presentation will start with the tracking detector closest to the interaction point and end with the furthest one.

Vertex Detector was a silicon detector providing very precise tracking close to the interaction point, in order to detect short-lived particles by extrapolating the tracks back, towards the collision point. Owing to the above detector properties it was possible to reconstruct secondary vertices, in particular those of beauty and charm hadrons, on the basis of the information obtained from VD. It consisted of three coaxial cylindrical layers of silicon strip detectors at average radii of 6.3, 9.0 and 10.9 cm. The innermost and outer-most layers were double-sided. Each covered the full azimuthal angle and was composed of 24 sectors, with overlaps between adjacent sectors. For polar angles within the range $25^\circ \leq \theta \leq 155^\circ$, a particle crossed all the three layers of VD. The precision of the track measurement in VD was 7.6 μm for $R\phi$ coordinate and varied within the range 9−30 μm in the case of z coordinate.

Inner Detector provided both tracking and trigger information. It was composed of an inner drift chamber with jet chamber geometry of 24 azimuthal sectors, each providing up to 24 $R\phi$ points per track between radii of 12 and 23 cm. Surrounding the jet chamber there were five cylindrical layers of straw tube detectors (between radii of 23 and 28 cm) measuring $R\phi$. The polar angle acceptance for tracks, giving a hit to the innermost anode wires, was $15^\circ \leq \theta \leq 165^\circ$. The average single point precision amounted to 85 μm with local track element precisions of $\sigma(R\phi) = 40\mu$m and $\sigma(\phi) = 0.89$ mrad.

Time Projection Chamber was the principal tracking device of DELPHI detector. It was a combination of drift chambers and Multi-Wire Proportional Chamber (MWPC) and provided the identification information by measuring the specific energy loss dE/dx. TPC was filled with the mixture of 80% Ar and 20% CH_4, and under the atmospheric pressure.

In the DELPHI detector the pattern recognition started from the TPC information and afterwards other track chambers were added (OD, FCA and FCB) to improve momentum resolution. Both end-plates of the TPC were divided into 6 azimuthal sectors, each equipped with 192 sense wires and 16 circular pad rows with constant spacing. At least three such pad-rows were crossed down by a particle traversing at polar angles $20^\circ \leq \theta \leq 160^\circ$. The metal plate electrode placed in the central region of the detector caused efficiency losses in the Rz plane. Short cathode pads (in R), in total 1,680 pads per sector, were chosen to improve two-track separation. The detector provided up to 16 space points per particle trajectory at radii between 35 and 111 cm between polar angles of $39^\circ \leq \theta \leq 141^\circ$. The single point precision for tracks from $Z^0 \to \mu^+\mu^-$ decays was 250 μm in the $R\phi$ plane and 880 μm in the Rz plane.

The identification of charged hadrons in DELPHI detector relied on both the ionisation energy loss per unit length (for relatively low momenta) in the TPC and on the information provided by RICHes (cf Sect. 5.2.2).

Outer Detector consisted of five layers of drift tubes located between radii 197 cm and 206 cm. The active length of the detector corresponded to a polar angle within the range from 42° to 138°. It provided a precise direction measurement after that obtained from the Barrel Ring Imaging Cherenkov detector, giving fast trigger information in both $R\phi$ and z, and improving the momentum resolution. It was composed of 24 modules mounted on the BRICH construction, each consisting of 145 drift tubes placed in five layers. The layers were staggered and the adjacent modules were overlapped, providing full azimuthal coverage. All layers gave $R\phi$ information. Additionally, three layers provided fast z information by relative signal timing from both ends. OD provided a single point precision of $\sigma(R\phi) = 110$ μm independent of the drift distance, whereas the precision in z coordinate was $\sigma(z) = 3.5$ cm.

The tracking system gave the momentum measurement accuracy for muons of $\sigma(1/p) = 0.6 \times 10^{-3}$ (GeV/c)$^{-1}$, while the double track resolution in $R\phi$ plane amounted to $\sim$100 μm.

5.2.2 Charged hadron identification

When a charged particle travels faster than the speed of light in a dielectric medium, the polarized molecules of the medium emit electromagnetic radiation (Cherenkov photons) on a cone whose axis is the particle trajectory direction. The opening angle θ_c of this cone is given by the relation $\cos\theta_c = 1/(\beta n)$, where β denotes the particle velocity relative to the speed of light in vacuum (v/c) and n indicates the refractive index of the traversed medium. Since the Cherenkov radiation is emitted only if the speed of the particle is above the speed of light $v > c/n$, for each particle of a given rest mass this corresponds to a different momentum threshold for the emission of Cherenkov light. Detectors devoted to particle identification are constructed on the basis of the above phenomenon. The RICH technique allows for both the detection of the presence of Cherenkov light and the measurement of the Cherenkov angle.

Charged particle identification in DELPHI was provided mainly by liquid and gas Ring Imaging Cherenkov Counters (RICH). DELPHI RICH detectors contained two radiators of different refractive indices (cf Fig.5.3). The liquid radiator was used for particle identification in the momentum range from 0.7 to 9.0 GeV/c and the gas radiator for the range from 2.5 to 25 GeV/c. The full solid angle coverage was provided by two independent detectors, one located in the barrel region (BRICH) and the other in the end-cap regions (FRICH).

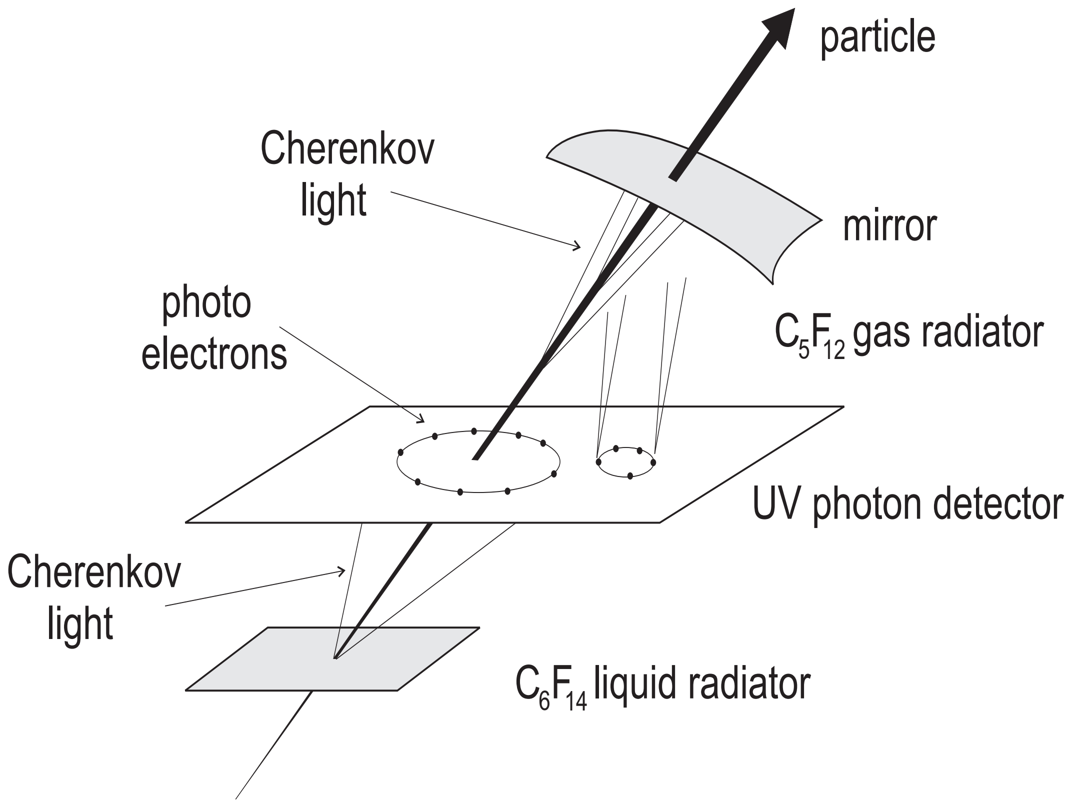

Figure 5.3: The Cherenkov effect as observed by the BRICH detector. Due to the parabolic shape of the mirrors, the focusing point on the photon detector for photons in the gas radiator does not depend on the emission point along the particle trajectory. The difference in the diameters of the Cherenkov rings coming from different radiators is clearly visible.

Barrel RICH was located between the Time Projection Chamber and the Outer Detector. It was a 350 cm long cylinder with the inner radius of 123 cm and the outer of 197 cm, divided into two halves by a central 6.4 cm thick support wall. Liquid radiator boxes with quartz windows on the outer surface were mounted near the inner surface of the cylinder. UV photons were detected in the drift tubes constructed entirely from quartz plates, which acted as TPCs with readout chambers at the outer end. Cherenkov photons produced in the outer gas volume were reflected by parabolic mirrors and focused into ring images in the same drift tubes. Each half of the detector contained 24 drift tubes and liquid radiator containers, in azimuth, grouped in pairs. C_6F_{14} was used as a liquid radiator and C_5F_{12} as a gas radiator. BRICH covered polar angles between 40° and 140°. For the sample of muons from the decay $Z^0 \to \mu^+\mu^-$, the measured number of photoelectrons per track amounted to 14 (8) for the liquid (gas) radiator. At the same time, the value of the mean Cherenkov angle was 666 mrad for the liquid and 62.3 mrad for gas radiator.

Forward RICH was located between 1.7 m $\leq |z| \leq$ 2.7 m and covered polar angles in the range from 15° to 35°. Each end-cap consisted of two truncated half-cones and was divided into 12 modular sectors in azimuthal direction. Each sector of this kind contained one drift-box, two MWPC, three liquid radiator containers and five mirrors. The vessel was built from carbon-epoxy laminate and contained heating elements on the inside and cooling pipes on the outside. The two vessels from one end-cap were supported by an iron yoke fitted to a carbon-epoxy cylinder. C_6F_{14} and C_5F_{12} were used as liquid and gas radiators, respectively. In the case of muons from $Z^0 \to \mu^+\mu^-$ decays the number of photoelectrons per track amounted to 7 (8) for the liquid (gas) radiator, with the mean Cherenkov angle precision of 675 mrad for the liquid and 55 mrad for gas radiator.

Thanks to the Ring Imaging Cherenkov Detectors DELPHI gained a unique and very important hadron indentification tool. The information from both the liquid and gas radiators could be combined with the dE/dx information measured in the Time Projection Chamber to achieve separation of hadron species at different momenta (cf Fig.5.4). The RICH detectors provided acceptable hadron identification in the higher momentum range, while the TPC could distinguish particles with low momenta. The particle identification DELPHI algorithms were included in the RPROCO software package [68], which combined information on the Cherenkov angle and dE/dx. The process of identification based on the combined information from TPC and RICH encountered the problem how to deal with momentum ranges when one detector could not separate different particle hypotheses and another detector was in the so-called veto mode, i.e. when one expected no signal for a track in the detector. That is why the construction of simple tags was strongly momentum dependent. The most advanced method used to combine the information on the Cherenkov angles from RICH with the dE/dx losses from TPC was implemented in the MACRIB software package [69]. Here, all the information was put into the neural network allowing for best quality identification as far as kaons and protons were concerned. In the case of this package the average identification efficiency for kaons amounted to around 75% with respective purity of around 80% [69] within a broad momentum range.

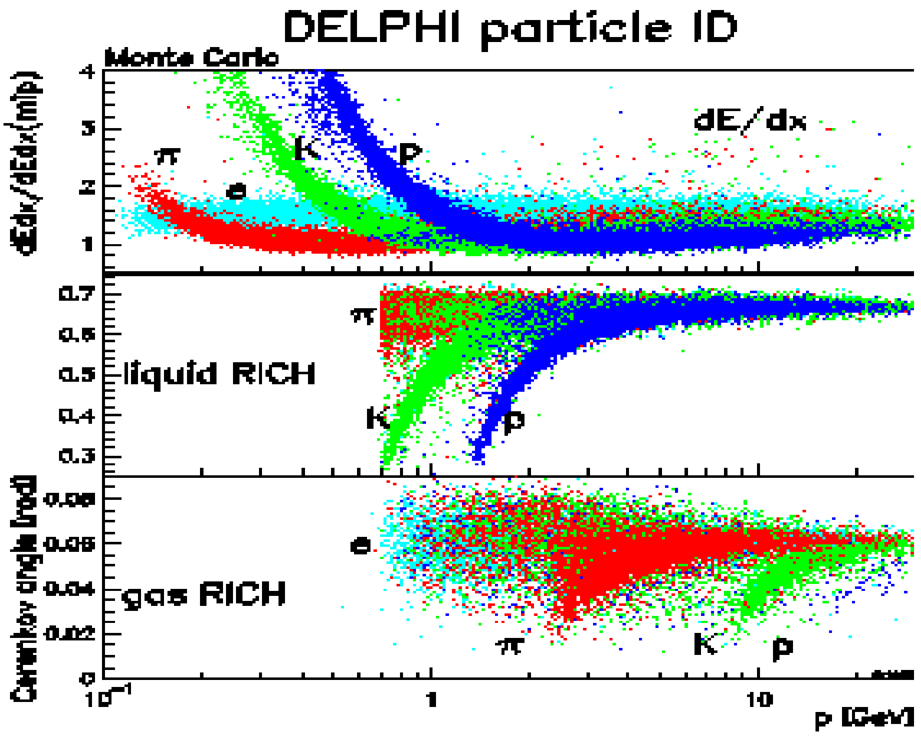

Figure 5.4: DELPHI particle identification. The specific ionisation loss dE/dx vs the track momentum (upper plot) shows clear bands corresponding to electrons, pions, kaons and protons. Two lower plots show the distributions of the mean Cherenkov angle with a clear separation between π, K and p.

5.2.3 Track reconstruction and detector simulation

The track reconstruction in DELPHI was based on the DELANA [70] package. A basic element of DELANA was the package TANAGRA (Track ANAlysis and GRAphics) [71] which provided data structure for storing track and vertex information in a format independent of various program modules.

The detector response was simulated by the use of DELSIM [67, 72] package aimed at generating Monte Carlo samples which were as far as possible similar to the raw real data. These data were then passed through the reconstruction (DELANA) and analysis programs in exactly the same way as the real data, i.e. the effects such as secondary interactions, particle cascades and ionisation losses as well as the aparatus response were reliably simulated.

5.3 Data analysis

The present analyses was based on around 2.2×10^6 hadronic events using data collected between 1994 and 1995 by the DELPHI detector at the centre-of-mass energy corresponding to the Z^0 mass. In the above-mentioned period of data collecting RICH detectors provided the identification information of best quality.

5.3.1 Track selection

The tracks of charged particles had to fulfil the following requirements: the track length greater than 30 cm, the relative error on momentum measurement lesser than 100%, at least one point of the track trajectory measured in the VD, the track impact parameter with reference to the interaction point lesser than 0.1 cm in the plane orthogonal to the beam direction and the respective impact parameter in the plane parallel to the beam direction below 1 cm as well as the track polar angle θ between $25°$ and $155°$. Additionally, to select the momentum region with the MC simulation agreeing very well with data, the minimum particle momentum had to be greater than 0.1 GeV in the case of pions, whereas it increased to the value of 0.7 GeV for protons. Moreover, it was required that the identification information be available from both the RICH detector and the dE/dx measurement.

5.3.2 Selection of hadronic events containing $\pi\pi$ and pp pairs

The following requirements were applied in the selection of hadronic Z^0 decays: at least five charged tracks and the total energy of all charged particles exceeding $0.12\sqrt{s}$, where s represents the square of the center-of-mass energy. The selection criteria for hadronic events limited the background from beam-gas interactions and $\gamma\gamma$, $\mu\mu$, ee final state events to the level of 0.1%. The contamination of $\tau\tau$ events was reduced to under 0.2%.

Pion analysis
A hadronic event was accepted on the condition that it contained at least two same-charge pion candidates which could not be classified either as the decay products of an identified K^0_s, or tracks from photon conversions. Pion identification was based on the requirement that the particle was not identified as a kaon or a proton, by employing an identification package RPROCO. This yielded the purity of 80% and the identification efficiency of 80% for a single pion sample.

The thrust tensor was calculated for each event using charged tracks and only events with the thrust value above 0.95 were accepted in order to select events with a two-jet topology. The remaining three-jet events constituted around 6% of the sample. The angle between the thrust vector and the beam direction (θ_{thrust}) had to fall within the range from $41°$ to $139°$ in order to single out events reconstructed in the barrel part of the aparatus.

Applying the above criteria a sample of about 0.7×10^6 events with at least two pion candidates was obtained. Distributions of the most important variables employed in the event selection for pions were compared to the Monte Carlo simulated distributions in Fig.5.5.

Proton analysis
In the case of protons a hadronic event was accepted only if it contained at least two proton (antiproton) candidates, which were not the decay products of an identified Λ hyperon. Proton candidates were selected using the particle identification information from the MACRIB package. A proton candidate was accepted if the variable XPRNET exceeded 0.95. The XPRNET indicated a neural network response, normalised to the range (0−1), where XPRNET = 0 (1) minimises (maximises) probability of proton hy-

pothesis. Therefore, the single proton purity was ∼85% at the identification efficiency of 70%, as extracted by the MC simulation. This yielded the purity of 70% for the $\bar{p}\bar{p}$ sample and the purity of 50% for pp. Moreover, to make feasible the examination of samples with different purities, the above-mentioned requirement was altered within the range 0.90−0.97 in subsequent analyses. Additionally, the RPROCO package was applied in order to compare identification results. This package provided a less efficient proton identification at the same purity as compared to MACRIB, and it was finally used to check for possible biases in the part of analysis related to the particle identification.

The sample of about 180, 000 events with at least two proton candidates was selected on the basis of the criteria described above. Using the MC simulation it was established that the background contaminates strongly the low-Q region for pp sample due to secondary interactions. Therefore, only the $\bar{p}\bar{p}$ sample was used in the standard analysis. Nevertheless, the result for the pp sample with background subtracted was consistent with the $\bar{p}\bar{p}$ and it is also quoted.

The analysis was performed for all events independent of jet multiplicity. It was ascertained that the results for the sample limited to two-jet events with the constraint on the thrust > 0.95 agree within errors with the standard analysis.

5.3.3 Details of Monte Carlo simulations

The detector acceptance and event selection efficiency were examined using the Monte Carlo technique. The simulation of a sample without BEC was conducted by the author.

Pion analysis

In the case of pions, the sample of $\sim 5.4\times10^6$ Monte Carlo hadronic events was generated using the JETSET 7.3 PS [15] generator with parameters tuned as in [32]. In this model the BEC effect is simulated on the basis of the LUBOEI algorithm, with parameters corresponding to the correlation radius of about 0.5 fm (PARJ(93) = 0.394) and to a fully incoherent source (PARJ(92) = 1.0). A sample of $\sim 5\times10^6$ events, produced using the JETSET 7.3 PS generator with the BEC effect switched off, was used in the analysis of distributions without the BEC effect. The efficiency corrections were obtained by comparing the simulated distributions to the distributions at the generator level with no requirements imposed. The 'bin-by-bin' method was chosen to correct the observed distributions.

Proton analysis

In the case of protons, a sample of about 6.2×10^6 Monte Carlo hadronic events was produced on the basis of the JETSET 7.4 PS [73] generator with parameters tuned as in [32]. Around 560,000 events with at least two proton candidates were preselected from this sample. Contrary to the Bose-Einstein studies for $\pi^\pm\pi^\pm$ and $K^\pm K^\pm$, where the Bose-Einstein effect is simulated using LUBOEI algorithm, JETSET 7.4 generator does not contain the Fermi-Dirac correlation effect. Thus, the Monte Carlo sample might be used directly as a reference sample in the Fermi-Dirac analysis.

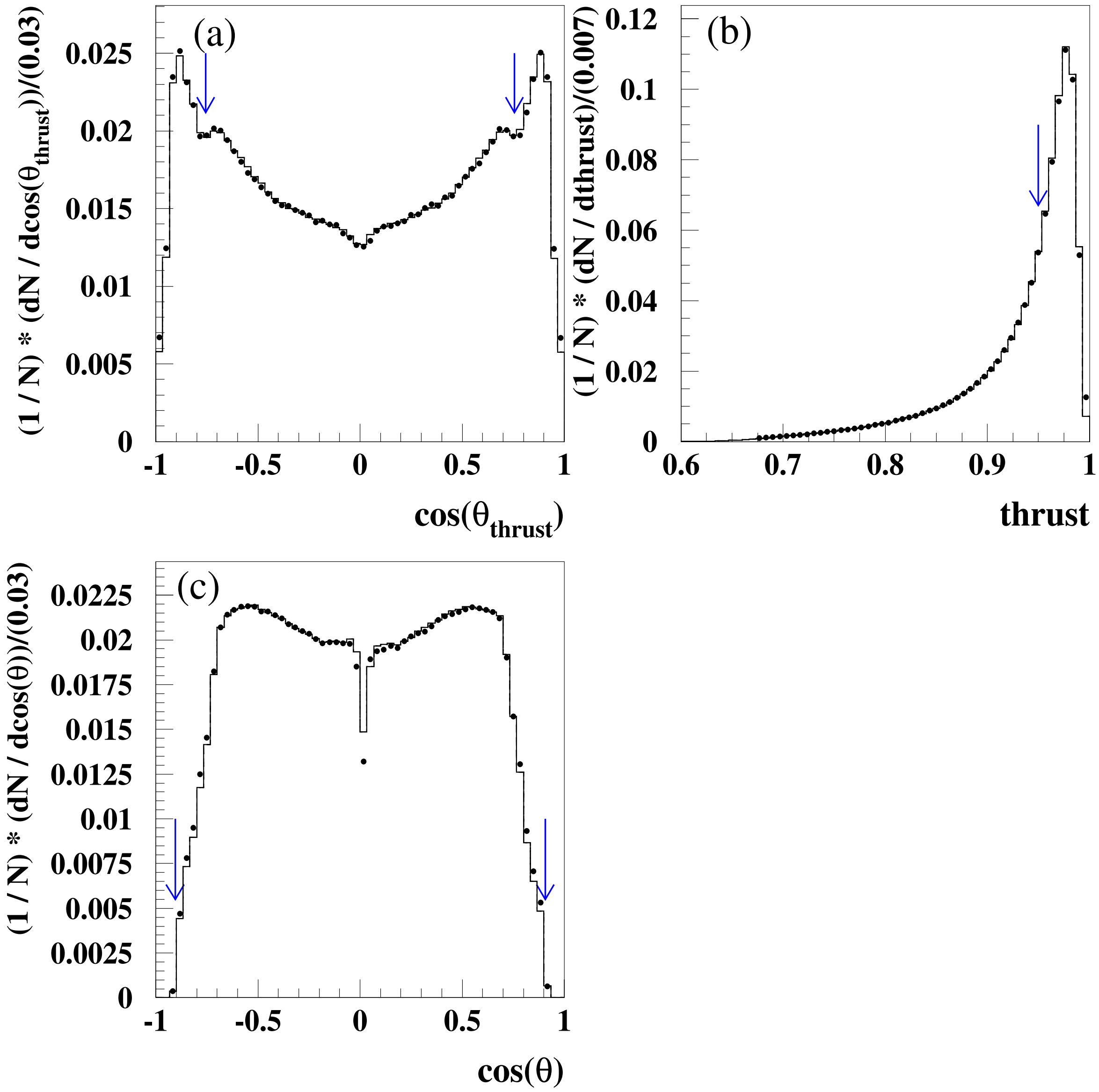

Figure 5.5: Distributions for pions: (a) cosine of the angle between the event thrust vector and the beam direction (θ_{thrust}), (b) thrust value and (c) cosine of the track polar angle in the laboratory frame (θ). Points denote distributions for the data, histograms for MC simulations, respectively. Blue arrows indicate the requirements applied in the selection.

Chapter 6

Study of Bose-Einstein correlations for $\pi^{\pm}\pi^{\pm}$ pairs

The present chapter describes the author's studies on azimuthal angle correlations of the same-sign charge pion pairs which were aimed at the determination of the transverse BEC radius. Preliminary results of the analysis have been presented as a contribution paper [74] to the EPS 2003[1].

The analysis was carried out using a substantial data sample of around 2.2×10^6 hadronic events collected by the DELPHI experiment (cf Sect. 5.3). Therefore, the study of the Bose-Einstein correlation function for identical particles could be performed with a satisfactory precision.

As has already been mentioned, the invariant $Q = \sqrt{-(q_1 - q_2)^2}$ (cf formula 2.16) is commonly applied in contemporary BEC analyses. The variable Q can be expressed in terms of particle transverse momentum magnitudes $q_{\perp 1}$, $q_{\perp 2}$, rapidities y_1, y_2 and azimuthal angles ϕ_1, ϕ_2:

$$Q = \sqrt{-2q_{\perp 1}q_{\perp 2}[\cosh(y_1 - y_2) - \cos(\phi_1 - \phi_2)]}. \tag{6.1}$$

For that reason the BEC effect observed in Q could also manifest itself in these observables. In the analysis presented below the correlation function is examined in differences of the above simple variables. Such a study has never been performed for the LEP data.

6.1 Definition of the reference frame

Kinematical variables describing a two-particle system, i.e. particle rapidities, transverse momenta and azimuthal angles were calculated in the reference frame determined by the event thrust axis. The Z-axis in this reference frame was parallel to the thrust axis, the Y-axis for each pair was directed towards one of the two $\vec{q}_\perp$ vectors, and the X-axis was orthogonal to both Y and Z. The azimuthal angle was defined in the range $-180° - 180°$. The azimuthal angle difference of the two tracks in the plane transverse to the thrust was calculated as the absolute value of the smallest angle between them. The only diffrence between the reference frame described above and the Longitudinal Center-of-Mass System (LCMS) (cf Sect. 3.2) was the absence of the rapidity boost which

[1] A draft of the publication containing the results described below is under the internal referee procedure of the DELPHI collaboration.

equalizes the longitudinal momenta of the tracks in the pair. It should be noted that the rapidities determined in LCMS have the same values but opposite signs. For that reason the rapidity difference cannot be examined in LCMS. Nevertheless, the azimuthal angle difference calculated in our system coincided with that calculated in the LCMS frame used in three-dimensional correlation radius studies.

The correlation functions were examined in the relative azimuthal angle $|\phi_1 - \phi_2|$, the rapidity difference $|y_1 - y_2|$ and the two transverse momentum magnitude difference $|q_{\perp 1} - q_{\perp 2}|$.

6.2 One-particle density distributions

The uncorrected one-particle density distributions of the azimuthal angle, rapidity and transverse momentum for pions in the data and MC simulation (BEC included), are presented in Fig.6.1, showing a satisfactory agreement between the data and MC distributions. A remarkable uniformity of the ϕ distribution (Fig.6.1a) may be noticed, indicating that the efficiency losses are unimportant for this variable. The single-particle distributions determined separately for positive and negative pions were found to be identical.

An acceptable agreement of the distributions in data and MC justified the application of the MC simulation for the calculation of the efficiency weights in order to correct the observed distributions for efficiency losses. The observed one-particle distributions were corrected for acceptance and reconstruction losses in each bin using the following weights:

$$W_{1p}(x) = \left(\frac{dN}{dx}\right)_{true} \Big/ \left(\frac{dN}{dx}\right)_{sim}, \tag{6.2}$$

where the index *true* denotes the generated distribution, while *sim* indicates the distribution after simulation of all detector effects, and $x = y, q_\perp$. The efficiency weights for the azimuthal angle distribution were found to be constant, therefore no corrections to this distribution were applied. Average values of the weights for rapidity and transverse momentum amount to:

$$\langle W_{1p}(y)\rangle = 2.1 \pm 0.7, \qquad \langle W_{1p}(q_\perp)\rangle = 2.7 \pm 0.5, \tag{6.3}$$

where the quoted errors stand for the RMS values of weights distributions. The normalised and corrected one-particle distributions of rapidity and transverse momentum are compared to uncorrected ones in Fig.6.2.

The weights for the y distribution are largest in the central rapidity region. The depletion in the observed distribution (cf Fig.6.2a) is mainly caused by the presence of thick metal plate electrode of the TPC. The corrected rapidity distribution agrees well with that obtained by the DELPHI collaboration in an earlier analysis [32]. The observed and corrected transverse momentum distributions agree well in the region of $q_\perp < 0.8$ GeV, therefore the efficiency corrections for the $q_\perp$ distribution are important only in the high $q_\perp$ region.

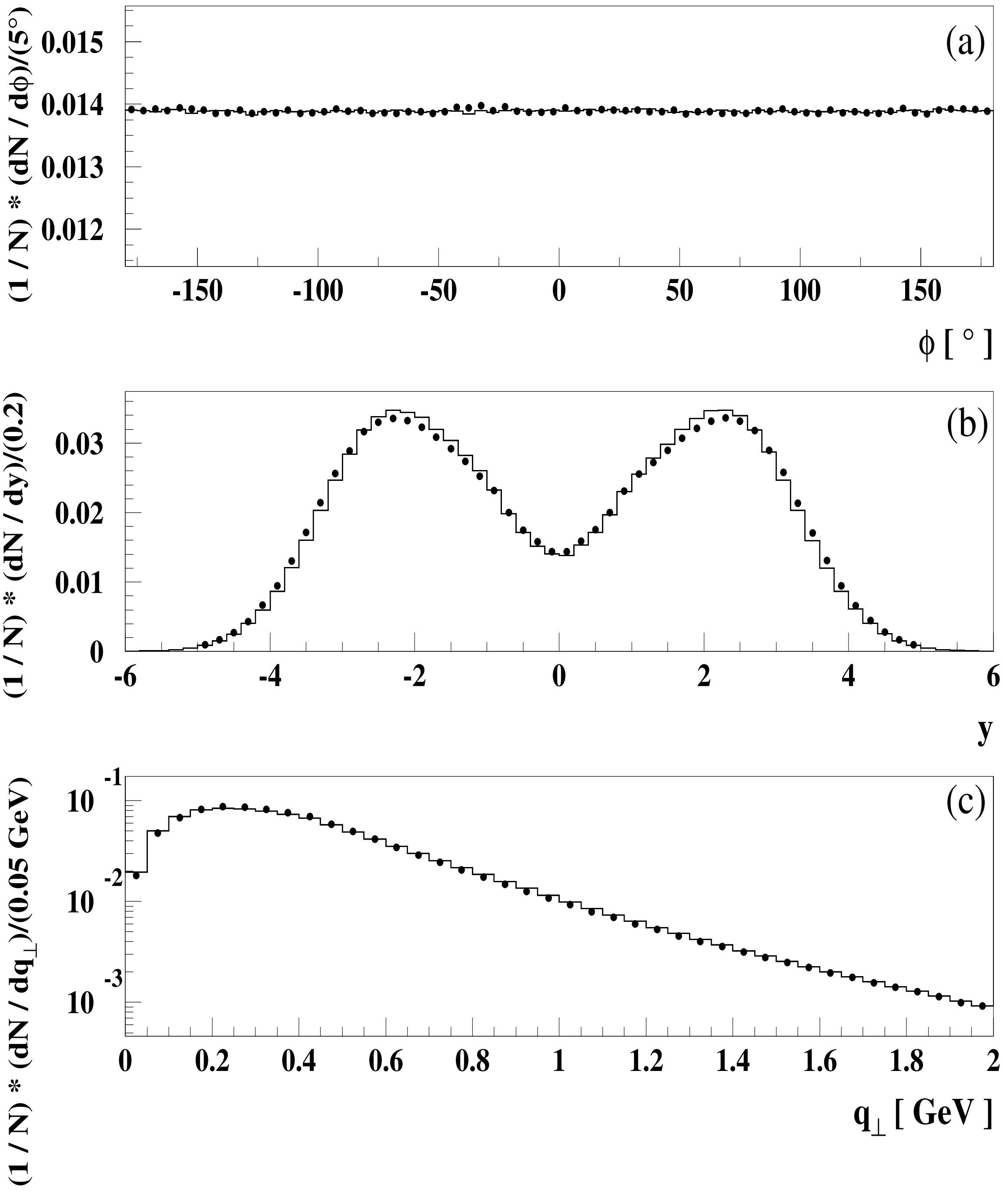

Figure 6.1: Uncorrected one-particle density distributions of (a) azimuthal angle, (b) rapidity and (c) transverse momentum. The variables were calculated in the event thrust reference frame defined in the text. Points correspond to the distributions for data and histograms to the MC simulations.

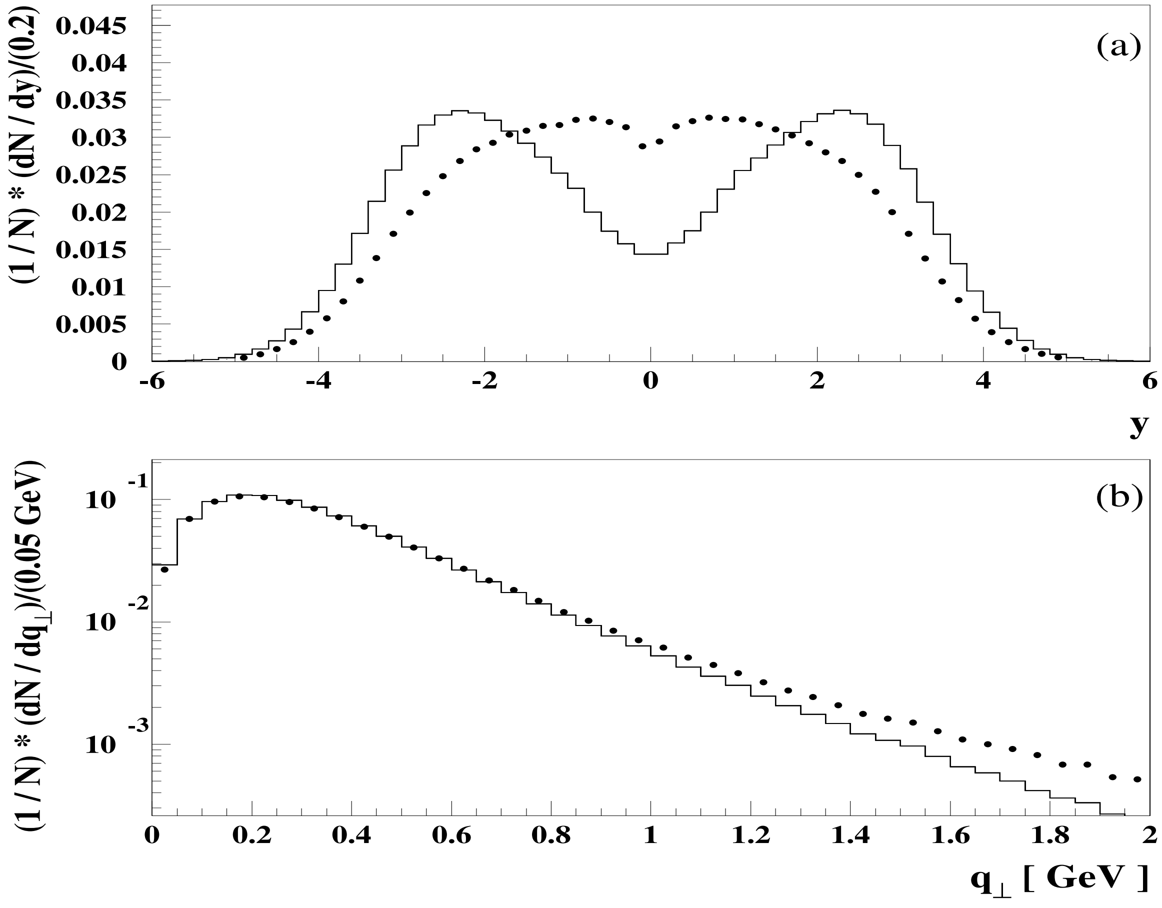

Figure 6.2: Corrected one-particle density distributions of (a) rapidity, (b) transverse momentum. Histograms stand for uncorrected data distributions, points denote corrected ones.

6.3 Two-particle density distributions

Two-particle distributions were constructed by pairing pions coming from the same event. Normalised and corrected two-particle density distributions of $\Delta\phi = |\phi_1 - \phi_2|$, $\Delta y = |y_1 - y_2|$ and $\Delta q_\perp = |q_{\perp 1} - q_{\perp 2}|$ for like-sign pion pairs are presented in Fig.6.3[2]. Corresponding distributions for unlike-sign pions are shown in Fig.6.4. Errors in the above-mentioned distributions were calculated neglecting any inter-bin correlations.

The two-particle distributions were corrected for efficiency employing the weights determined for one-particle distributions:

$$W_{2p}(\Delta x) = W_{1p}(x)W_{1p}(x), \tag{6.4}$$

where $x = y, q_\perp$. This correction procedure is to a lesser extent sensitive to the model assumptions associated with the two-particle correlations than the implementation of correction weights determined for two-particle distributions.

[2]Note that modules of $\vec{q}_\perp$ vectors were directly subtracted in the $\Delta q_\perp$ difference.

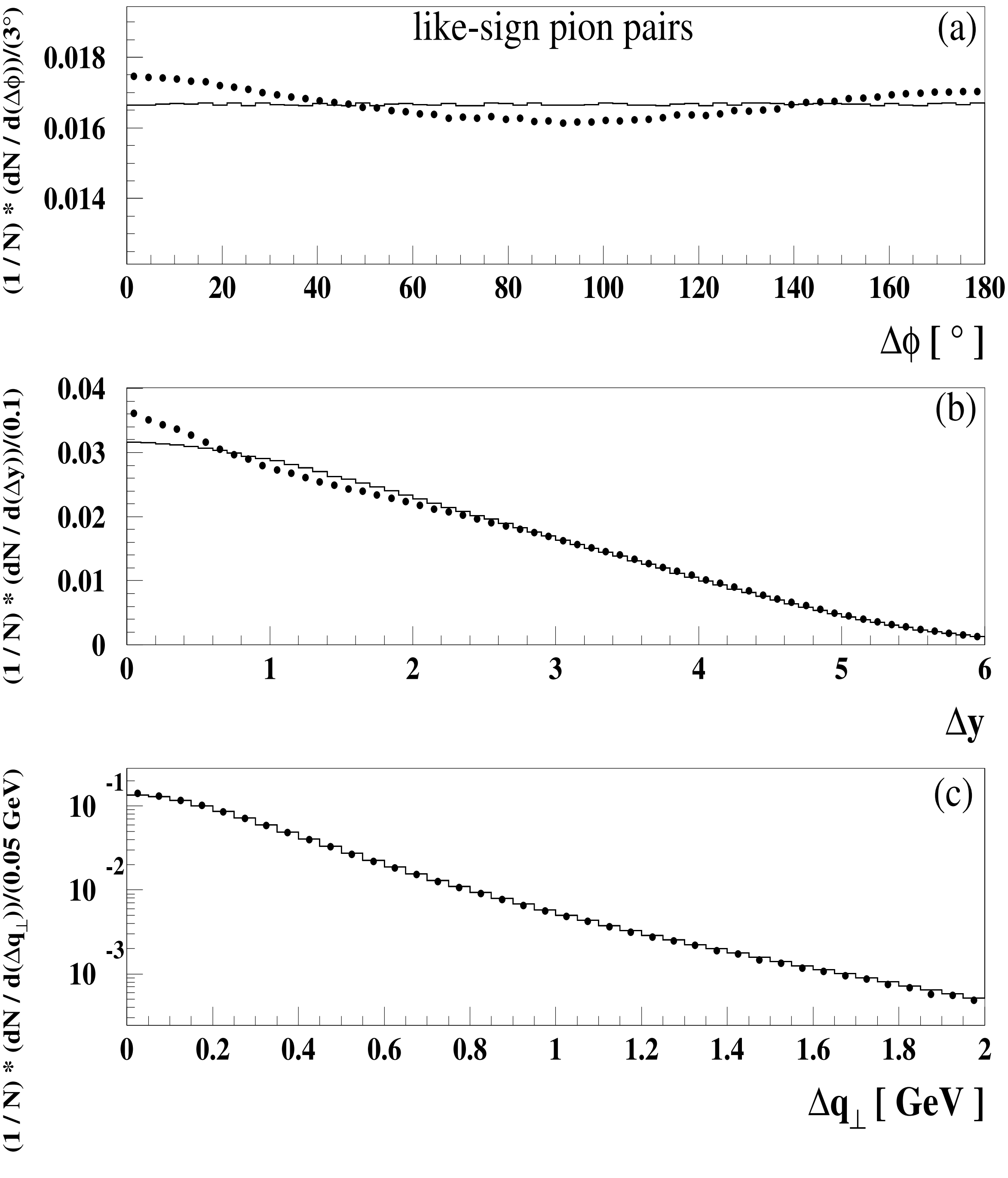

Figure 6.3: Corrected two-particle density distributions for like-sign pion pairs compared to uncorrelated distributions: (a) azimuthal angle difference, (b) rapidity difference and (c) transverse momentum magnitude difference. Points denote corrected distributions in data, histograms represent the product of one-particle distributions. Error bars are smaller than the plotted symbols.

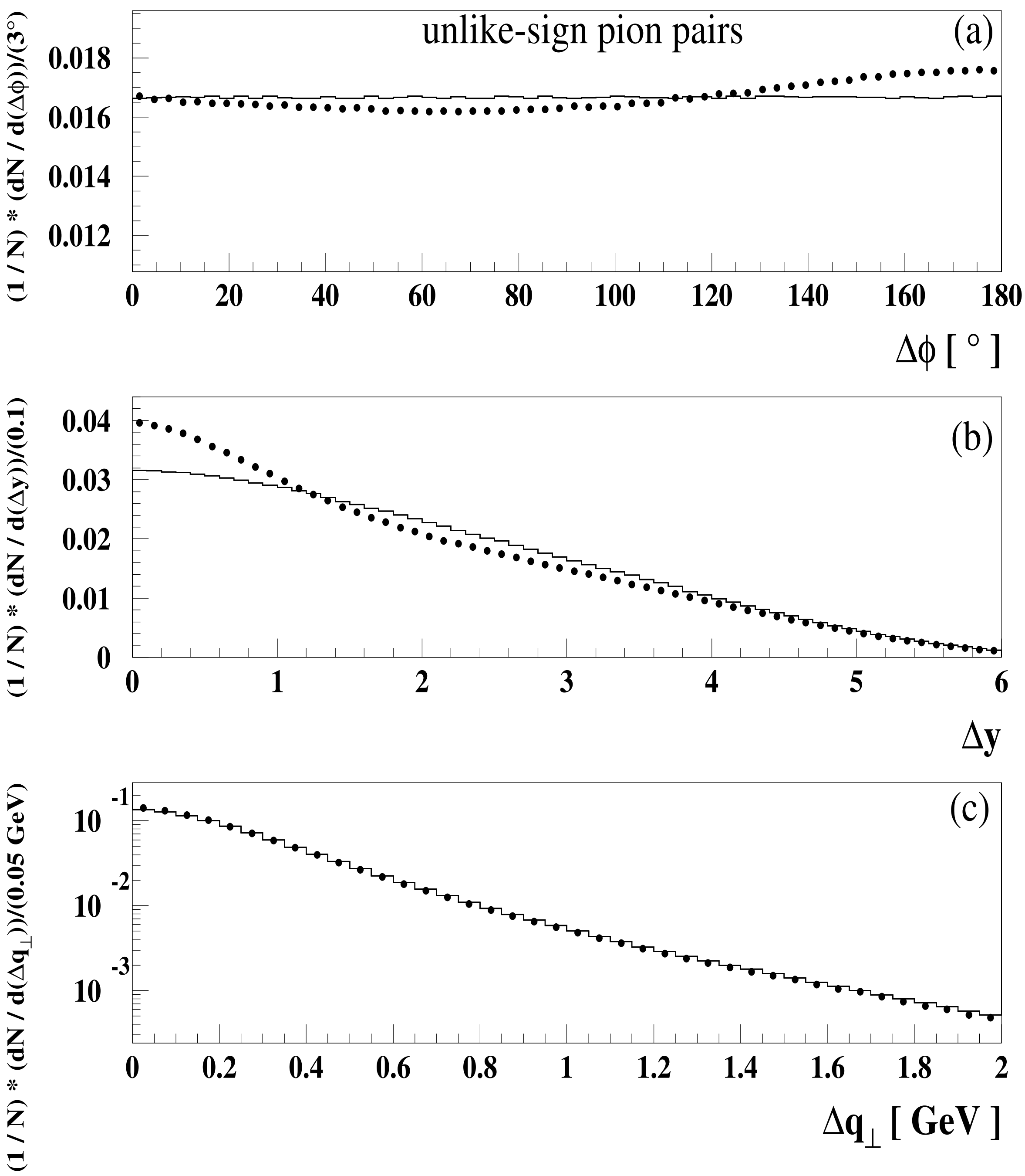

Figure 6.4: Corrected two-particle density distributions for unlike-sign pion pairs compared to uncorrelated distributions: (a) azimuthal angle difference, (b) rapidity difference and (c) transverse momentum magnitude difference. Points denote corrected distributions in data, histograms represent the product of one-particle distributions. Error bars are smaller than the plotted symbols.

The superimposed distributions in Fig.6.3 and Fig.6.4 represent the two-particle distributions arrived at by random drawing of variable pairs from the corresponding corrected one-particle density distributions. This approach is a practical realisation of 'the reference distribution', i.e. the product of two single-particle density distributions in the denominator of the correlation function expressed by formula (3.1). Such a construction yields reference distributions where all correlations are removed. Nevertheless, their properties may be dissimilar from the features of two-particle reference distribution, which is constructed by mixing tracks from different events or jets. For example, the above-mentioned distributions are less affected by the violation of energy-momentum conservation, since they are the result of randomising two measured one-particle distributions of a given variable, with one-particle distributions preserved, and all the remaining variables used to describe the particle system integrated out.

The $\Delta\phi$ and Δy distributions in data differ considerably from uncorrelated reference distributions. Clearly, one may observe a significant enhancement in the like-sign $\Delta\phi$ distribution over the uncorrelated one in the region of $\Delta\phi < 60°$ (Fig.6.3a), which is absent in unlike distributions (Fig.6.4a). The BEC effect, if present, contributes to the low $\Delta\phi$ region. The increase for $\Delta\phi > 120°$ in the $\Delta\phi$ distribution for unlike-sign pions (cf Fig.6.4a) may probably be attributed to the local $q_\perp$ compensation. A minor enhancement for $\Delta\phi \approx 180°$ in both like-sign and unlike-sign distributions is expected due to the effect of limited $q_\perp$ phase-space [75].

The Δy distribution for like-sign pions (cf Fig.6.3b) exhibits an enhancement over the uncorrelated distribution in the region of $\Delta y < 0.6$, while both distributions converge if $\Delta y > 2.2$. A more evident effect was observable in the unlike-sign distribution (cf Fig.6.4b) at small Δy. The BEC effect might possibly contribute to a low Δy region in the like-sign pions distribution. The unlike Δy distribution suggests that other correlations also bear significance in this region. Therefore, disentangling the BEC in this variable may be problematic.

Both $\Delta q_\perp$ distributions, for like- and unlike-sign pions, agree well with the uncorrelated distribution across the entire measured range.

The two-particle distributions measured are compared to the JETSET 7.3 predictions for like- (Fig.6.5) and unlike-sign (Fig.6.6) pion pairs. Histograms as well as red lines represent MC distributions at the generator level, where histograms denote the MC distributions with the BEC effect modelled using the LUBOEI algorithm, whereas red lines indicate the MC distributions without BEC. Both like and unlike-sign data distributions agree very well with the respective MC distributions when the BEC effect is simulated.

The like-sign $\Delta\phi$ distribution in the data disagrees with the distribution in the MC sample with no BEC effect simulated (cf Fig.6.5a). The MC distribution was fairly flat for small $\Delta\phi$, being similar to the uncorrelated reference distribution from Fig.6.3a. Moreover, it overestimates also the enhancement for high $\Delta\phi$.

The unlike-sign Δy distribution (cf Fig.6.6b) agrees well with both MC predictions. However, a certain disagreement with no-BEC MC prediction may be noticed in the like-sign distribution for $\Delta y < 1$.

Shapes of the $\Delta q_\perp$ distributions (cf Fig.6.5c and Fig.6.6c) are acceptably well reproduced by both MC models, although some discrepancies exist in the tail ($q_\perp > 1.5$ GeV) of the distributions.

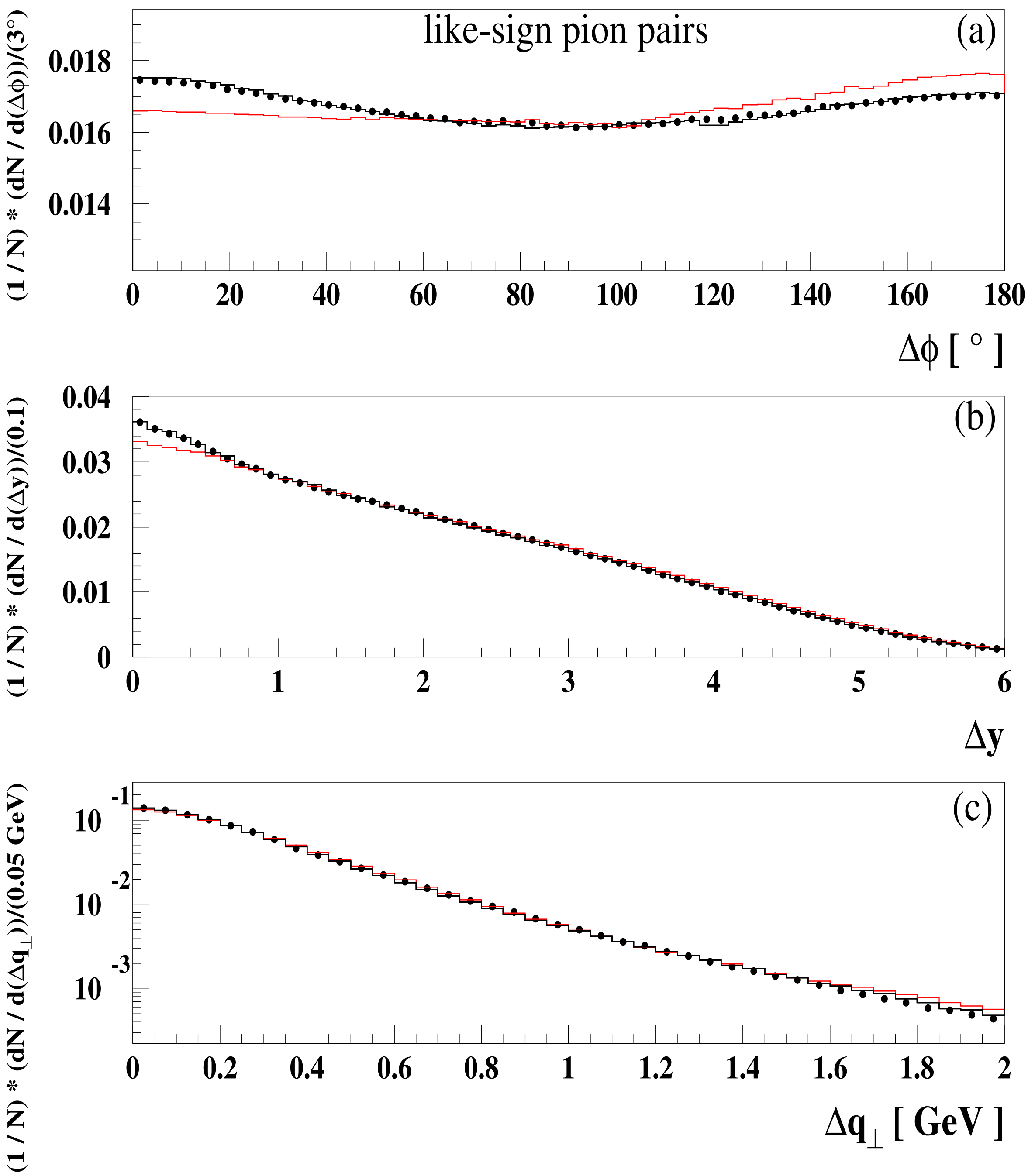

Figure 6.5: Corrected two-particle density distributions for like-sign pion pairs compared to the MC prediction with and without BEC: (a) azimuthal angle difference, (b) rapidity difference and (c) transverse momentum magnitude difference. Points denote corrected distributions in data, histograms stand for MC with BEC, red lines represent MC without BEC.

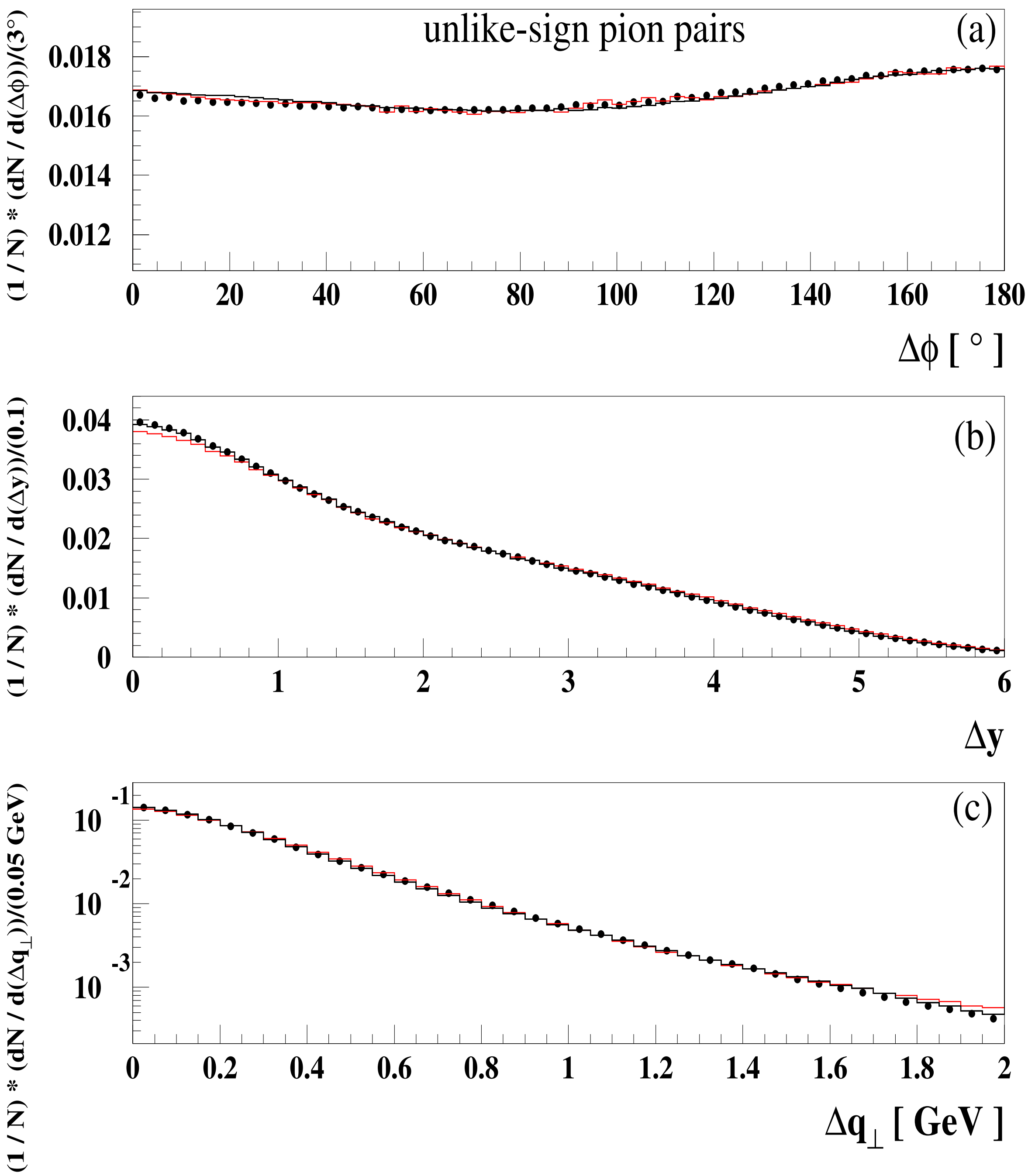

Figure 6.6: Corrected two-particle density distributions for unlike-sign pion pairs compared to the MC prediction with and without BEC: (a) azimuthal angle difference, (b) rapidity difference and (c) transverse momentum magnitude difference. Points denote corrected distributions in data, histograms stand for MC with BEC, red lines represent MC without BEC.

6.4 Determination of the correlation function

Formula (3.1) was employed to derive correlation functions $C_2(\Delta\phi)$, $C_2(\Delta y)$ and $C_2(\Delta q_\perp)$ from the above-mentioned one- and two-particle density distributions. These functions are presented for like- and unlike-sign pion pairs in Fig.6.7 and Fig.6.8, respectively. Again, the JETSET 7.3 predictions with (histograms) and without (red lines) the BEC effect are superimposed.

Similarily to the two-particle distributions, the MC model with the BEC effect simulated reproduces accurately correlation functions in $\Delta\phi$, Δy and $\Delta q_\perp$ for like- and unlike-sign pion pairs.

Differences between the Δy and $\Delta q_\perp$ distributions in data and MC predictions without BEC, observed already in the two-particle distributions, are presently enhanced in the Δy and $\Delta q_\perp$ correlation functions.

As has been mentioned in Sect. 3.1, the method frequently used in the BEC analyses to account for imperfections of the MC simulation is a double ratio, defined in this case as a ratio of the correlation function in the data and the respective correlation function in the MC model without the BEC effect. The double ratios of $\Delta\phi$, Δy and $\Delta q_\perp$ are shown in Fig.6.9 for like- and in Fig.6.10 for unlike-sign pion pairs. To a certain extent, they allow for the correction of the correlation function in respect of differences between the data and the MC simulation. On the other hand, they may introduce model dependencies to the measurement. It should be also noted that in the past analyses only a part of the Q phase-space was studied, and the correlation functions were often determined by normalising the corresponding two-particle distributions to some arbitrary common point far away from the correlation region. In the present analysis, we attempted to analyse the correlations in the whole measured variable ranges and no common normalisation of the distributions is performed. The above-mentioned double ratios were used only as a subsequent consistency check of the results.

The double ratios of the correlation functions in $\Delta\phi$ for like-sign data (cf Fig.6.9a) display the short-range BEC effect followed by negative correlations, whereas in the case of unlike-sign data (Fig.6.10a) such correlations are absent. The BEC-like effect may also be observed in the double ratio of the like-sign correlation functions in Δy (Fig.6.9b). In addition, the unlike-sign double ratio includes also some weaker positive correlations for Δy (Fig.6.10b). Certain correlations for low $\Delta q_\perp$ may be observed in both double ratios for like- (cf Fig.6.9c) and unlike-sign (Fig.6.10c) pion pairs, followed by the onset of negative correlations in the tails.

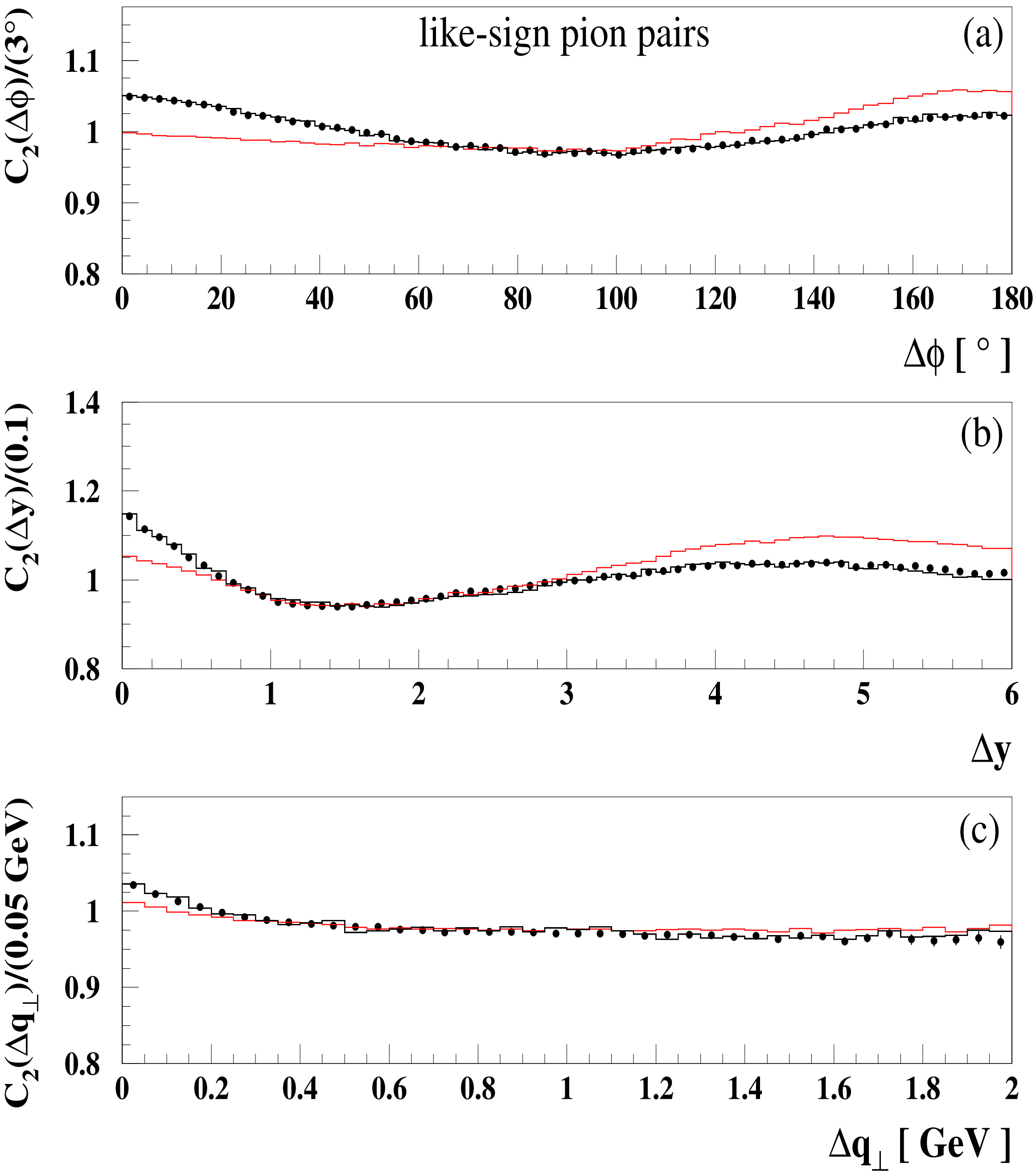

Figure 6.7: Correlation functions $C_2(\Delta\phi)$, $C_2(\Delta y)$ and $C_2(\Delta q_\perp)$ (cf formula (3.1)) for like-sign pion pairs compared to the MC prediction with and without BEC: (a) azimuthal angle difference, (b) rapidity difference and (c) transverse momentum magnitude difference. Points denote the data, histograms stand for MC simulations with BEC, red lines represent MC without BEC.

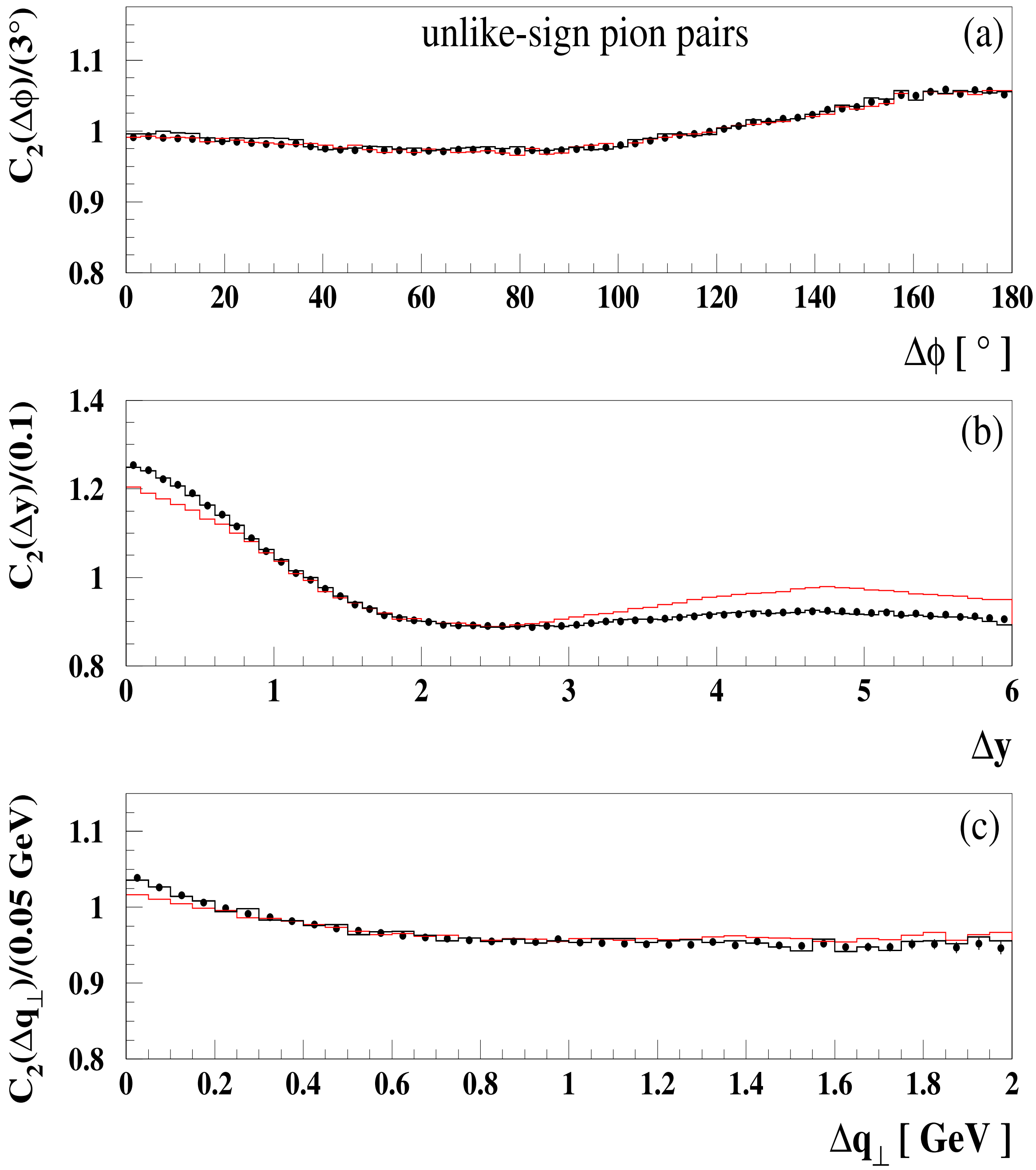

Figure 6.8: Correlation functions $C_2(\Delta\phi)$, $C_2(\Delta y)$ and $C_2(\Delta q_\perp)$ (cf formula (3.1)) for unlike-sign pion pairs compared to the MC prediction with and without BEC: (a) azimuthal angle difference, (b) rapidity difference and (c) transverse momentum magnitude difference. Points denote the data, histograms stand for MC simulations with BEC, red lines represent MC without BEC.

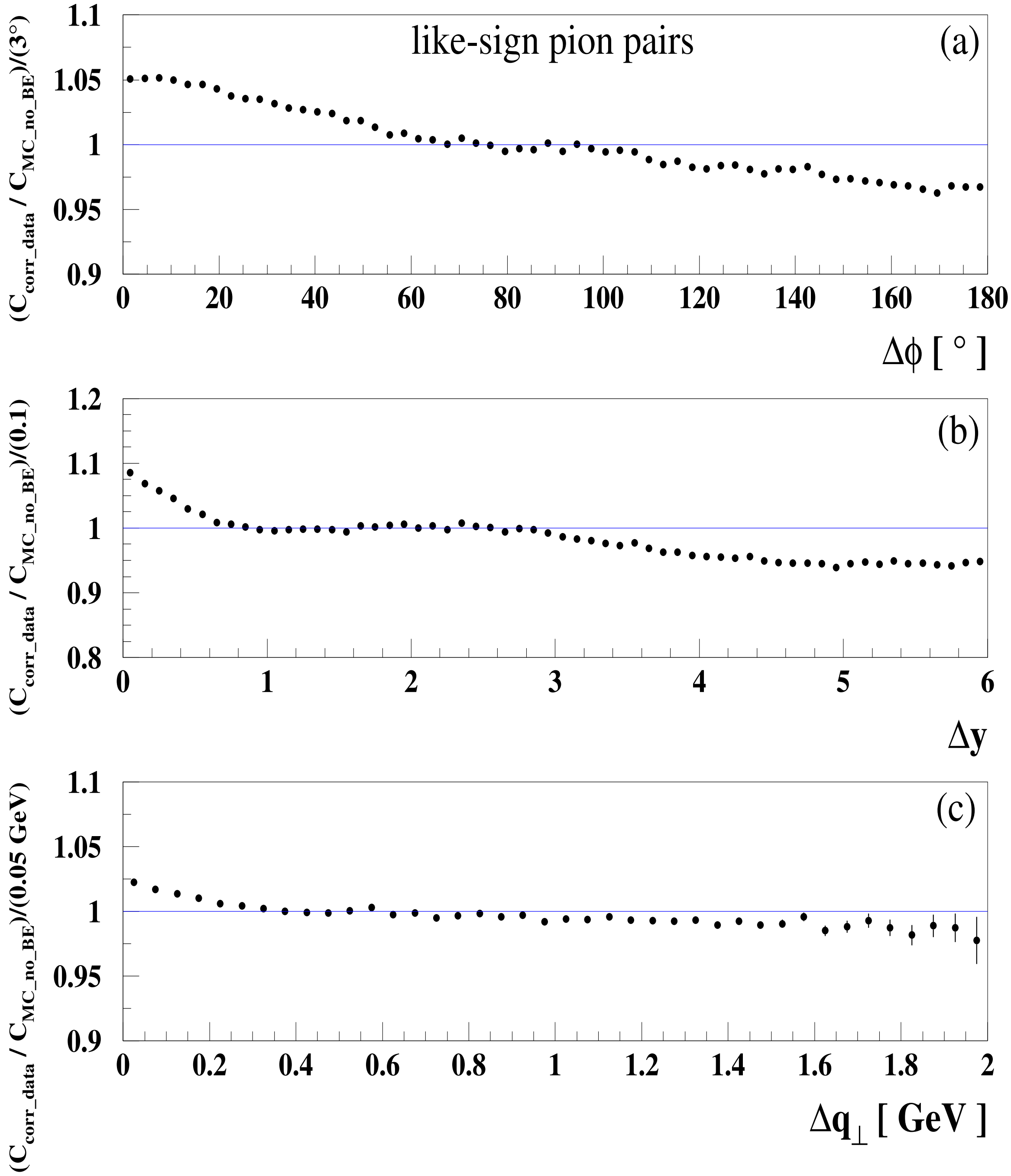

Figure 6.9: Correlation function ratios (Data/MC without BEC, cf formula (3.2)) for like-sign pion pairs in: (a) azimuthal angle difference, (b) rapidity difference and (c) transverse momentum magnitude difference.

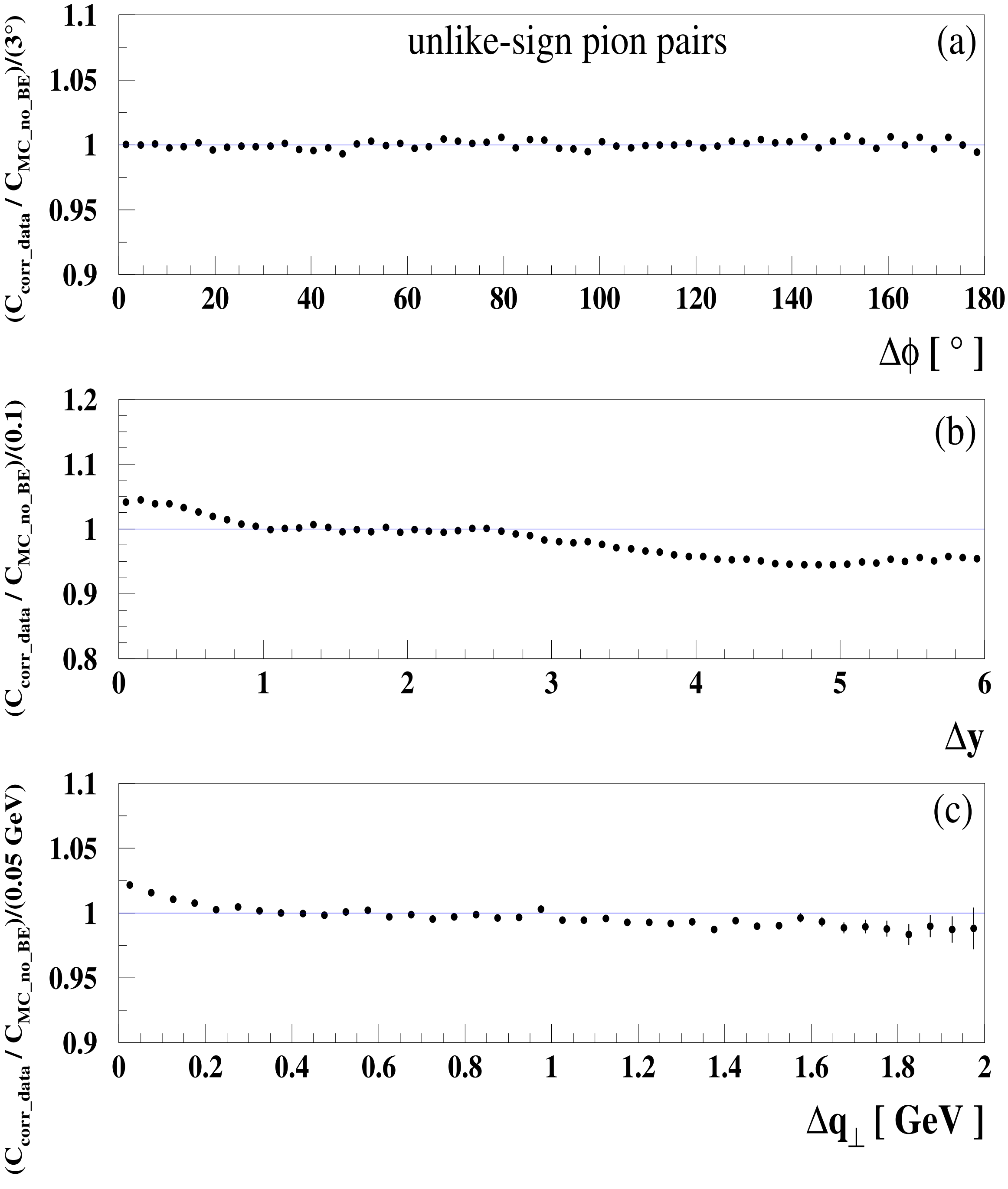

Figure 6.10: Correlation function ratios (Data/MC without BEC, cf formula (3.2)) for unlike-sign pion pairs in: (a) azimuthal angle difference, (b) rapidity difference and (c) transverse momentum magnitude difference.

6.5 Determination of the transverse correlation radius

A fit to the correlation function $C_2(\Delta\phi)$ for like-sign pion pairs (cf Fig. 6.11) was performed to estimate the width of the enhancement observed for $\Delta\phi < 60°$. The Goldhaber parametrisation (2.20) was assumed to describe this enhancement, while the correlations observed at large $\Delta\phi$ were parametrised by the polynomial term. The following formula was adopted to fit the entire $\Delta\phi$ range:

$$C_2(\Delta\phi) = N\Big(1 + \lambda \exp\left(-R^2_{\Delta\phi}(\Delta\phi)^2\right)\Big) \cdot \Big(1 + k\sum_{i=0}^{6} a_i(\Delta\phi)^i\Big), \qquad (6.5)$$

where N, λ, k and $R_{\Delta\phi}$ (in rad^{-1}) stand for free parameters of the fit. The coefficients a_i in the polynomial term were fixed to the values determined by fitting the shape of the MC like-sign correlation function $C_2(\Delta\phi)$ without the BEC effect (Fig.6.11b). The free parameter k was introduced to account for a fraction of long-range correlations present in the data. Minimalisation of the χ^2 function was performed using the MINUIT package [76]. The result of the fit is shown in Fig.6.11a as a red line superimposed on the measured correlation function. The fitted parameters are listed in Table 6.1.

Table 6.1: Results of the fit to the acceptance corrected correlation function $C_2(\Delta\phi)$ for like-sign pion pairs using parametrization (6.5).

$R_{\Delta\phi}$	(1.255 ± 0.029) rad^{-1}
λ	0.078 ± 0.001
N	0.505 ± 0.004
k	0.913 ± 0.011
χ^2/ndf	60/56

A number of tests were conducted in order to examine sensitivity of the fitted parameters to the parametrisation of long-range correlations. Instead of the polynomial parametrisation the Gaussian and trigonometric functions were applied to describe the MC distribution in Fig.6.11b. In another test, the shape of the long-range correlation contribution was taken from the correlation function for unlike-sign data or Monte Carlo samples. The correlation function $C_2(\Delta\phi)$ for like-sign pions was also fitted in the region of $\Delta\phi < 90°$ with the Goldhaber term alone. All the above cross-checks proved that the changes of the fit parameters to the variations of the long-range correlation component are much smaller than the systematic errors from other sources.

The fitted parameter $R_{\Delta\phi}$ corresponds to the angular dimension of the source of $1/R_{\Delta\phi} = 0.797 \pm 0.018$ rad. For Gaussian sources described in a transverse momentum space by $\exp\left(-R^2_\perp Q^2_\perp\right)$, it can be related to the source transverse radius $R_\perp$ using the following derivation:

$$\begin{aligned}\exp\left(-R^2_\perp(\vec{q}_{\perp 1} - \vec{q}_{\perp 2})^2\right) &= \exp\left(-R^2_\perp(q^2_{\perp 1} + q^2_{\perp 2} - 2q_{\perp 1}q_{\perp 2}\cos\Delta\phi)\right) \\ &= C_1 \exp\left(2R^2_\perp q_{\perp 1}q_{\perp 2}\cos\Delta\phi\right), \end{aligned} \qquad (6.6)$$

where $C_1 = \exp\left[-R^2_\perp(q^2_{\perp 1} + q^2_{\perp 2})\right]$. Using the approximation $\cos(\Delta\phi) \approx 1 - \frac{(\Delta\phi)^2}{2}$, the exponent from formula (6.6) assumes the form:

$$C_1 \exp\left(2(R^2_\perp q_{\perp 1}q_{\perp 2} - R^2_\perp q_{\perp 1}q_{\perp 2}\Delta\phi^2)\right). \qquad (6.7)$$

Averaging over $q_{\perp i}$ and applying the approximation $\langle q_{\perp 1}\rangle \langle q_{\perp 2}\rangle \approx \langle q_{\perp}\rangle^2$ to formula (6.7) one obtains:

$$\begin{aligned} C_1 C_2 \exp\left(-R_\perp^2 \Delta\phi^2 \langle q_\perp\rangle^2\right) &= C \exp\left(-R_\perp^2 \langle q_\perp\rangle^2 \Delta\phi^2\right) \\ &= C \exp\left(-R_{\Delta\phi}^2 \Delta\phi^2\right). \end{aligned} \tag{6.8}$$

C_1, $C_2 \approx \exp(2)\exp(2R_\perp^2 q_{\perp 1} q_{\perp 2})$ as well as $C = C_1 C_2$ represent terms independent of $\Delta\phi$. The two approximations adopted to determine the above relation introduce negligibly small errors on $R_\perp$ as compared to other systematic errors. Thus, formula (6.8) yields:

$$R_\perp = \frac{R_{\Delta\phi}}{\langle q_\perp\rangle} = 0.591 \pm 0.015(stat)\,\mathrm{fm}, \tag{6.9}$$

where $\langle q_\perp\rangle$ represents the mean value of measured transverse momentum distribution, $R_{\Delta\phi}$ is expressed in radians. The value of $\langle q_\perp\rangle$ was determined on the basis of the corrected $q_\perp$ distribution for data, to be 416.6 ± 14.7 MeV, where the quoted error was derived from the RMS value of the distribution.

Systematic errors of the $R_\perp$ ($R_{\Delta\phi}$) determination were estimated by varying the fitted $\Delta\phi$ range as well as by assuming different parametrisations of long-range correlations, by applying different selection criteria and analysing the effects of efficiency weights. The results of the systematic effects analysis are listed in Table 6.2. Three dominant contributions to the systematic error of $R_\perp$ ($R_{\Delta\phi}$) were due to the requirement imposed on the thrust value, range of the polar angle θ as well as determination of the average value of $q_\perp$. The influence of the constraint imposed on minimum value of momentum was examined by varying the range from 100 to 400 MeV. No significant variation of $R_{\Delta\phi}$ was detected. The contribution to the systematic error of $R_\perp$ was assessed on the basis of the change in the mean value of the uncorrected and corrected $q_\perp$ distribution. The effects related to double-track angular resolution and track splittings were studied by removing all pairs with an opening angle below $2°$. The influence on $R_{\Delta\phi}$ and $R_\perp$ turned out to be insignificant. The requirement that particles in the pair originate from the same jet was also imposed, leading to the increase in the enhancement of the like-sign $\Delta\phi$ distribution for $\Delta\phi < 60°$. The obtained value of $R_{\Delta\phi}$ amounts to 1.304 ± 0.031 rad^{-1}, which agrees within erros with the present result.

The maximum variation of $R_{\Delta\phi}$ and $R_\perp$ in a given test, with respect to the result given in the Table 6.1 and in formula (6.9), was taken as an estimate of the systematic error contribution. The total systematic error value was obtained by summing in quadrature individual contributions.

Finally, the determination of $R_{\Delta\phi}$ yielded:

$$R_{\Delta\phi} = 1.255 \pm 0.029(stat) \pm 0.060(syst)\,\mathrm{rad}^{-1}, \tag{6.10}$$

which corresponds to the source angular dimension of

$$1/R_{\Delta\phi} = 0.797 \pm 0.018(stat) \pm 0.038(syst)\,\mathrm{rad}, \tag{6.11}$$

and the transverse source radius:

$$R_\perp = 0.591 \pm 0.015(stat) \pm 0.034(syst)\,\mathrm{fm}. \tag{6.12}$$

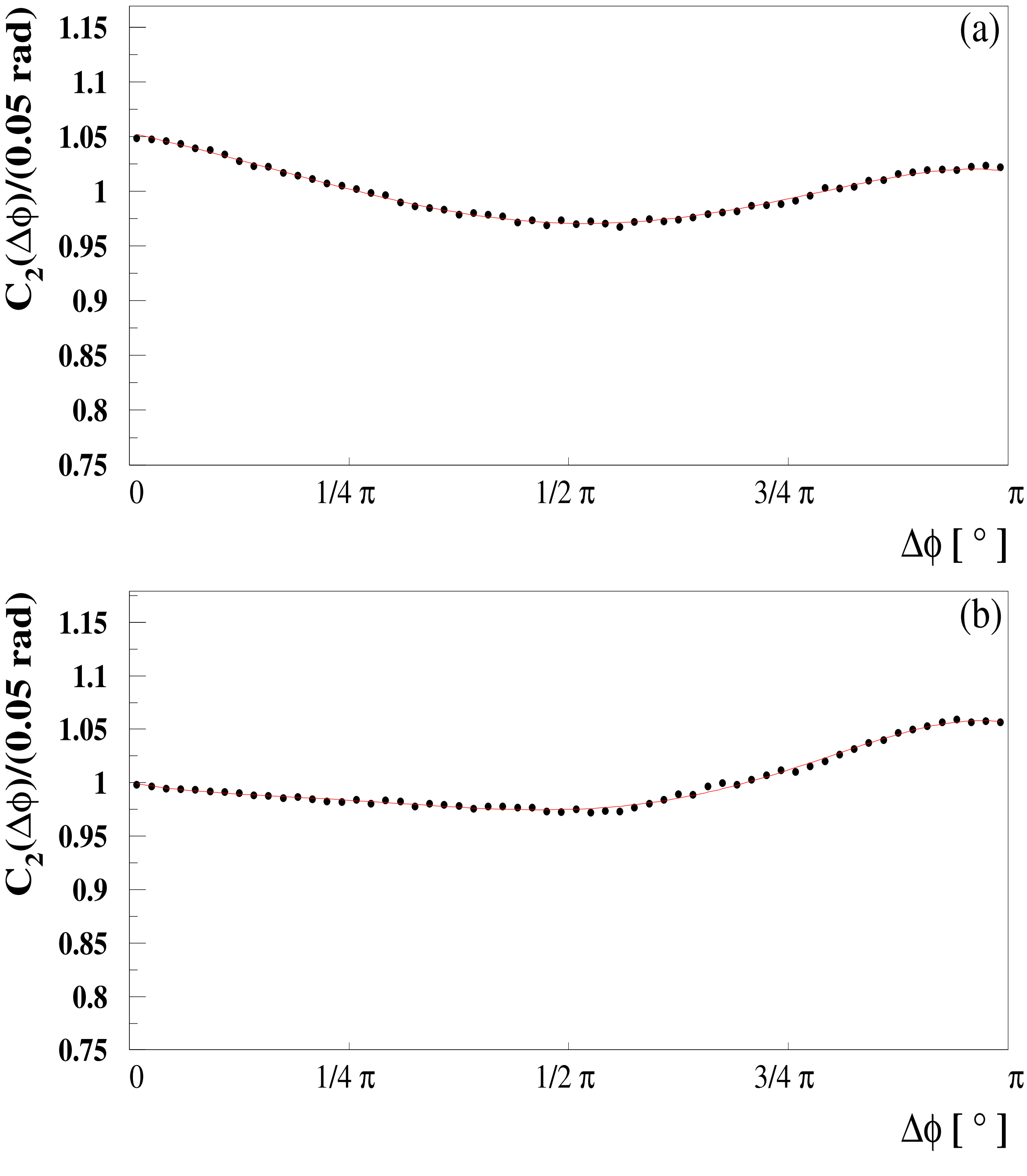

Figure 6.11: Fit to the correlation function $C_2(\Delta\phi)$ for like-sign pion pairs: (a) points represent data and the red solid line shows the fit result using parametrisation described in the text; (b) points correspond to MC without the BEC effect and the red solid line to the fit result using parametrization described in the text.

Table 6.2: Contributions to the systematic error of $R_{\Delta\phi}$ and $R_{\perp}$. Numbers in parentheses refer to the range in which the respective parameters were varied.

systematic error source	$\Delta R_{\Delta\phi}$ [rad^{-1}]	$\Delta R_{\perp}$ [fm]
$\Delta\phi$ range, diff. parametrisations	0.008	0.004
thrust^{min} requirement (0.91−0.98)	0.044	0.021
$\|cos\theta\|^{max}$ requirement (0.69−0.97)	0.036	0.017
$\|cos\theta_{thrust}\|^{max}$ requirement (0.66−0.84)	0.017	0.008
$\langle q_{\perp}\rangle$ determination	−	0.021
total systematic error	0.060	0.034

The above result agrees well with transverse radii determined in other LEP analyses (cf Fig. 6.12). The resulting small value of the incoherence parameter λ may be linked to the fact that the BEC effect is partially eliminated by the integration over the remaining kinematical variables which describe the two-particle system. This effect was observed in the BEC studies at CPLEAR [77]. On the other hand, the BEC effect in $\Delta\phi$ occupies a large fraction of the allowed phase-space. The integral of the BEC enhancement corresponds to ~7% of the total sample. This number agrees with the fraction of events showing the BEC effect in Q-variable analyses [58, 78].

6.6 Conclusions

The Bose-Einstein correlations in variables $\Delta\phi$, Δy and $\Delta q_{\perp}$ were examined by analysing two-particle density distributions and correlation functions for like- and unlike-sign pion pairs. The JETSET 7.3 PS generator with the BEC effect implemented gives acceptable description of the two-particle distributions as well as the correlation functions. Strong enhancement in the correlation function is observed in $\Delta\phi < 60°$, which may be attributed to the short range Bose-Einstein correlations. The BEC effect occurs in the low $\Delta\phi$ region where the uncorrelated distribution is flat, similarily to the distributions for unlike-sign pairs in the data and the MC prediction without the BEC effect. We attributed the observed correlations to BEC and determined the angular dimension of the pion source as given in formula (6.11) and the transverse correlation radius presented in formula (6.12). The present result, as shown in Fig.6.12, is in agreement with other LEP measurements obtained using different methods and it supports LEP's evidence for different values of the source radius in longitudinal and the transverse directions.

The onset of short range positive correlations is also noticeable in Δy for like-sign pions. This effect can partially be attributed to BEC. The correlations in $\Delta q_{\perp}$ were found to be weak.

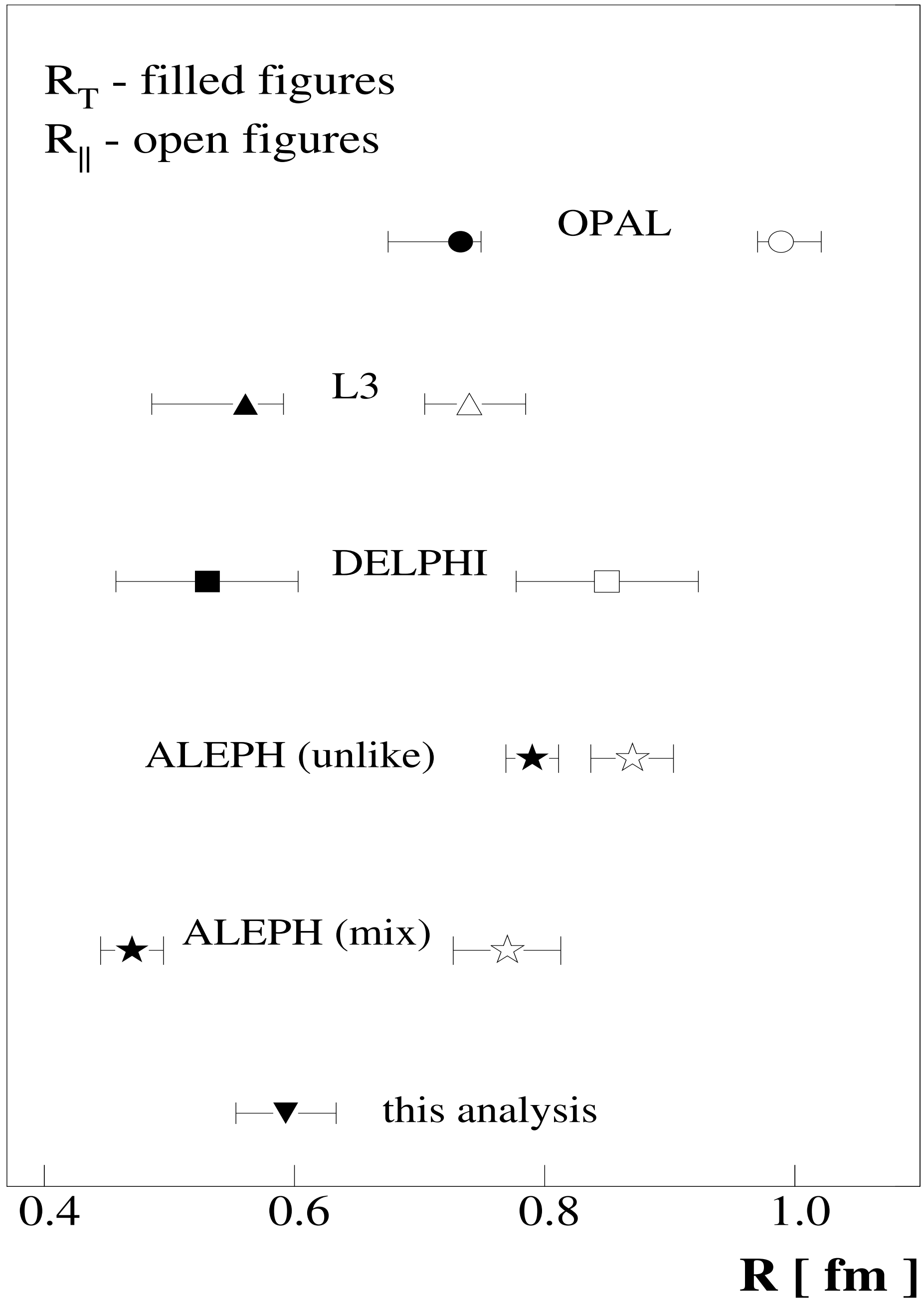

Figure 6.12: Results of two- and three-dimensional analyses of LEP data for radii $R_{\parallel}$ and $R_{\perp}$, as defined in formula (3.6). For L3 and OPAL results the $R_{\perp}$ is derived according to formula $\sqrt{(R^2_{t,out} + R^2_{t,side})/2}$, where $R_{t,out}$ and $R_{t,side}$ are defined in Sect. 3.2.

Chapter 7

Study of Fermi-Dirac correlations for $\bar{p}\bar{p}$ pairs

As has been mentioned in Sect. 2.3, the application of two-boson correlations to the measurement of spatiotemporal size of the hadron source may be extended to the analysis of identical fermion pairs. Due to the Pauli exclusion principle, identical fermions cannot occupy the same quantum state. For that reason, we expect a decrease in the probability distribution of the production of identical fermions nearby in space-time, attributed to the Fermi-Dirac correlation effect. Taking into consideration the range of the above-mentioned depletion it is possible to extract the information about the space-time properties of hadronic sources using the standard technique which employs the variable defined as the difference between four-momenta of two identical particles $Q = \sqrt{-(q_1 - q_2)^2}$ (cf formula 2.16). Studies on the correlation function as defined in formula (3.1) allow for the estimation of the correlation radius of identical fermions source.

This chapter describes in brief the outcome of the author's studies focused on the Fermi-Dirac correlations of two antiprotons produced in hadronic Z^0 events. Preliminary results of the analysis have been presented in contribution papers to the Rencontres de Moriond 2004 [79] and the ICHEP 2004 [80] conferences[1], including the author's presentation at the Rencontres de Moriond 2004 [81].

Following the discussion of essential one- and two-particle distributions in data as well as their comparison with MC distributions, the chapter will present the construction of the correlation function based on various reference samples.

7.1 One- and two-particle distributions relevant to the analysis

The selection described in Sect. 5.3 yielded about 1,000 $\bar{p}\bar{p}$ pairs for the analysis in data, and about 3,000 $\bar{p}\bar{p}$ pairs in the JETSET simulated MC sample. Detailed information about the number of pp, $\bar{p}\bar{p}$ and $p\bar{p}$ pairs in data and MC samples (mixed samples for data and MC, correspondingly) is collected in Table 7.1.

One-particle distributions of the momentum for protons and antiprotons in data and Monte Carlo are shown in Fig.7.1. An acceptable consistency between the data and

[1] A draft of the publication, containing the results discussed below, is currently in the internal referee procedure of the DELPHI collaboration.

Table 7.1: Number of pp, $\bar{p}\bar{p}$ and $p\bar{p}$ pairs in data, MC as well as mixed samples for data and MC.

	DATA	MC	DATA-MIX	MC-MIX
pp	$1,325$	$4,767$	$4,708$	$20,173$
$\bar{p}\bar{p}$	955	$3,358$	$3,968$	$15,409$
$p\bar{p}$	$6,473$	$26,355$	–	–

MC (at the level of 10−15%) may be observed, in particular for the momenta below ∼8 GeV. Small underestimation of the data by MC is noticeable for $|\vec{q}| \in$(8−20) GeV for both protons and antiprotons. It may be partially the result of an insufficient secondary interaction rate in MC, due to the underestimation of detector's material. Nevertheless, that underestimation is nearly the same for protons and antiprotons, that is why another explanation would be an imperfect baryon production modelling in JETSET. The decrease at $|\vec{q}| \sim 8$ GeV results from the kaon identification threshold in the gas RICH, whereas a similar depletion at $|\vec{q}| \sim 20$ GeV from the respective proton identification threshold.

Distributions of the cosine of opening angle θ in the thrust reference frame (cf Sect. 3.1)

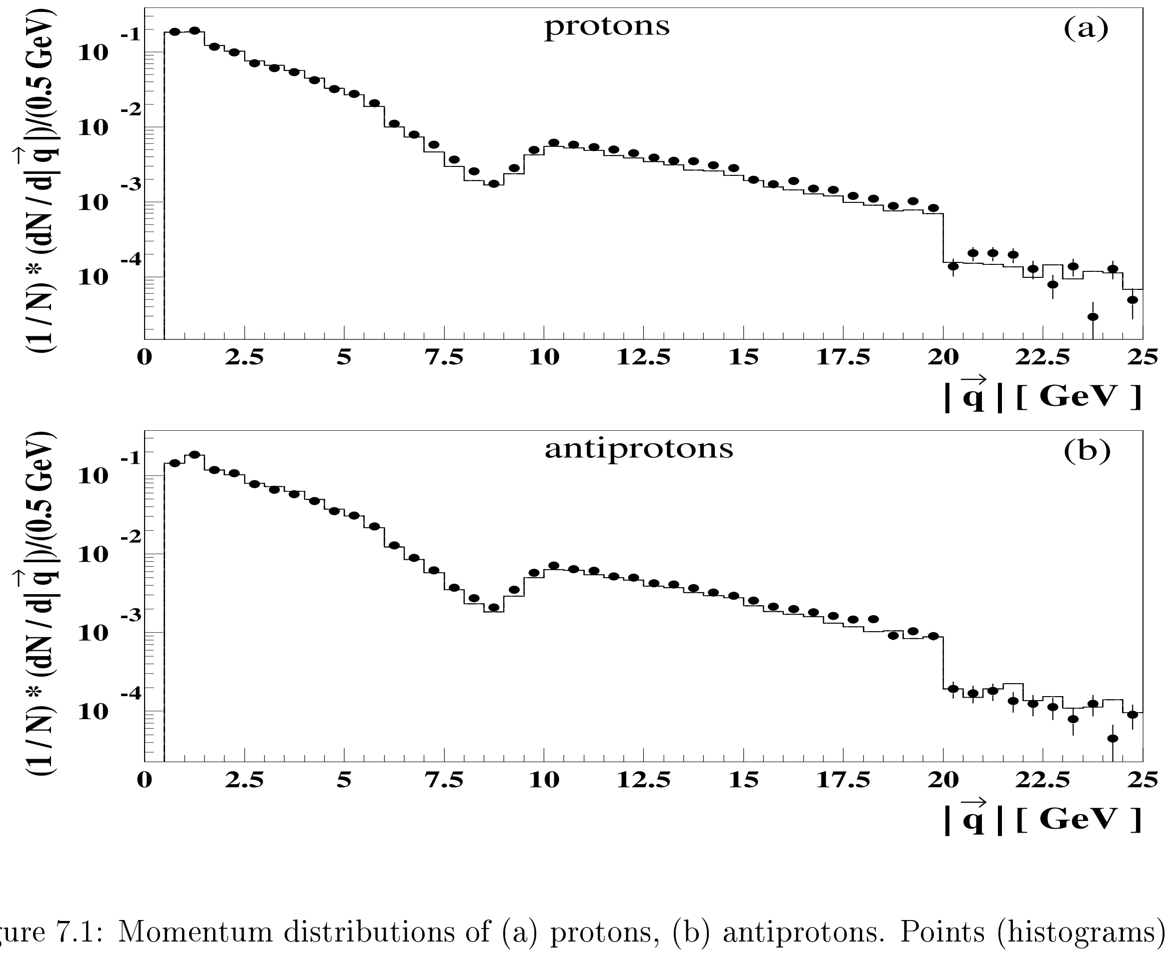

Figure 7.1: Momentum distributions of (a) protons, (b) antiprotons. Points (histograms) denote distributions for the data (Monte Carlo simulation).

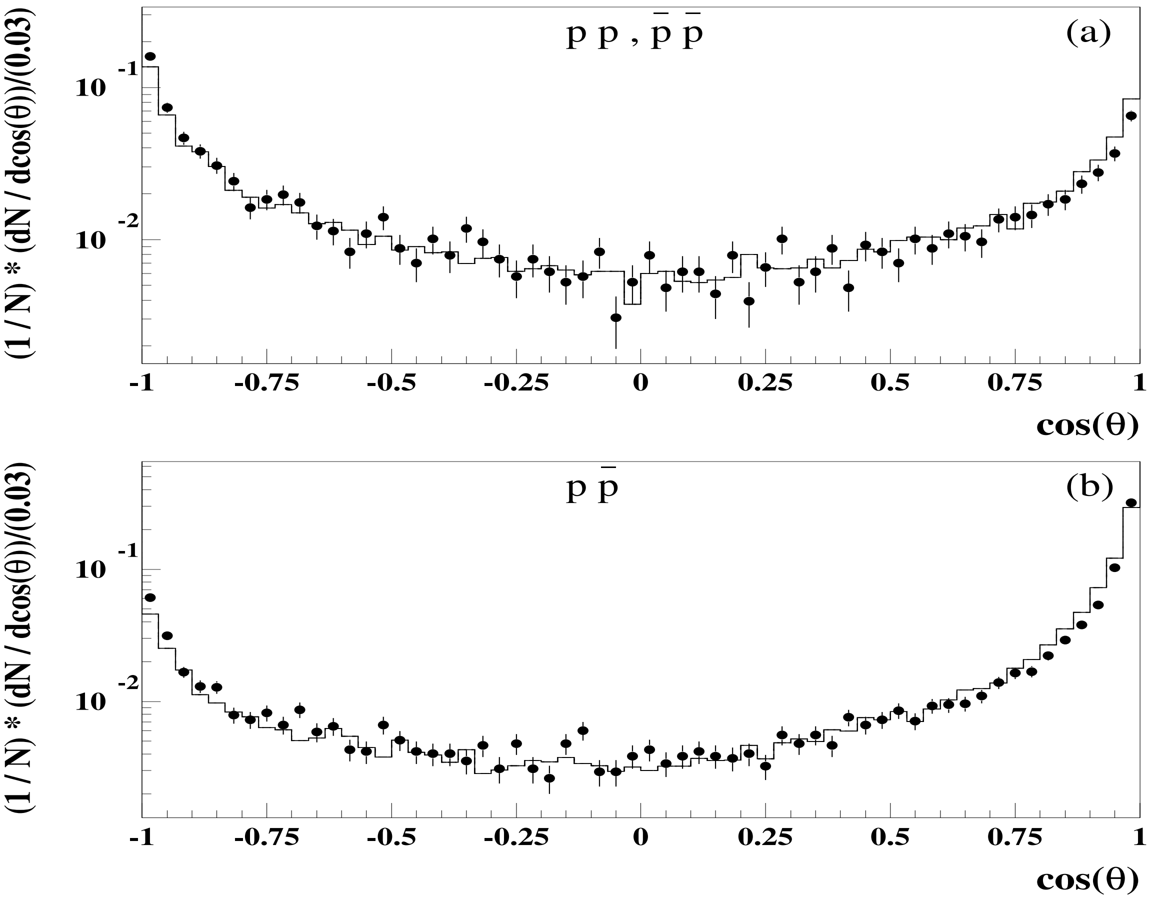

Figure 7.2: Distributions of the cosine of the angle (θ) between two particles' momentum vectors for (a) like-sign (pp, $\bar{p}\bar{p}$), (b) unlike-sign ($p\bar{p}$) proton pairs. Points denote distributions for the data, histograms stand for Monte Carlo simulation.

for the like- (pp, $\bar{p}\bar{p}$) and unlike-sign ($p\bar{p}$) pairs are compared to the MC simulation in Fig.7.2. Again, a good overall agreement between the data and MC may be noticed. Thus, the MC model reproduces fairly well the main features of the proton data sample.

In Fig.7.3 the Q distributions in data are compared to the respective ones in MC for pp, $\bar{p}\bar{p}$ and unlike-sign proton pairs. In the case of like-sign (pp, $\bar{p}\bar{p}$) distributions (Fig.7.3a,b) the data points are below the MC prediction in the region of low-Q values, while in the rest of the distribution they agree well. In the $p\bar{p}$ distribution (Fig.7.3c) MC underestimates the data for $|\vec{q}| < 1$ GeV. The total background, indicated by blue lines, is superimposed in pp and $\bar{p}\bar{p}$ distributions, while the contribution from secondary interactions is denoted by a red shaded histogram. It is clear that both the total background and its secondary interaction part affect more strongly the Q distribution for pp than $\bar{p}\bar{p}$ pairs. The total background contribution as well as its secondary interaction part for $\bar{p}\bar{p}$ pairs in the low-Q region correspond to 31% and 11% of the total sample, respectively. In the case of pp pairs the fractions of total background and secondary interactions amount to 49% and 36%, correspondingly.

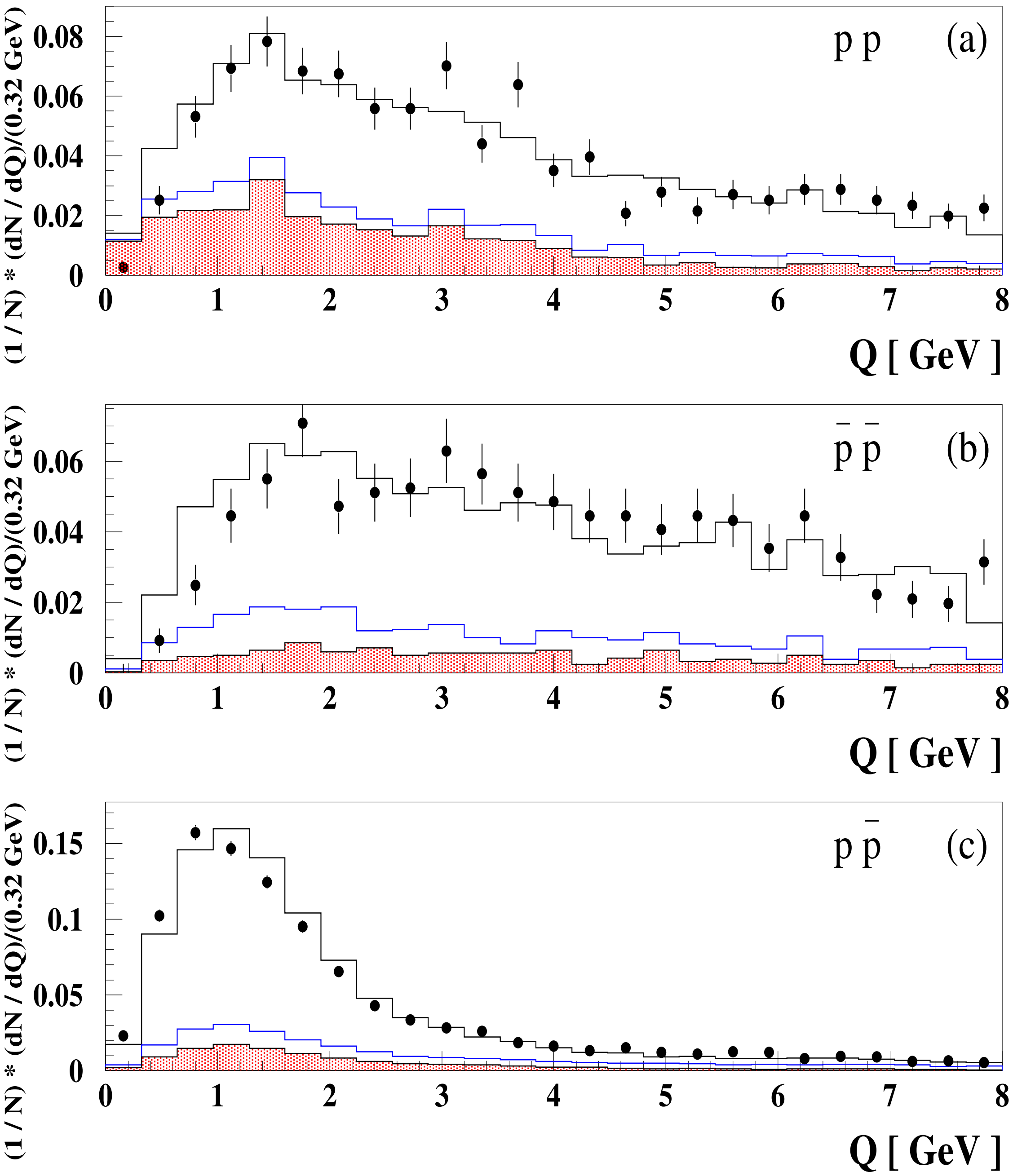

Figure 7.3: Distributions of the four-momenta difference Q in the data (points) and in MC (histogram) for (a) pp, (b) $\bar{p}\bar{p}$ pairs, (c) unlike-sign ($p\bar{p}$) proton pairs. Blue lines represent the total background due to misidentification and secondary interactions, red shaded histograms indicate the background contribution due to secondary interactions.

7.2 Construction of a mixed reference sample

An event-mixed reference sample was constructed using the following procedure:
1) momentum vectors of all proton and antiproton candidates were transformed to the reference frame defined by the thrust axis (cf Sect. 3.1);
2) each p ($\bar{p}$) momentum vector was stored in a buffer of momentum vectors;
3) for a given pair of antiprotons$-\bar{1},\bar{2}$ (protons$-1,2$) with respective momenta $\vec{q}_{\bar{1}}$, $\vec{q}_{\bar{2}}$ ($\vec{q}_1$, $\vec{q}_2$) the two momentum-vector pairs $\vec{q}_{\bar{1}}\vec{q}_{\bar{1},mix}$, $\vec{q}_{\bar{2}}\vec{q}_{\bar{2},mix}$ and ($\vec{q}_1\vec{q}_{1,mix}$, $\vec{q}_2\vec{q}_{2,mix}$) were derived using original momenta and momenta randomly drawn from the buffer;
4) the above procedure was repeated for every pair of antiprotons (protons).
Two variants of the mixing procedure were tested: with and without removing the already used momenta from the buffer. No significant change in the result was observed.

A comparison of the momentum distributions for original and mixed samples, for p and $\bar{p}$ separately, is shown in Fig.7.4. No distortions were found in the distributions resulting from the mixing. The cosine of the $\bar{p}\bar{p}$ (pp) opening angle θ distributions in the data and the mixed sample are presented in Fig.7.5. It should be emphasised that these distributions usually get distorted while mixing [53, 82], which is not covered by this study. Therefore, an event-mixed reference sample may be applied to obtain the correlation function.

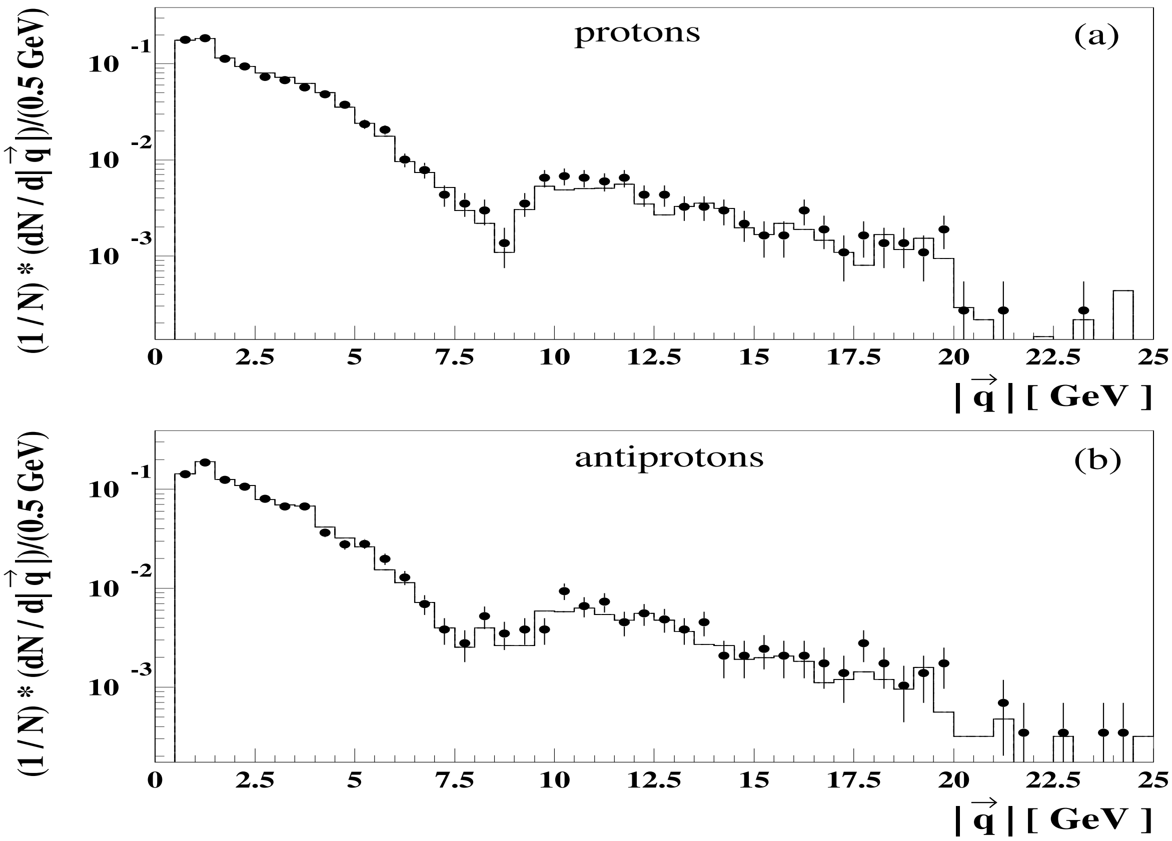

Figure 7.4: Momentum distributions of (a) protons, (b) antiprotons. Points denote distributions for the data, histograms represent mixed data samples, as described in the text.

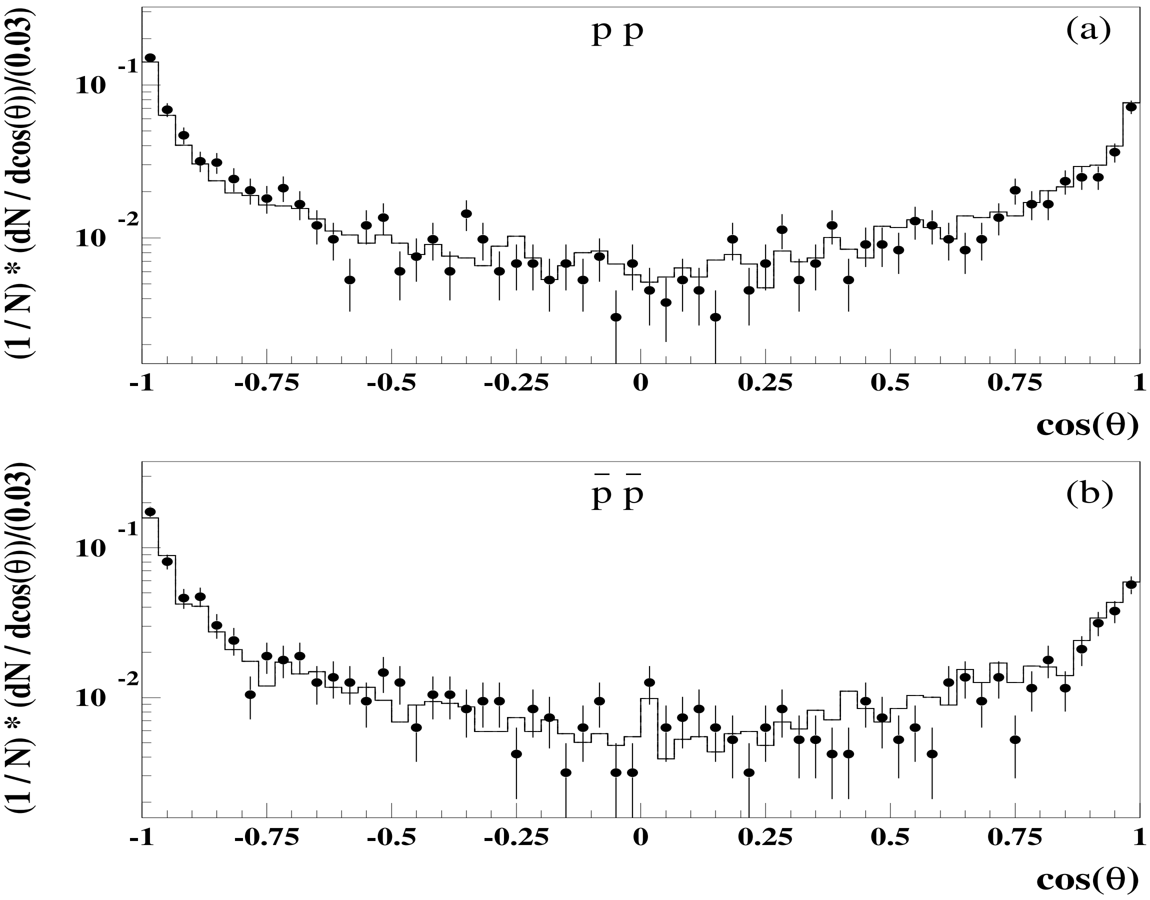

Figure 7.5: Distributions of the cosine of the angle (θ) between two particles' momentum vectors for (a) pp, (b) $\bar{p}\bar{p}$ pairs. Points denote distributions for the data, histograms represent mixed data samples, as described in the text.

A comparison of the Q distributions in the data and in the mixed sample was also performed (cf Fig.7.3). The four momenta difference distributions for the mixed samples (Fig.7.6) are very similar to the MC distributions in Fig.7.3a,b. Likewise, the Q distributions for $\bar{p}\bar{p}$ and pp obtained from the MC mixed-events are consistent with the corresponding MC distributions.

7.3 Determination of the correlation function

Correlation functions are determined using three different reference samples: the Monte Carlo, mixed-events and unlike pairs. They are evaluated primarily for antiproton pairs, for which the background is low and fairly flat (cf Sect. 5.3). The correlation function defined in formula (3.1) with the Monte Carlo distribution used as a reference sample assumes the form:

$$C_2^{MC}(Q) = \frac{\rho_2(Q)^{data}}{\rho_2(Q)^{MC}}, \tag{7.1}$$

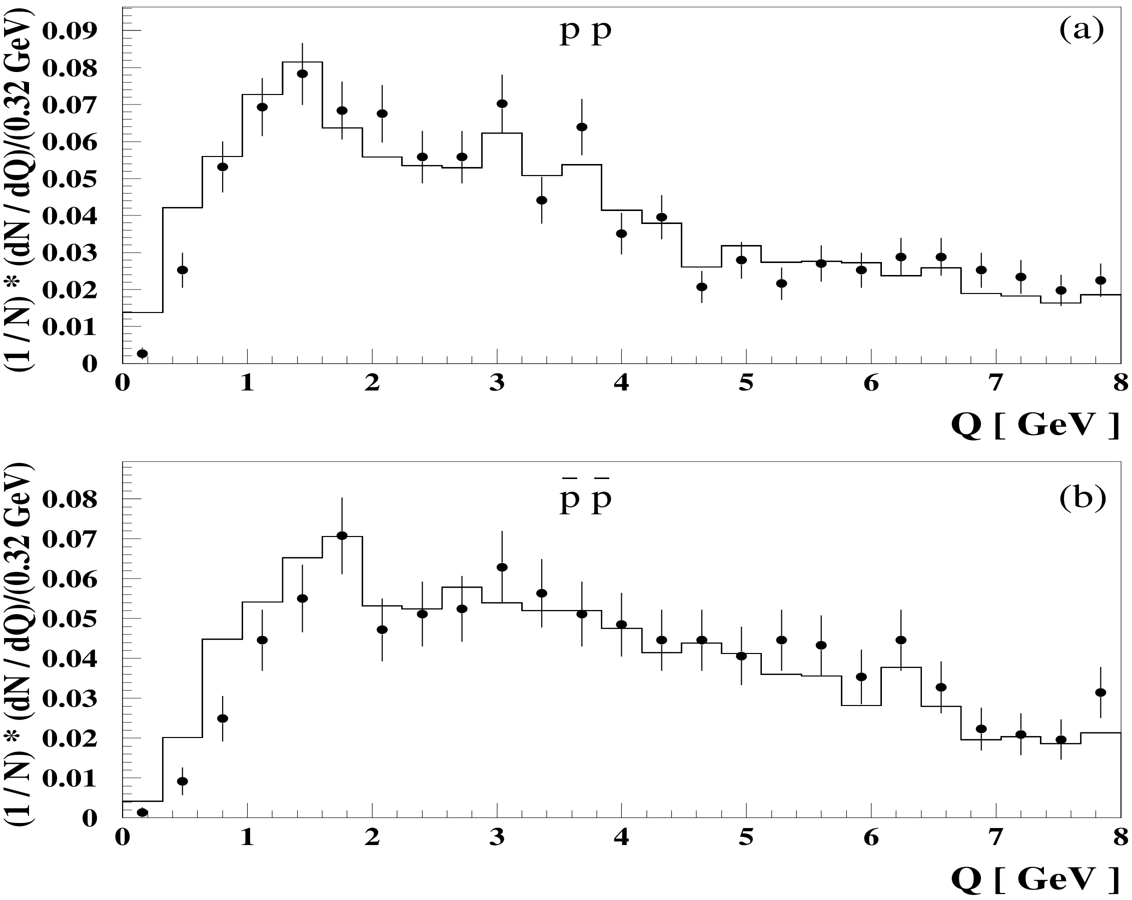

Figure 7.6: Distributions of particles' four-momenta difference (Q) for (a) pp, (b) $\bar{p}\bar{p}$ pairs. Points denote distributions for the data, histograms represent mixed data samples.

where $\rho_2(Q)^{data}$ stands for the Q distribution of $\bar{p}\bar{p}$ ($p\bar{p}$) pairs in data and $\rho_2(Q)^{MC}$ represents the same distribution in the JETSET Monte Carlo without the Fermi-Dirac effect. $\rho_2(Q)^{data}$ and $\rho_2(Q)^{MC}$ are both normalised to 1. The correlation function distributions for antiprotons and proton-antiproton pairs are shown in Fig.7.7. In the region of $Q < 2$ GeV a depletion in the $C_2^{MC}(Q)$ for antiproton pairs as well as an enhancement in the same distribution for $p\bar{p}$ pairs may be observed.

An alternative method of determining the correlation function relies on the event-mixed reference sample:

$$C_2^{mix}(Q) = \frac{\rho_2(Q)^{data}}{\rho_2(Q)^{data}_{mix}}, \tag{7.2}$$

where $\rho_2(Q)^{data}$ denotes the distribution of $\bar{p}\bar{p}$ pairs in the same event and $\rho_2(Q)^{data}_{mix}$ represents pairs of antiprotons from different events. In this method not only the Fermi-Dirac but also all other correlations may be removed from the reference sample. In order to correct for this effect the double ratio is usually applied:

$$R^{mix}(Q) = \frac{\rho_2(Q)^{data}}{\rho_2(Q)^{data}_{mix}} \Bigg/ \frac{\rho_2(Q)^{MC}}{\rho_2(Q)^{MC}_{mix}}. \tag{7.3}$$

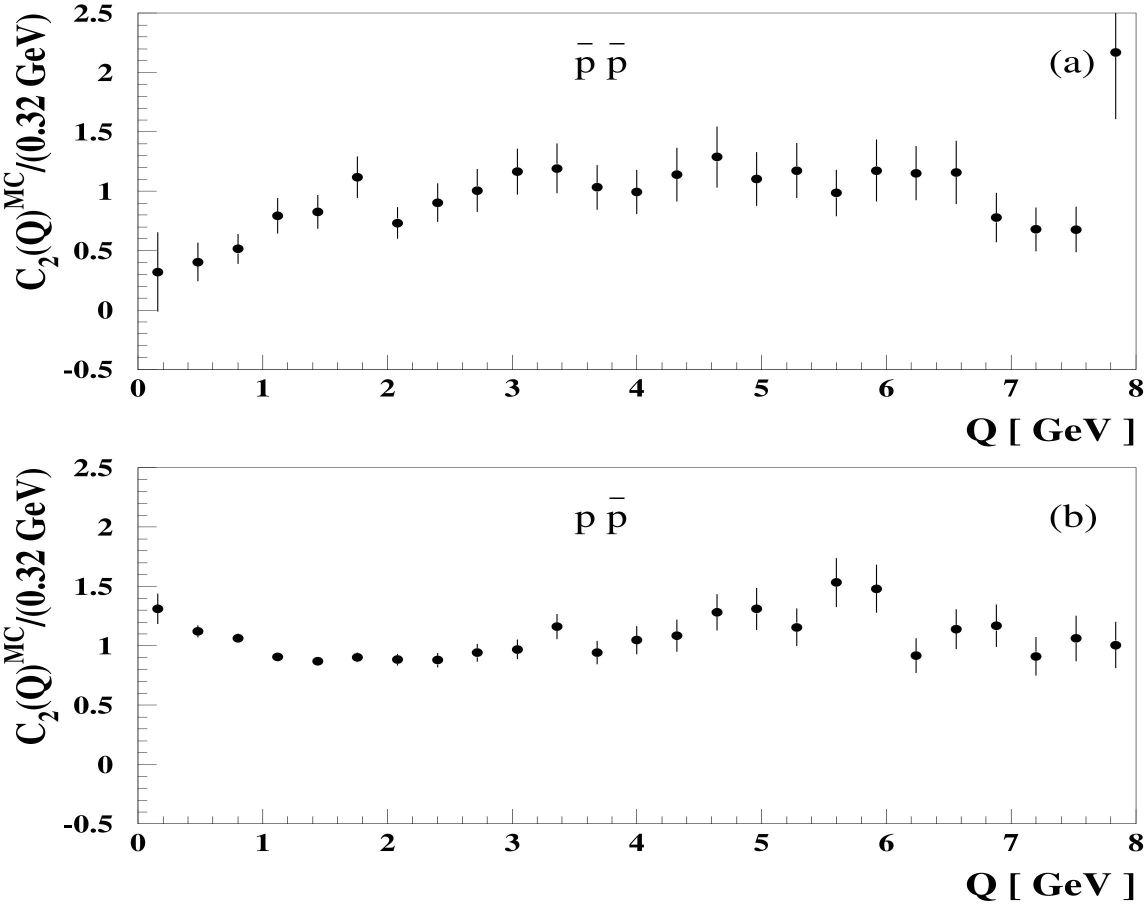

Figure 7.7: Distributions of the correlation function C_2^{MC} (as defined in formula 7.1) with the MC reference sample for (a) $\bar{p}\bar{p}$, (b) $p\bar{p}$ pairs.

As has been mentioned in Sect. 7.2, the Q distributions for pp, $\bar{p}\bar{p}$ obtained from the MC mixed-events are compatible with respective MC distributions. Therefore, the factor $(\rho_2(Q)^{MC}/\rho_2(Q)^{MC}_{mix})$ in formula (7.3) is nearly constant and close to 1, and thus it is unnecessary to resort to the double ratio (7.3) to determine the correlation function. In consequence, the double ratio technique was used only as a consistency check. The correlation function and double ratio distributions with event-mixing sample used as a reference are presented in Fig.7.8.

The correlation function, based on an event-mixed reference sample with background subtraction, was also examined. No change could be observed in contrast with the situation when the background was not subtracted.

The last approach uses the unlike reference sample, where the double ratio is analysed:

$$R^{unlike}(Q) = \frac{\rho_2(Q)_{data}}{\rho_2(Q)^{data}_{unlike}} \Bigg/ \frac{\rho_2(Q)_{MC}}{\rho_2(Q)^{MC}_{unlike}}, \tag{7.4}$$

where $\rho_2(Q)_{data}$, $\rho_2(Q)_{MC}$ denote respectively the Q distributions of antiproton pairs for data and MC sample, and $\rho_2(Q)^{data}_{unlike}$, $\rho_2(Q)^{MC}_{unlike}$ indicate the unlike Q distributions in

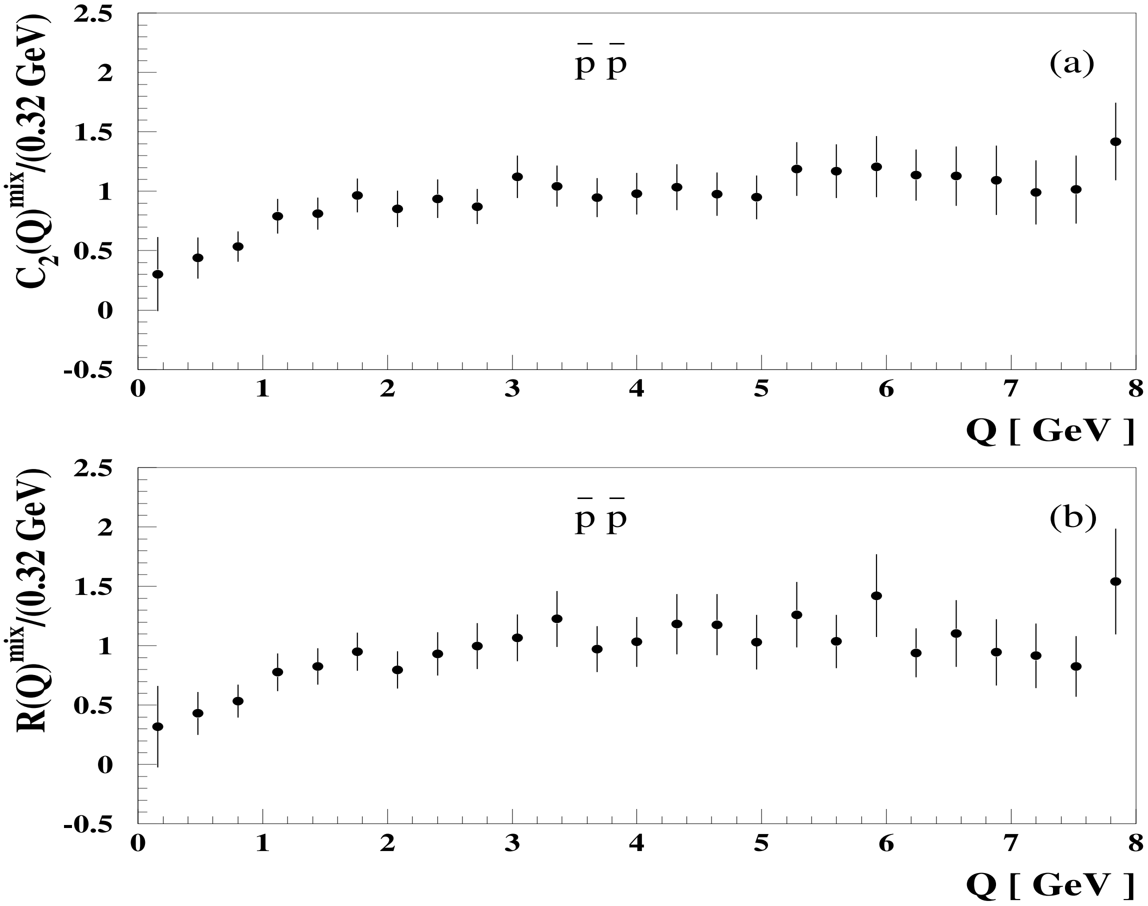

Figure 7.8: (a) Correlation function C_2^{mix} (as defined in formula 7.2) with the event-mixed reference sample for $\bar{p}\bar{p}$ pairs, (b) corresponding double ratio R^{mix} (cf formula (7.3)).

data and MC, correspondingly.

7.4 Determination of the correlation radius

The distributions of the correlation function for $\bar{p}\bar{p}$ pairs, defined by assuming the event-mixing, MC and unlike reference samples, were fitted using the parametrisation given in formula (2.21). The fits are presented in Fig.7.9. Two options, corresponding to the value of normalisation factor fixed at one and left as a free parameter, were examined. The fitted range of the Q variable amounted to $0 < Q < 8.0$ GeV. The results of fits to the correlation function for $\bar{p}\bar{p}$ pairs with MC (cf formula (7.1)) and event-mixed (cf formula (7.2)), together with the fit to the double ratio R^{unlike} (cf formula (7.4)) are collected in Table 7.2. The entries in brackets correspond to the fit variant where the normalisation factor in formula (2.21) remains free.

As may be seen in Table 7.2, all fits yield the normalisation factor N in formula (2.21) compatible with one. For that reason the fits to the correlation function with $N = 1$ were chosen as the final result. Since the analysis relying on the event-mixing reference sample

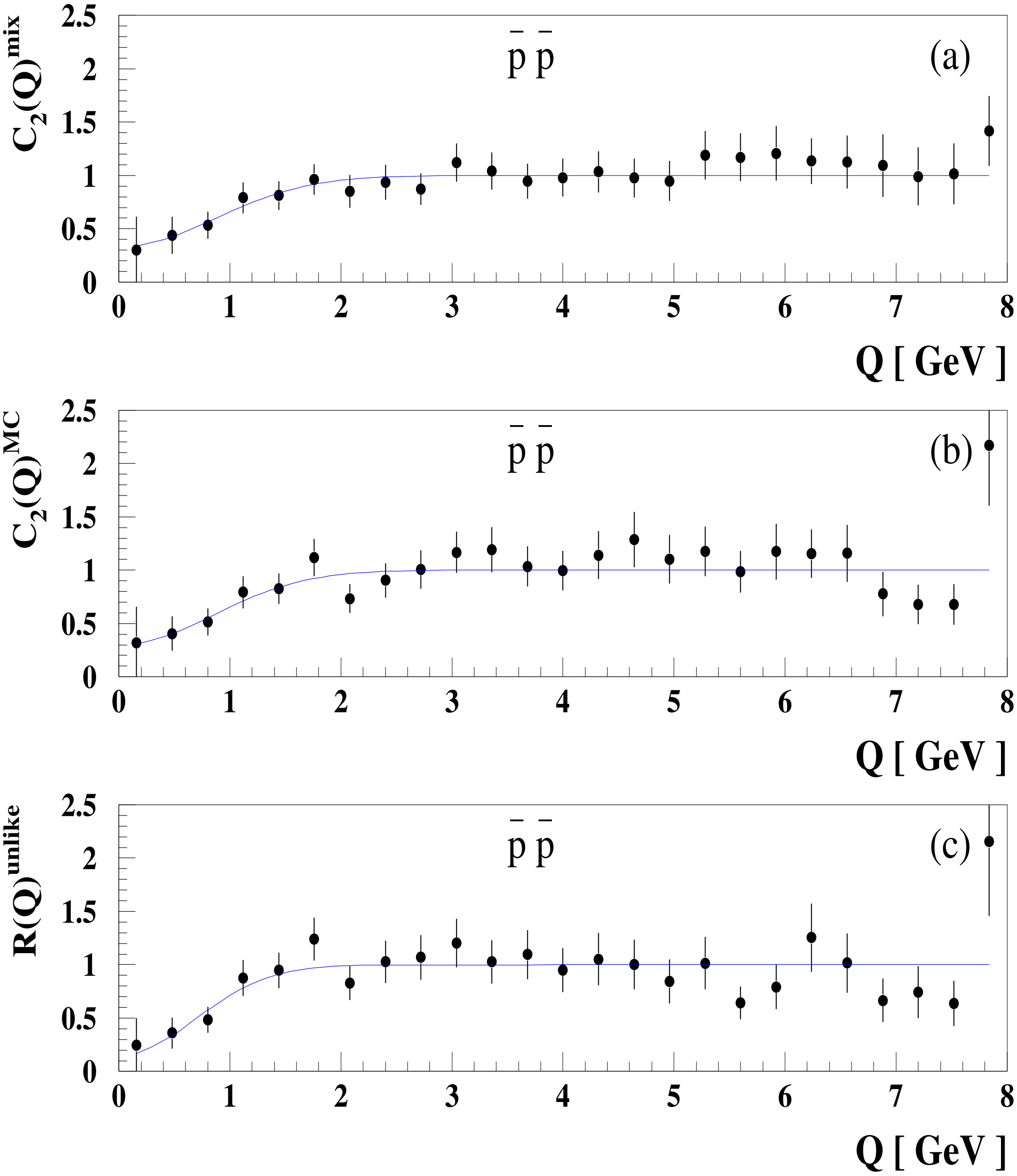

Figure 7.9: Fits to the correlation function distributions for $\bar{p}\bar{p}$ pairs using parametrisation described in the text: (a) event-mixed reference sample, (b) MC reference sample, (c) unlike reference sample (double ratio, as defined in (7.4) was fitted in this case).

Table 7.2: Results of fits to the correlation function $C_2(Q)$ for $\bar{p}\bar{p}$ pairs using parametrisation (2.21) where the normalisation factor is fixed at 1 (upper numbers) and remains free (numbers in brackets), in the case of the MC, event-mixed and unlike reference samples. Only statistical errors were included.

	Reference sample		
Parameters	MC	Event-mixed	Unlike
R [fm]	$0.17^{+0.04}_{-0.05}$ $\left[0.16^{+0.04}_{-0.05}\right]$	$0.16^{+0.04}_{-0.04}$ $\left[0.15^{+0.05}_{-0.04}\right]$	$0.20^{+0.04}_{-0.04}$ $\left[0.20^{+0.04}_{-0.04}\right]$
λ	$0.70^{+0.20}_{-0.17}$ $\left[0.70^{+0.21}_{-0.17}\right]$	$0.67^{+0.19}_{-0.17}$ $\left[0.65^{+0.19}_{-0.16}\right]$	$0.85^{+0.18}_{-0.16}$ $\left[0.85^{+0.20}_{-0.18}\right]$
N	1.0 (fixed) $[1.00 \pm 0.05]$	1.0 (fixed) $[1.03 \pm 0.05]$	1.0 (fixed) $[0.96 \pm 0.05]$
χ^2/ndf	24/23 [24/22]	18/23 [17/22]	25/23 [25/22]

is more precise than the MC or unlike reference sample ones, the final result is taken from the event-mixing analysis (with the normalisation factor fixed at 1):

$$R = 0.16 \pm 0.04(stat)\,\text{fm}, \tag{7.5}$$

$$\lambda = 0.67^{+0.19}_{-0.17}(stat). \tag{7.6}$$

Methods relying on the MC or unlike reference samples gave results compatible within errors with the event-mixing technique and were used only for a cross-check. The numbers listed above are consistent with the results of the fit to the double ratio distribution, as defined with respect to the event-mixed reference sample, where the values of fitted parameters are $N = 1.05 \pm 0.06$, $R = 0.13^{+0.05}_{-0.04}$ fm, $\lambda = 0.63^{+0.19}_{-0.15}$ in the case of parametrisation where the normalisation factor remained free, and $R = 0.16^{+0.05}_{-0.04}$ fm, $\lambda = 0.66^{+0.21}_{-0.17}$, when parametrisation with the normalisation factor fixed at 1 was used. In all the fits parameters R and λ are strongly correlated, where the correlation coefficient amounts to about 75%.

After subtracting the total background from the Q distribution of pp pairs, a fit to the correlation function with an event-mixed reference sample was also performed using parametrisation (2.21) with a free normalisation factor. The result of the fit is shown in Fig.7.10, which also lists the parameters of the fit. The obtained parameter values ($R = 0.19 \pm 0.07(stat)$, $\lambda = 0.88 \pm 0.21(stat)$) agree well with those for $\bar{p}\bar{p}$ pairs, nevertheless it suffers from a larger systematic error due to the background subtraction.

The following sources of systematic uncertainties in the R and λ determination were examined: the proton identification, double track resolution, background subtraction, different reference samples as well as the use of double ratio, parametrisation of the correlation function, fit range and bin width in Q. The maximum variation of R and λ with respect to the values from (7.5) and (7.6) in a given test was taken as an estimate of an individual systematic error contribution. The total systematic error was obtained by

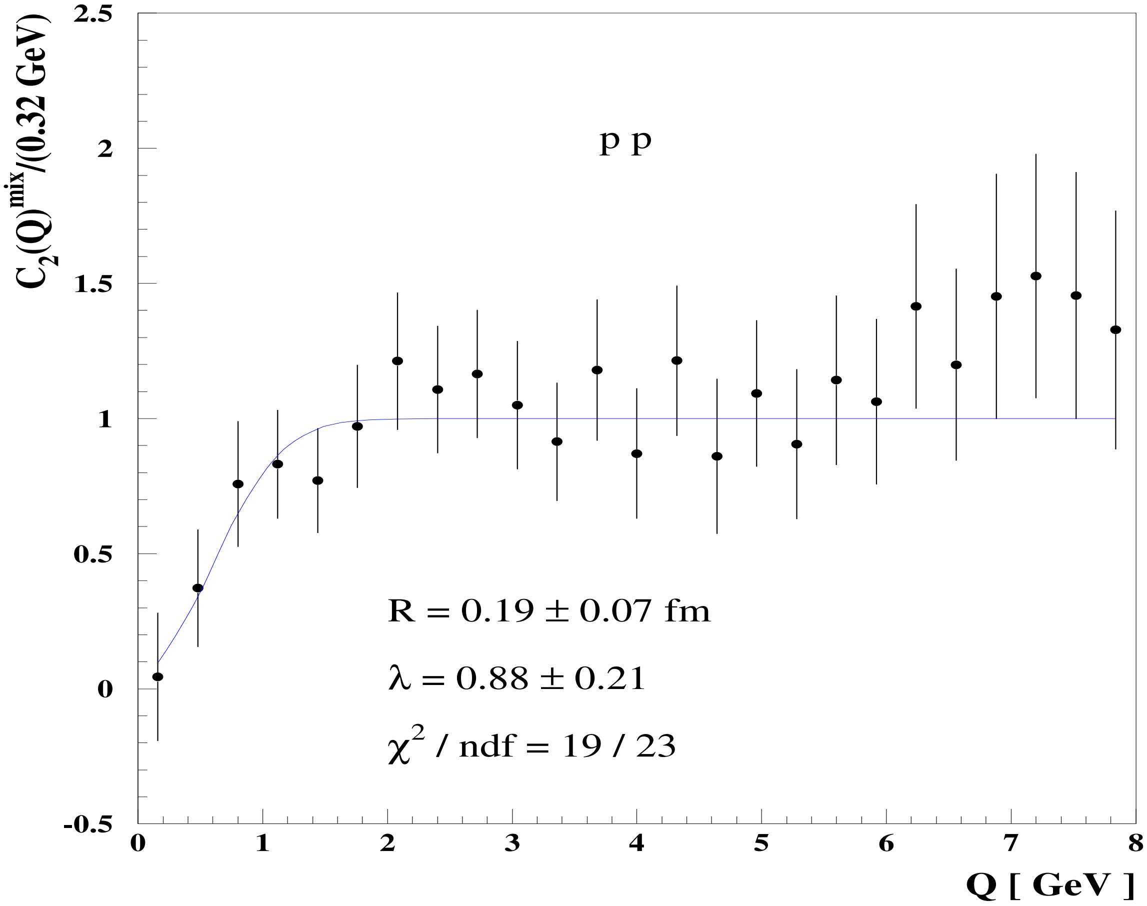

Figure 7.10: Distribution of the background subtracted correlation function C_2^{mix} for pp pairs together with fit results. Points (blue solid line) represent data (fit described in the text).

summing in quadrature individual contributions. Contributions to the systematic errors of R and λ are listed in Table 7.3. Systematic effects coming from the proton identification were evaluated by studying $\bar{p}\bar{p}$ samples with purities ranging from 60% (XPRNET$>$ 0.90) to 90% (XPRNET$>$ 0.97). The contribution due to the proton identification criteria appeared to be biggest among systematic uncertainties collected in Table 7.3. The obtained correlation functions together with fit results are shown in Fig.7.11. The effect of double track resolution was examined by selecting a sample with a two-track opening angle exceeding 2°. The effect of background subtraction was estimated by comparing results of the fit to the correlation function in the case of background subtraction and without it. The systematics due to different reference samples used, the double ratio and parametrisation of the correlation function were extracted from the results discussed at the beginning of this section. The systematics derived from the fit range was obtained by changing the upper limit of Q value from 6 to 9 GeV. The correction for Coulomb repulsion between particles in the pair was also examined by taking into account a Gamov penetration factor (cf Sect. 3.4 and formula 3.9). This had a negligible impact on the result, since it affects only the region of very low Q values.

Table 7.3: Contributions to the systematic error of R and λ. Numbers in parentheses refer to the range in which the parameters were varied.

systematic error source	ΔR	$\Delta\lambda$
identification; XPRNET $\in (0.90-0.97)$	0.017	0.141
double track resolution	0.008	0.023
background subtraction	0.004	0.052
different reference samples	0.013	0.068
double ratio	0.002	0.011
$C_2(Q)$ parametrisation	0.011	0.022
fit range; $Q_{MAX} \in (6.0-9.0)$ GeV	0.003	0.005
Q-bin size; $\Delta Q \in (0.25-0.35)$ GeV	0.011	0.063
total systematic error	0.028	0.180

Having considered the above, the final result for the radius of the antiproton source was calculated at

$$R = 0.16 \pm 0.04(stat) \pm 0.03(syst)\,\mathrm{fm}, \tag{7.7}$$

and the incoherence parameter

$$\lambda = 0.67^{+0.19}_{-0.17}(stat) \pm 0.18(syst). \tag{7.8}$$

7.5 Conclusions

We examined Fermi-Dirac correlations in variable Q for antiproton and proton pairs using three different reference distributions in the definition of the correlation function. Significant depletion in the correlation function is observed in the region of $Q < 2$ GeV, contrary to the enhancement seen for $p\bar{p}$ pairs. The depletion is interpreted as a result of the Pauli exclusion principle. The correlation function was fitted using parametrisation (2.21), which yielded a very small Gaussian source radius $R = 0.16 \pm 0.04(stat) \pm 0.03(syst)$ fm and a large incoherence parameter $\lambda = 0.67^{+0.19}_{-0.17}(stat) \pm 0.18(syst)$. The measurement based on the pp sample, which is not as clean as the $\bar{p}\bar{p}$ sample due to pollution from secondary interactions, yields a compatible result: $R = 0.19 \pm 0.07(stat) \pm 0.07(syst)$ fm, $\lambda = 0.88 \pm 0.20(stat) \pm 0.19(syst)$.

The present measurement agrees well with the ALEPH ($R = 0.11 \pm 0.01(stat) \pm 0.01(syst)$ fm, $\lambda = 0.49 \pm 0.04(stat) \pm 0.08(syst)$) [50] and OPAL ($R = 0.142 \pm 0.035(stat) \pm 0.047(syst)$ fm, $\lambda = 0.76 \pm 0.16(stat) \pm 0.29(syst)$) [52] results.

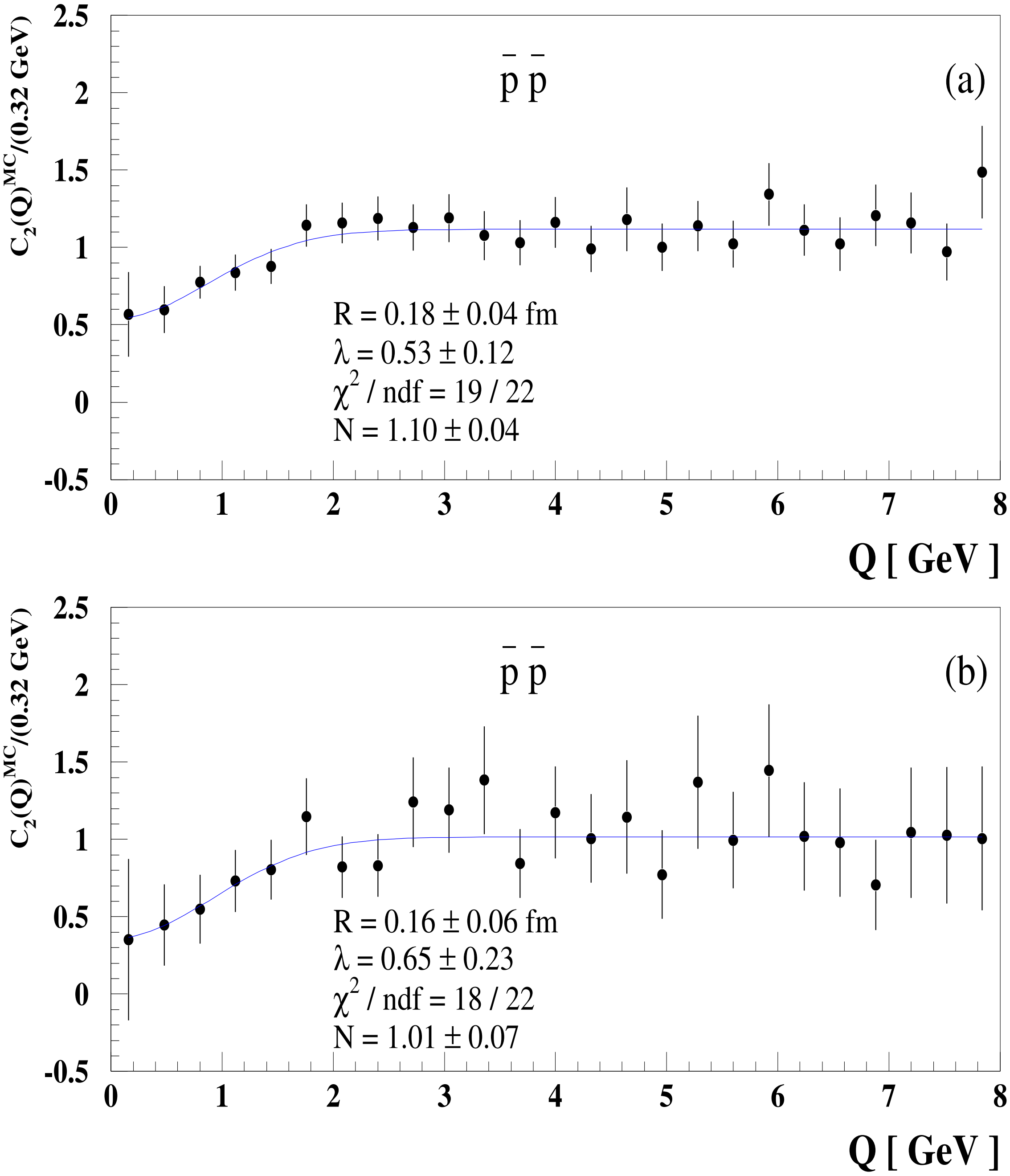

Figure 7.11: Correlation functions C_2^{MC} for $\bar{p}\bar{p}$ samples of different purities, together with fit results using parametrisation (2.21); (a) sample with lower purity of 60% (XPRNET> 0.90), (b) sample with enhanced purity of 90% (XPRNET> 0.97).

Chapter 8

Dependence of the correlation radius on hadron mass

Measurements of the emitter source radius performed by LEP experiments and discussed in chapter 4, including the results presented by the thesis (cf chapters 6 and 7), indicate that the correlation radius decreases with particle mass. This chapter is devoted to the discussion of theoretical attempts to describe this phenomenon. Among them are semi-classical models based on the Heisenberg relations or the virial theorem [83], and the quantum-mechanical model proposed by A. Białas and K. Zalewski [84]. The latter will be discussed in greater detail as the author of this thesis determined correlation functions predicted by the model so as to compare them with the data [85, 86].

8.1 Semi-classical model based on the Heisenberg relations

The BEC or FDC effect reaches its maximum (minimum) when the difference of four-momenta q_1 and q_2 of two identical hadrons approaches zero. In this case hadrons are nearly at rest in their centre-of-mass system, therefore their three-vector momenta difference Δq also goes to zero. Applying the Heisenberg uncertainty principle:

$$\Delta q \Delta R \geq \hbar c, \tag{8.1}$$

to relate Δq to the spatial separation of two particles, one obtains:

$$\Delta q \Delta R \approx \hbar c = 2\mu v R = m v R, \tag{8.2}$$

where μ is the reduced mass of two hadron system and $R \equiv \Delta R$ is the geometrical distance between them. The hadron mass and velocity are denoted by m and v, correspondingly. From formula (8.2) one obtains:

$$R = \frac{\hbar c}{m v} = \frac{\hbar c}{q}, \tag{8.3}$$

where $\hbar c \approx 0.197$ GeV fm.
On the other hand using the Heisenberg relation in terms of energy and time:

$$\Delta E \Delta t = \frac{q^2}{m} \Delta t \approx \hbar, \tag{8.4}$$

where ΔE is expressed in GeV, Δt in seconds, one obtains:

$$q^2 = \hbar m/\Delta t \quad \Rightarrow \quad q = \sqrt{\hbar m/\Delta t}. \tag{8.5}$$

By inserting the right hand side of the above implication into formula (8.3), the relation between R and m is arrived at:

$$R(m) = \frac{\hbar c/\sqrt{\hbar/\Delta t}}{\sqrt{m}} = \frac{c\sqrt{\hbar \Delta t}}{\sqrt{m}}. \tag{8.6}$$

Assuming that Δt is of the order of time scale for strong interactions, i.e. $\Delta t = 10^{-24}$ s, and independent of the hadron mass, one obtains the formula:

$$R(m) = A/\sqrt{m}, \tag{8.7}$$

where $A \approx 0.243$ fm GeV$^{1/2}$. The R dependence on mass from formula (8.7) is represented by the black solid line in Fig.8.1. Dashed black lines show the $R(m)$ dependence on Δt: the upper line corresponds to $\Delta t = 1.5 \cdot 10^{-24}$ s and the lower one to $\Delta t = 0.5 \cdot 10^{-24}$ s. The fit to the data points yielded $\Delta t = (1.2 \pm 0.3(stat.)) \cdot 10^{-24}$ s [9].

It is clear that this simple model gives satisfactory description of the observed hierarchy of the correlation radii with respect to the hadron mass $R_{\pi\pi} > R_{KK} > R_{pp} > R_{\Lambda\Lambda}$.

8.2 Model based on the virial theorem and QCD motivated potential

The authors of the model based on the Heisenberg relations [83] proposed another explanation of $\partial R/\partial m < 0$ on the basis of properties of the potential for interactions leading to hadronisation.

Semiclassically, the angular momentum of two particles is expressed as:

$$l = b_t|\vec{q_1} - \vec{q_2}| \approx \hbar c, \tag{8.8}$$

where $b_t = R/2$ for particles at distance R.

Considering the two particle system as a bound state in the interaction potential $V(R)$, the virial theorem may be employed so as to relate the average value of kinetic energies T to the average value of potential energies:

$$2\langle T\rangle = \langle \vec{b}_t \cdot \vec{\nabla}_t V(R)\rangle, \tag{8.9}$$

in which case only the transversal direction is taken into account. Substituting T in formula (8.9) by $T_t = q_t^2/m$, one obtains:

$$\langle \vec{R}_t \cdot \vec{\nabla}_t V(R)\rangle \approx \frac{\langle q_t^2\rangle}{m}. \tag{8.10}$$

The above formula illustrates that the dependence of $\langle q_t^2\rangle$ on radius R follows from the properties of the potential $V(R)$. Therefore, it may also be inferred that the average interaction volume depends on the $V(R)$ features (because of $\vec{\nabla} V(R)$):

$$R^2\langle \vec{R} \cdot \vec{\nabla} V(R)\rangle \approx \frac{(\hbar c)^2}{m}. \tag{8.11}$$

Since the physics of particle emission from the interaction point cannot be described by the perturbative QCD, the analytic form of the $V(R)$ dependence is practically unknown. Nevertheless, the Local Parton Hadron Duality (LPHD) [88, 89] hypothesis may be applied to guess $V(R)$. Namely, the LPHD states that the main features of the final state in multiparticle production are not significantly modified by unknown large distance effects. Therefore, the production of hadrons may be still considered as an interaction of partons (i.e. quarks, gluons), even if the hadronisation mechanism is unknown. The LPHD hypothesis is supported by the data from inclusive hadron production at LEP [90].

Thus, the general QCD potential for interacting two quarks:

$$V(R) = \kappa R - \frac{4}{3}\frac{\alpha_s \hbar c}{R} \tag{8.12}$$

was used to deduce features of the interaction volume. The values of potential parameters come from the calculations of meson decay constants ($\kappa = 0.70$ GeV/fm, $\alpha_s = 2\pi/9\ln[2.0 + 1.87\ \mathrm{GeV}^{-1}/R]$). It should be noted that since factor $R^2\langle\vec{R}\cdot\vec{\nabla}V(R)\rangle$ for the QCD potential introduced in (8.12) is nearly constant over the R range of 0.14 to 1.0 fm, the simple relationship

$$R(m) = B/\sqrt{m} \tag{8.13}$$

is approximately valid, where constant B is consistent with A in formula (8.7). The result of the above derivation is represented in Fig.8.1 by the red solid line.

Both the above-mentioned approaches providing an explanation of the $R(m)$ dependence suggest that hadrons are not emitted from a unique source, but from sources with radii strongly dependent on the mass. If that was the case, the small radius of the source emitting protons and Λ hyperons (0.10−0.16 fm) would imply enormously large energy density, estimated in [9] to be greater than 100 GeV/fm^3. An alternative model proposed by A. Białas and K. Zalewski (discussed below in Sect. 8.3) considers the universal source radius of all particle species and predicts an apparent source size as observed in interferometry measurements, which is smaller than the real size.

8.3 Model by A. Białas and K. Zalewski

The model proposed by A. Białas and K. Zalewski is based on the Björken-Gottfried condition which is dealt with at a greater length below. Then, the source function as well as the density matrix are evaluated using the above-mentioned relation. Finally, the single particle distribution of $q_\perp$ and two-particle correlation function are derived within this model.

8.3.1 Björken-Gottfried condition

The quantum-mechanical attempt to describe the phenomenon of dependence of the correlation radius on hadron mass [84–86] is based on the only classical assumption that the momentum-position correlation is included in the Björken-Gottfried condition [92–94]. This hypothesis assumes the existence of a linear relation between four-momentum (q_μ) and space-time position (x_μ) of the produced particle:

$$q_\mu = \lambda x_\mu, \tag{8.14}$$

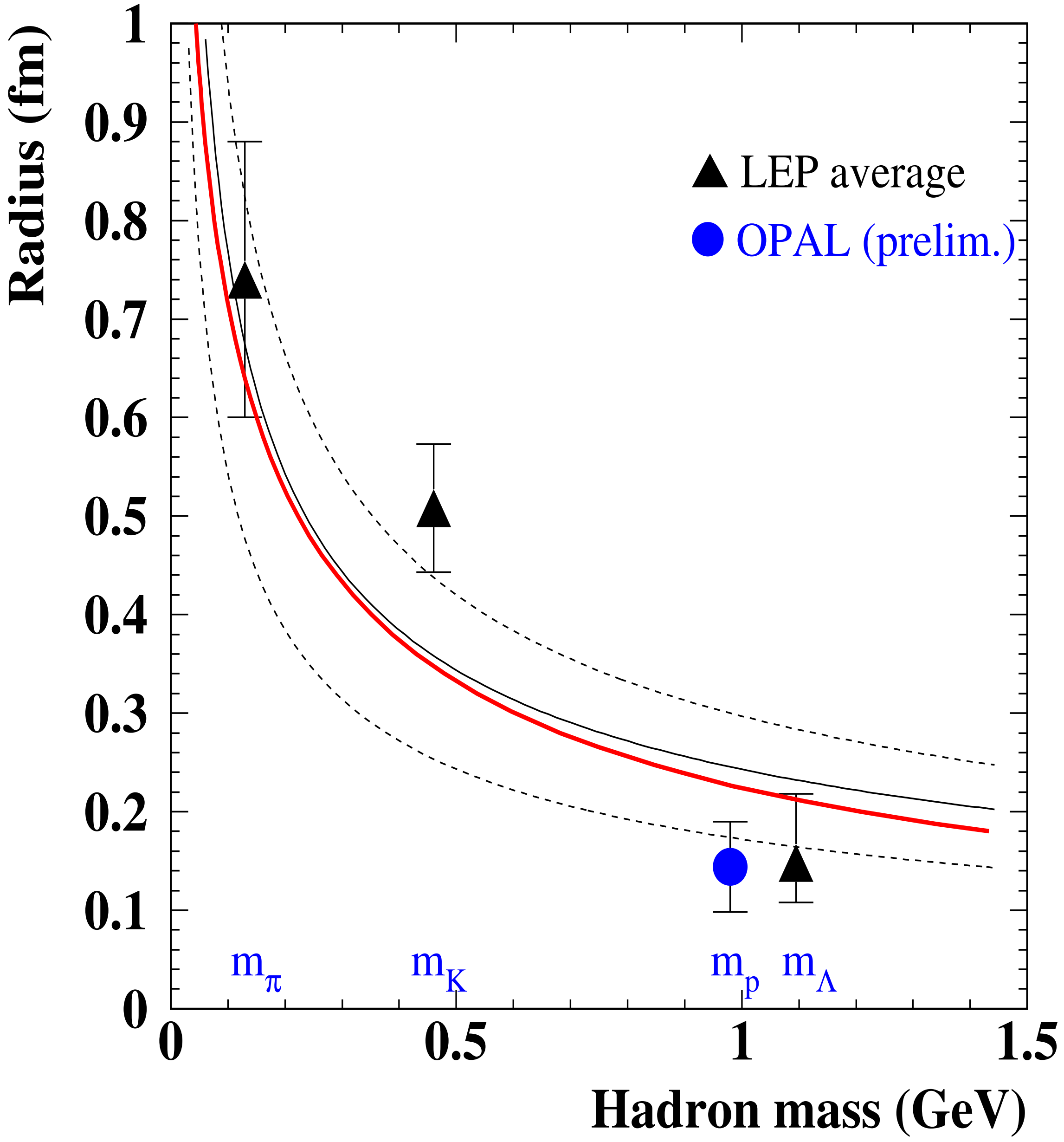

Figure 8.1: Radius of emitter source vs hadron mass (figure taken from [9]). Points denote averaged LEP results from the BEC and FDC analyses, whereas the superimposed curves represent theoretical predictions based on the virial theorem with the QCD potential (red solid line) as well as on the Heisenberg uncertainty relations with $\Delta t = 10^{-24}$ s (black solid line). Upper and lower black dashed curves indicate predictions for $\Delta t = 1.5 \cdot 10^{-24}$ s and $\Delta t = 0.5 \cdot 10^{-24}$ s, respectively. Error bars indicate statistical and systematic errors added in quadrature.

where parameter λ is the scalar with respect to the boost along z axis. The longitudinal proper time from the moment of collision up to the moment of particle creation is fixed and expressed as follows (for all particles):

$$\tau = \sqrt{x_0^2 - x_3^2}, \tag{8.15}$$

where $x_0 = t$ is the time component of the space-time position of the produced particle and $x_3 = z$ is the component longitudinal to the beam axis. The hyperbola (8.15) is illustrated in Fig.8.2.

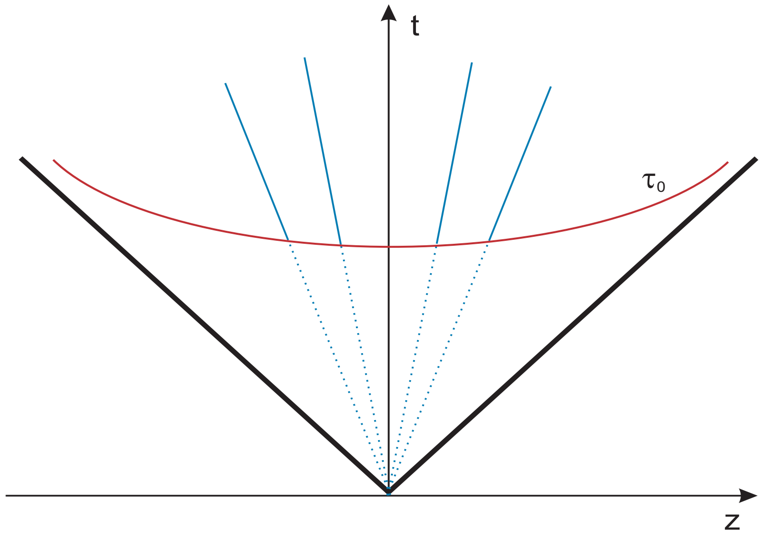

Figure 8.2: Space-time illustration of particle emission for a given fixed momentum. τ_0 denotes the longitudinal proper time, as given by (8.15), at a particular moment.

On the basis of the above equation and formula (8.14) it is possible to derive the expression for λ parameter:

$$\lambda = \frac{m_\perp}{\tau}, \tag{8.16}$$

where $m_\perp = E^2 - q_\parallel^2 = m^2 + q_\perp^2$ denotes the particle transverse mass. Therefore:

$$q_\mu = \frac{m_\perp}{\tau} x_\mu. \tag{8.17}$$

8.3.2 Source function

In the model by A. Białas and K. Zalewski the source function from formula (2.34) is postulated to be factorised in order to apply the Björken-Gottfried condition:

$$S(P, X) = F(\tau) S_\parallel S_\perp, \tag{8.18}$$

where $F(\tau)$ represents the distribution of longitudinal proper time, while $P = (q + q')/2$ and $X = (x + x')/2$ is the variable related to the position of the source in space-time, where x and x' indicate the position four-vectors (cf Sect. 2.5). Longitudinal and transversal components of the source function are given by the expressions:

$$S_\parallel = \exp\left[\frac{1}{2\delta_\parallel^2}\left(P_+ - \frac{M_\perp}{\tau} X_+\right)\left(P_- - \frac{M_\perp}{\tau} X_-\right)\right] \tag{8.19}$$

and

$$S_\perp = \exp\left[-\frac{X_\perp^2}{2r_\perp^2}\right]\exp\left[-\frac{P_\perp^2}{2\Delta^2}\right]\exp\left[-\frac{1}{2\delta_\perp^2}\left(\vec{P_\perp}-\frac{M_\perp}{\tau}X_-\right)^2\right], \tag{8.20}$$

where $X_\pm = t \pm z$, $P_\pm = P_0 \pm P_z$, the transverse mass of two particle system $M_\perp^2 = P_+P_-$, $\tau^2 = X_+X_-$ and $P_\perp$, $X_\perp$ denote transverse components of the four-momentum P and position four-vector X, respectively. The $S_{||}$ and $S_\perp$ components are assumed to be described by Gaussian distributions in order to simplify the evaluation of the Fourier transform in formula (2.34). The correlation between the momentum and the point of particle emission is introduced by the last factor in the transversal $S_\perp$ and longitudinal $S_{||}$ components of the source function, where Björken-Gottfried condition is applied. This condition accounts for the dependence of the correlation radius on the mass. The $\delta_\perp$ and $\delta_{||}$ parametrise the correlation lengths, the same determining the size of the particle emission region. The first exponent in $S_\perp$ indicates a standard cylindrically symmetric 'tube' in the configuration space, described by radius $r_\perp$, related to the source velocity by formula $v^2 = r_\perp^2/\tau^2$. The second factor in $S_\perp$ component introduces a natural cut-off on the transverse momenta of particles emitted from the tube, where Δ parameter represents the width of the Gaussian-like distribution of particle transverse momentum.

8.3.3 Density matrix

The density matrix in the momentum representation may be evaluated from the assumed source function (8.18):

$$\rho(q,q') = \int \tau d\tau F(\tau)\rho_{||}\rho_\perp, \tag{8.21}$$

where the transverse and longitudinal elements $\rho_\perp$ and $\rho_{||}$ take the forms:

$$\rho_\perp = \int d^2X_\perp S_\perp e^{-i\vec{X}_\perp\vec{Q}_\perp}; \qquad \rho_{||} = \int d\eta e^G. \tag{8.22}$$

Here, η denotes pseudorapidity: $\eta = \log(X_+/X_-)$ and

$$G = \frac{1}{2\delta_{||}^2}\left(P_+ - \frac{M_\perp}{\tau}X_+\right)\left(P_- - \frac{M_\perp}{\tau}X_-\right) + i(Q_0t - Q_{||}z), \tag{8.23}$$

where $Q_0^2 = Q_t^2 + Q_{||}^2$ with $Q_t^2 = (q_1 - q_2)^2$ and $Q_{||}^2 = (q_{||1} - q_{||2})^2$.

Ignoring the normalisation and phase factors, the integral of the orthogonal term in formula (8.22) may be evaluated exactly:

$$\begin{aligned}\rho_\perp(\vec{q}_\perp, \vec{q'}_\perp) &= 2\pi r_{eff}^2 \exp\left(-\frac{\vec{P}^2}{2}\left(\frac{1}{\omega^2}+\frac{1}{\Delta^2}\right) - \frac{\vec{Q}_\perp^2 r_{eff}^2}{2}\right)\\ &\times \exp\left[-i\frac{M_\perp\tau v^2}{\omega^2}\vec{P}_\perp\vec{Q}_\perp\right],\end{aligned} \tag{8.24}$$

where

$$\omega^2 = M_\perp^2 v^2 + \delta_\perp^2; \qquad v^2 = r_\perp^2/\tau^2; \qquad r_{eff}^2 = \frac{r_\perp^2\delta_\perp^2}{\omega^2}. \tag{8.25}$$

The integral of the longitudinal component assumes the form:

$$\rho_{||} = 2\exp\left(\frac{M_\perp^2}{\delta_{||}^2}\right)K_0(s), \tag{8.26}$$

where $K_0(s)$ represents the Bessel function of variable:

$$s = \left[\frac{M_\perp^4}{\delta_{||}^4} - \frac{\tau^2}{M_\perp^2}(\vec{P}_\perp\vec{Q}_\perp)^2 - 2i\frac{\tau M_\perp}{\delta_{||}^2}\vec{P}_\perp\vec{Q}_\perp + \frac{\tau^2}{4M_\perp^2}m_\perp^2 m_\perp'^2\sinh^2(y-y')\right]^{1/2}, \tag{8.27}$$

where $Q_\perp^2 = (q_{\perp 1} - q_{\perp 2})^2$, $m_\perp$ and $m'_\perp$ represent particle transverse masses, while y, y' denote its rapidities.

8.3.4 Single-particle distribution

One-particle distribution is derived on the basis of the diagonal elements of the density matrix:

$$\rho(q) \equiv \frac{dn}{dyd^2q_\perp} = 2\pi r_\perp^2\delta_\perp^2\exp\left[\frac{m_\perp^2}{\delta_{||}^2}\right]K_0\left(\frac{m_\perp^2}{\delta_{||}^2}\right)\exp\left[-\frac{q_\perp^2}{2\Delta^2}\right]I(q_\perp^2), \tag{8.28}$$

where

$$I(q_\perp^2) = \int \tau d\tau F(\tau)\xi^{-2}\exp\left[\frac{q_\perp^2}{2\xi^2}\right] \tag{8.29}$$

and

$$\xi^2 = m_\perp^2 v^2 + \delta_\perp^2. \tag{8.30}$$

It is clear that the integral (8.29) is responsible for the parametrisation of the transverse correlation length in formula (8.28).

8.3.5 Two-particle correlation function

The normalised two-particle correlation function assumes the form:

$$C_2(q_1,q_2) = \frac{|\rho(q_1,q_2)|^2}{\rho(q_1)\rho(q_2)} = \frac{|\rho_\perp(q_1,q_2)|^2|\rho_{||}(q_1,q_2)|^2}{\rho_\perp(q_1,q_1)\rho_\perp(q_2,q_2)\rho_{||}(q_1,q_1)\rho_{||}(q_2,q_2)}. \tag{8.31}$$

Here, only the Bose-Einstein or Fermi-Dirac correlations are considered, whereas all other correlations are neglected. The dependence of the correlation radius on the hadron rest mass is included in formula (8.31) by the relation $m_\perp^2 = q_\perp^2 + m^2$.

An important consequence of the model described above is the fact that the observed correlation radius R_{obs} is the apparent radius which is smaller than the real particle emission radius R_{real}:

$$\frac{1}{R_{obs}^2} \approx \frac{1}{R_{real}^2} + \frac{M_\perp^2}{\tau^2\delta_\perp^2} \qquad \Rightarrow \qquad R_{obs} < R_{real}. \tag{8.32}$$

Chapter 9

Determination of correlation functions and the correlation radius dependence on hadron mass in the model by A. Białas and K. Zalewski

This chapter describes the determination of correlation functions within the model by A. Białas and K. Zalewski presented in Sect. 8.3. Calculations were performed by the author of this thesis, based on the algorithm originally written by A. Białas. This algorithm was subsequently developed and extended by the author by applying numerical integrals and introducing other improvements. On the basis of the resulting correlation functions, the correlation radii for pions, kaons, protons and Λ hyperons were estimated and compared to experimental measurements.

These results were published in papers [85, 86]. Below, we present the results for the final improved version of the model as described in [86].

9.1 Estimation of free parameters of the model

Within the model proposed by A. Białas and K. Zalewski, the two essential parameters $\delta_{||}$ and $\delta_{\perp}$ determine the momentum-position correlation lengths resulting from the Björken-Gottfried condition. The other unknown parameters include: $\Delta-$width of the Gaussian-like distribution of particle transverse momentum, $v-$transverse component of the source velocity and τ_0-proper time at which particles are produced. The above-mentioned parameters determine the shape of the $q_{\perp}$ distribution given by formula (8.28). In principle, they may be derived from the data, however some of them (in particular v) are negligibly constrained. Therefore, in the final version of the model calculi the following strategy was adopted: the distribution of longitudinal proper time $F(\tau)$ was substituted by $\delta(\tau-\tau_0)$ on the assumption that the time range of particle production is very narrow $\sim 10^{-24}$ s or, correspondingly, $\tau_0 \approx 0.9$ fm. Moreover, we constrained our analysis to the case when $\delta_{||} = \delta_{\perp} \equiv \delta$. This decision was supported by the fact that the value of $\delta_{||}$ coincides, within the wide allowed range, with the relation $\delta_{||} \approx \delta_{\perp}$, fulfilled for the quasi-isotropic case. The values of δ and Δ parameters were established from the fit to the transverse momentum distribution for a range of $v \in (0.2-1.0)$. The fit to the distribution of $q_{\perp}^2$ for charged pions was performed using parametrisation (8.28). The fitted $q_\perp^2$ region was considered up to the value of 2.0 GeV^2, which contained 99% of the data. The region of small values of $q_\perp^2$ ($q_\perp^2 < 0.02$ GeV^2) was excluded from fits. This was motivated by the presence of uncertainties due to the contribution of low momentum pions from D^* decays and the possible influence of imperfect approximation of the primary quark direction by the measured thrust axis. The example fit, presented in Fig.9.1, performed on the assumption that $v = 0.286$, $\delta_\perp = 0.303$, $\delta_\parallel = 0.172$, gave the value of $\Delta = 0.421 \pm 0.018$.

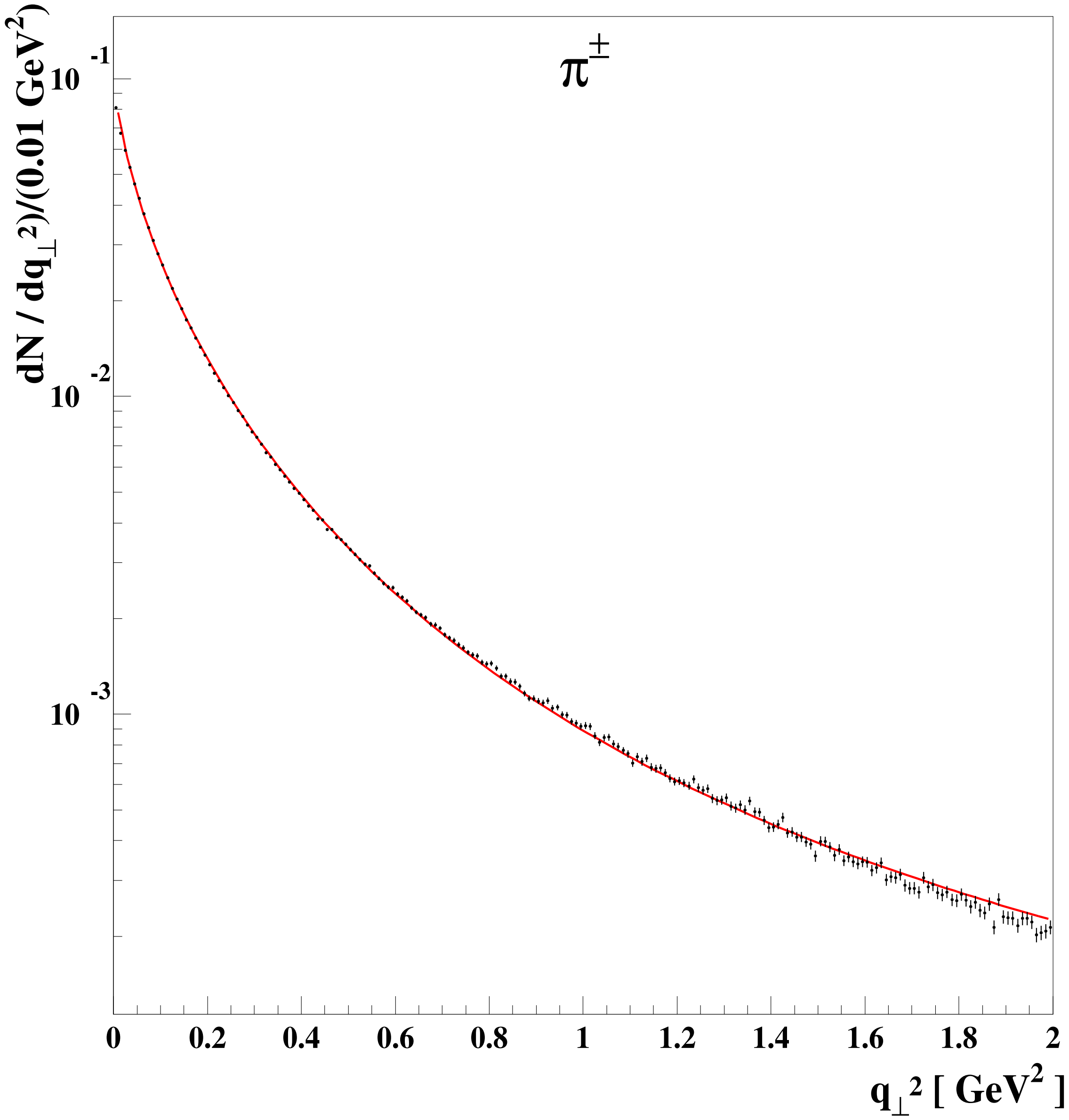

Figure 9.1: Fit to the square of the transverse four-momentum $q_\perp^2$ distribution for pions employing formula (8.28), with values of all relevant parameters as given in the text.

9.2 Determination of the two-particle correlation function

For a given set of parameters $\tau_0, v, \delta, \Delta$, the correlation function for each particle species may be calculated according to formula (8.31). Derivations were performed at discrete equidistant points in $Q_\perp^2$, $Q_\parallel^2$. This procedure was repeated for several values of v. The value of parameter v resulting in $R_\parallel/R_\perp = 1.4$ for pions was used in subsequent calculations, which was motivated by published experimental results. Phase-space integrals were derived numerically, while integrals of integrable formulae were performed analytically. Values of the parameters used in final derivations are collected in Table 9.1.

Table 9.1: Parameters of the model by A. Białas and K. Zalewski employed in the determination of the two-particle correlation function.

v	Δ [GeV]	δ [GeV]
0.94	0.421 ± 0.018	$0.233^{+0.034}_{-0.020}$

Similar calculations were also performed for kaons, protons and Λ hyperons. The available data samples for the above-mentioned particles are much smaller with respect to those for pions. That is why their $q_\perp^2$ distributions are not discriminating enough to estimate the model parameters with proper reliability. For that reason, the same parameters as those used for pions were adopted here (cf Table 9.1). It was proven that these parameters reproduce well the transverse momentum distributions for kaons, protons and Λ hyperons.

The example outcome, i.e. the correlation function for pion pairs, is shown in Fig.9.2. The resulting correlation functions display non-Gaussian behaviour. It should be pointed out that such a shape is often observed in the data [57–60, 74]. Nevertheless, for the reasons of simplicity, the Gaussian parametrisation is normally applied. The most important sensitivity to the R determination comes from the measured points with $Q \geq 100$ MeV. Additionally, the region of $Q < 100$ MeV in the data suffers from lower resolution as well as pollution from backgrounds ($\gamma \to e^+e^-$ conversion, split tracks etc.) and resonances, and is often omitted in data analyses. Therefore, to estimate R from the correlation function, the region of $Q < 100$ MeV was excluded and the correlation radius was determined using the Gaussian parametrisation.

Statistical errors shown in Fig.9.2 were estimated by employing correlations between free parameters. The above-mentioned correlations were taken into account by Gaussian sampling the area of three standard deviations correlation ellipse for every pair of parameters. The presence of such correlations makes unjustified the use of the one-dimensional statistical errors, as given by the MINUIT software package. Repeating calculations for extreme parameter values, which provided acceptable description of the $q_\perp^2$ distribution, enabled us to determine systematic effects of the fit. Strong points of the above-mentioned procedures lied in the fact that the value of the correlation function for each particle could be elaborated with both statistical and systematic errors, which were added linearly. Results of the calculation for charged pions are shown in Fig.9.2a,b for perpendicular and parallel components, correspondingly.

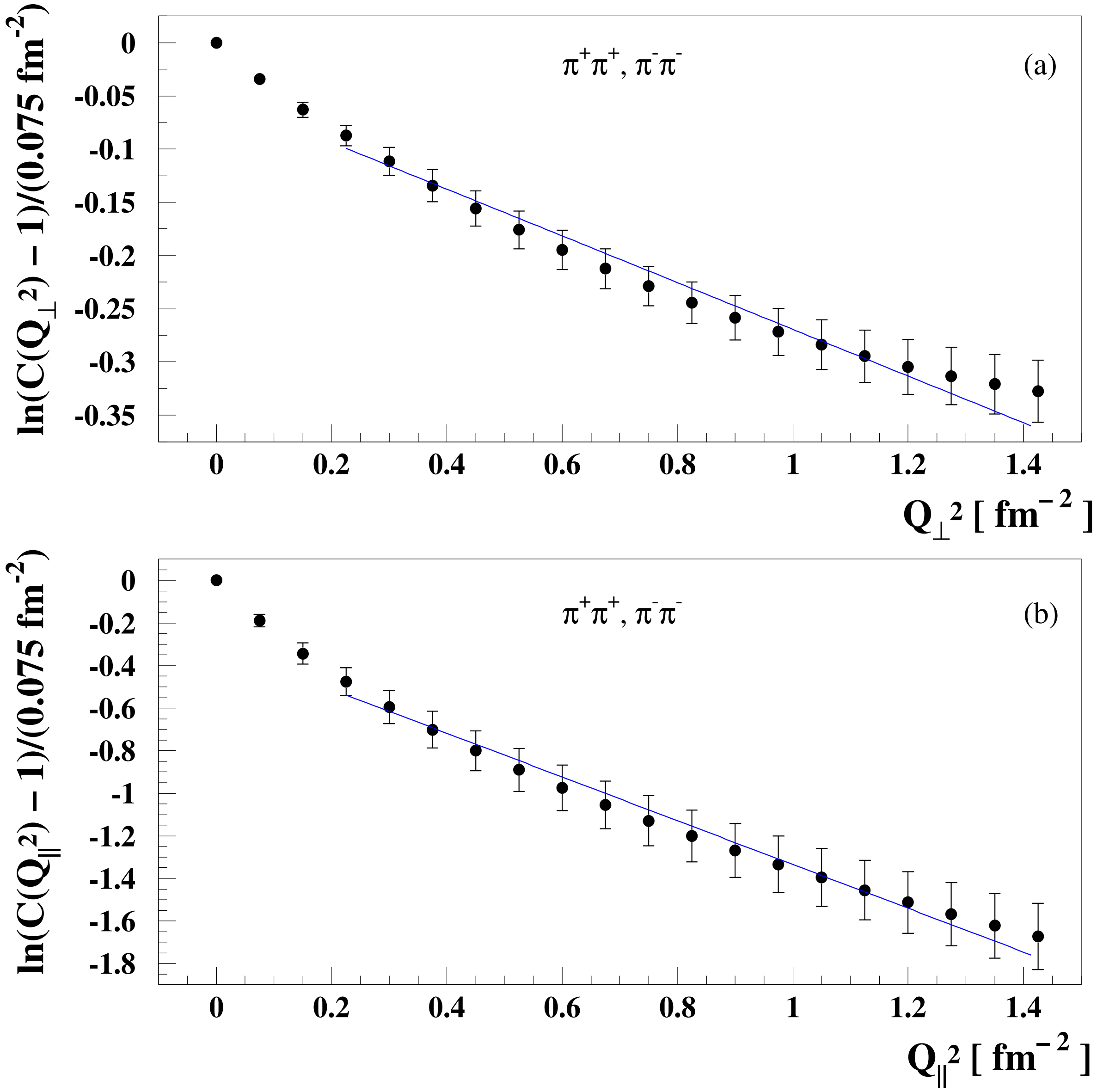

Figure 9.2: Two-particle correlation function of $C_2(Q_\perp^2)$ (a) and $C_2(Q_\parallel^2)$ (b) for charged pion pairs. Points denote data, blue lines represent fits to the correlation functions, as described in the text.

9.3 Determination of correlation radii for π, K, p and Λ

On the basis of the two-particle correlation function, determined above, the transversal ($R_\perp$) and longitudinal ($R_\parallel$) radii were calculated within the model by A. Białas and K. Zalewski. This evaluation was performed for masses of pion, kaon, proton and Λ hyperon, and compared to measurements conducted by four LEP experiments [47–55, 57–60, 74, 79, 80] (cf chapter 4) in Fig.9.3. Correlation radii for pions and protons determined in the thesis are also included in the figure. All measurements, i.e. those performed on the basis of studies on the correlation function in one, two and three dimensions were compared to the model expectations. For three-dimensional results obtained in the LCMS frame (see Sect. 3.2), $R_\perp = \sqrt{(R^2_{t,out} + R^2_{t,side})/2}$, $R_{||} = R_{long}$, while R, shown together with $R_\perp$ and $R_{||}$, represents the effective radius being the average over longitudinal and transverse directions. Results of one-dimensional analyses for pions are not taken into account, although they agree fairly well with the $R_\perp$ measurements from two- and three-dimensional studies. Shaded bands interconnecting the derived values of the correlation radius stand for one standard deviation error of the calculated value.

It is clear that the model describes remarkably well the dependence of the correlation radius on hadron mass, including inequality $R_{||} > R_\perp$. In particular, the difference $R_{||} - R_\perp$ decreases for higher masses.

The value of parameter $v = 0.94$, used in the calculations, was determined from the constraint $R_{||}/R_\perp = 1.4$ for pions, in order to describe properly the measured $R_{||}/R_\perp$ ratio. Although v treated as a free parameter leads to the higher value of the ratio $R_{||}/R_\perp$ [85], the difference $R_{||} - R_\perp$ still goes to zero with decreasing mass.

9.4 Conclusions

The observed correlation between identical hadrons produced in e^+e^- annihilation seems to be a consequence of the relation between the momentum and the production point of an emitted particle, suggested by the Björken-Gottfried hypothesis. The above-mentioned condition included in the model by A. Białas and K. Zalewski explains measured anisotropy of the two-pion correlation function and reproduces correctly the mass dependence of the correlation radius. An essential consequence of the model is the universality of the source radius, i.e. the radius of emitter volume is independent of the hadron mass. Moreover, the correlation radius determined from the Bose-Einstein and Fermi-Dirac correlation analyses is only an apparent radius, smaller than the real one.

Further studies are required to arrive at more quantitative conclusions. A key issue in this respect is to achieve better precision of the correlation radius measurements. In particular, the determination of $R_{||}$ and $R_\perp$ is missing for kaons, protons and Λ hyperons. Secondly, the model predictions were obtained with several simplifying assumpions in order to reduce the number of free parameters. With data samples of higher statistics some of those assumptions could be eliminated. A more numerous pion sample would probably allow for the separation of the determination of $\delta_{||}$ and $\delta_\perp$ as well as to make possible to perform precise determination of the v parameter. It will be difficult to determine directly the τ_0 parameter, but the predictions of the model assuming several τ distributions $F(\tau)$ could possibly be employed.

The mass dependence of the effective HBT correlation radii derived from the model and presented in Fig.9.3 was elaborated on the condition that parameters of the model not depend on particle masses. Nevertheless, for v, δ and Δ the above assumption may be fundamentally verified as soon as the data of higher statistics are available.

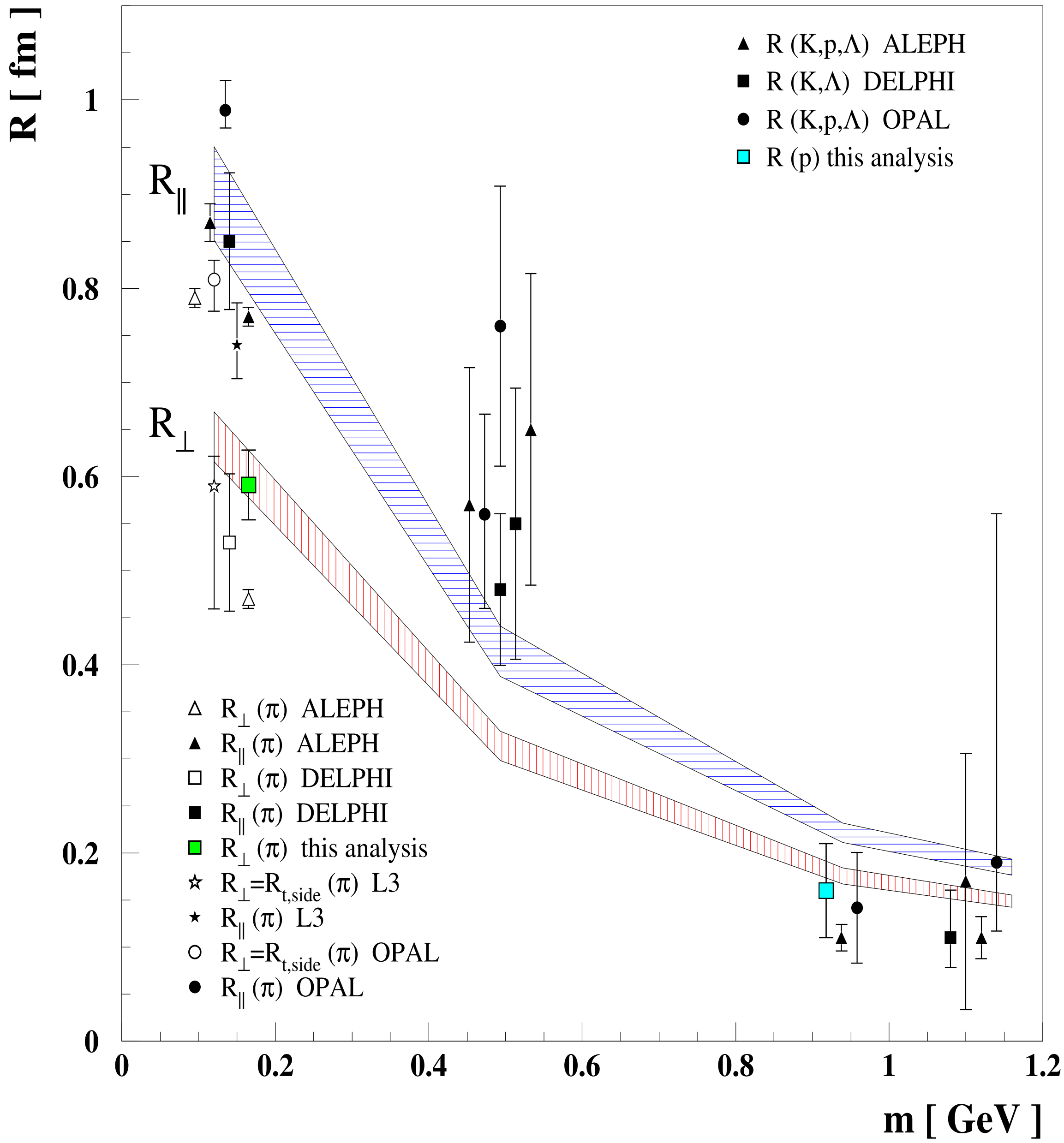

Figure 9.3: Transverse $R_{\perp}$ and longitudinal $R_{\parallel}$ components of the correlation radius derived from the model (shaded bands) for π, K, p, Λ. Data points at $m = m_{\pi}$ indicate results of 2- and 3-dimensional analyses for LEP data [57–60, 74], where the bars for ALEPH points denote statistical errors only. $R_{t,side}$ was assumed as the representative geometrical transverse dimension of the pion source in the case of 3-dimensional results. Points at higher masses account for 1-dimensional source radius R [47–55, 79, 80].

Chapter 10

Summary

The present thesis has undertaken the studies on the Bose-Einstein and Fermi-Dirac correlations in a hadronic Z^0 sample recorded in the DELPHI experiment at LEP. In the analysis of Bose-Einstein correlations for pions a new methodology (unique at LEP) was employed, where the correlation function for like-sign pions was analysed in the differences of azimuthal angles, rapidities and transverse momenta. The Bose-Einstein interference enhancement was identified in the two-particle correlation function of the azimuthal angle difference, providing the estimate of the spatial transverse radius of the pion source $R_\perp = 0.591 \pm 0.015(stat) \pm 0.034(syst)$ fm. The above-mentioned result agrees with other LEP measurements conducted by other methods. It supports LEP's evidence for different values of the source radius in longitudinal and transverse directions.

The correlation radius for protons has been determined employing the correlation function of the four-momentum difference. The correlation function for antiproton-antiproton and proton-proton pairs displays a strong depletion in the low-Q region. Such decrease is observed in the correlation functions determined by three different reference distributions: Monte Carlo, unlike and event-mixed samples. The source radius determined for an event-mixed reference sample amounts to $R = 0.16 \pm 0.04(stat) \pm 0.03(syst)$ fm, while the incoherence parameter $\lambda = 0.67^{+0.19}_{-0.17}(stat) \pm 0.18(syst)$. The above-mentioned values are consistent within errors with results for other reference distributions.

The above results, together with earlier LEP results, establish a strong decrease of R with the increase in hadron mass. Currently, there are three known models which aim at understanding of this effect: semi-classical derivations based on the Heisenberg relations or the virial theorem and a quantum-mechanical model based on the Björken-Gottfried condition, proposed by A. Białas and K. Zalewski.

The first two explanations predict that hadrons are emitted from sources with radii strongly dependent on the mass. This makes the energy density of the source emitting protons or Λ's unacceptably high. In the third approach to understand the dependence of the correlation radius on hadron mass, i.e. the model by A. Białas and K. Zalewski, the radius of the particle source is universal, being in fact the apparent radius, which is smaller than the real particle emission radius.

Calculations within this model are presented in the last part of this thesis. The correlation function dependencies on $Q_\perp$ and $Q_{||}$ have been derived. On the basis of them the predicted values of correlation radii $R_\perp$ and $R_{||}$ have been evaluated for different particles. The expected results of the model by A. Białas and K. Zalewski have been compared to the combined LEP measurements, providing an acceptable description of the correlation radius dependence on hadron mass. The observed anisotropy of the source shape ($R_{\parallel} > R_{\perp}$) is correctly reproduced by the model for pions and is predicted to diminish for higher masses. It is worthwhile to note that, contrary to semi-classical approaches, in the model by A. Białas and K. Zalewski the observed source radius is an apparent radius, being in fact smaller than the real one of particle emission volume.

Further studies are needed to gain a better understanding of the observed dependence of the correlation radius on hadron mass. One of the key issues is to achieve better precision of the correlation radius measurements. In particular, the determination of transversal and longitudinal components of the correlation radii for kaons, protons and Λ hyperons must be performed. This would allow for the verification of theoretical predictions.

Acknowledgements

First and foremost, I would like to express my gratitude to Dr. Henryk Pałka who has been supporting my efforts through all the years from the concept of this analysis till the final version of my manuscript. I would also like to make acknowledgement to his valuable assistance in dealing with everyday issues in the field of physics and helping me to extend my scientific experience.

I am very fortunate to have had an opportunity to work with Prof. Andrzej Białas who has inspired my work and supported it financially with his private subsidy. I want to express my utmost gratitude both to him and Prof. Kacper Zalewski who have encouraged the pursuit of this analysis. I am greatly indebted to them for theoretical support and many stimulating discussions.

My special thanks go to Assoc. Prof. Tadeusz Lesiak for his assistance in promoting my thesis as well as constant professional attention to my work and its progress.

I would like to express my appreciation to Dr. Jan Timmermans for his kindness and continuous interest in my work.

Last but not least, I would like to thank all members of the DELPHI Collaboration for the friendly atmosphere and their significant effort in data collection. In particular I am grateful to Nick van Remortel and Pedro Abreu for their help in solving various problems encountered. Many special thanks go to my friends from the Department of Leptonic Interactions INP PAS with whom I had the privilege to collaborate.

The work has been partially supported by the Subsidy FNP 1/99 as well as by the Polish State Commitee for Scientific Research (KBN) Grants Nos 620/E-77/SPUB/CERN/P-03/DZ 3/99 and 620/E-77/SPUB-M/CERN/P-03/DZ 297/2000.

List of Figures

List of Tables

Bibliography

[1] R. Hanbury Brown and R. Q. Twiss, Phil. Mag. **45** (1954) 663.
[2] R. Hanbury Brown and R. Q. Twiss, Nature **177** (1956) 27.
[3] R. Hanbury Brown and R. Q. Twiss, Nature **178** (1956) 1046.
[4] R. K. Ellis, W. J. Stirling and B. R. Webber, *QCD and Collider Physics*, Cambridge Monographs on Particle Physics, Nuclear Physics and Cosmology, ISBN: 0521 58189 3.
[5] G. Baym, Acta Phys. Pol. **B29** (1998) 1839.
[6] G. Goldhaber, W. B. Fowler, S. Goldhaber, T. F. Hoang, Phys. Rev. Lett. **3** (1959) 181.
[7] G. Goldhaber, S. Goldhaber, W. Y. Lee and A. Pais, Phys. Rev. **120** (1960) 300.
[8] W. Kittel, Acta Phys. Pol. **B32** (2001) 3927.
[9] G. Alexander, Rept. Prog. Phys. **66** (2003) 481.
[10] M. G. Bowler, Phys. Lett. **B180** (1986) 229; ibid. **B185** (1987) 205.
[11] B. Andersson, W. Hofmann, Phys. Lett. **B169** (1986) 364.
[12] B. Andersson, Acta Phys. Pol. **B32** (2001) 3993.
[13] B. Andersson and M. Ringner, Nucl. Phys. **B513** (1998) 627.
[14] B. Andersson and M. Ringner, Phys. Lett. **B421** (1998) 283.
[15] T. Sjöstrand (CERN), preprint CERN-TH-6488-92 (1992) 284.
[16] T. Sjöstrand, Comp. Phys. Comm. **27** (1982) 243; ibid. **28** (1983) 229.
[17] T. Sjöstrand and M. Bengtsson, Comp. Phys. Comm. **43** (1987) 367.
[18] A. Bialas and A. Krzywicki, Phys. Lett. **B354** (1995) 134.
[19] S. Chapman, P. Scotto and U. Heinz, Heavy Ion Physics 1 (1995) 1.
[20] A. Bialas and K. Zalewski, Eur. Phys. J. **C6** (1999) 349; Phys. Lett. **B436** (1998) 153.
[21] H. Gyulassy, S. Kauffmann and L. W. Wilson, Phys. Rev. **C20** (1979) 2267.
[22] S. Pratt, Phys. Rev. Lett. **53** (1984) 1219.
[23] S. Pratt, T. Csörgo and J. Zimanyi, Phys. Rev. **C42** (1990) 2646.
[24] P. Carruthers and F. Zachariasen, Rev. Mod. Phys. **55** (1983) 245.
[25] E. P. Wigner, Phys. Rev. **40** (1932) 749.
[26] M. Hillery, R. F. O'Connel, M. O. Scully and E. P. Wigner, Phys. Rep. **106** (1984) 121.
[27] B. Lörstad, Int. J. Mod. Phys. A4 **12** (1989) 2861.
[28] S. Haywood, *Where are we going with Bose-Einstein—a Mini Review*, RAL Report **RAL-94-074** (1995).
[29] H. Aihara et al., (TPC Coll.), Phys. Rev. **D31** (1985) 996.
[30] H. Althoff et al., (TASSO Coll.), Z. Phys. **C30** (1986) 35.
[31] I. Juricic et al., (Mark II Coll.), Phys. Rev. **D39** (1989) 1.

[32] P. Abreu et al., (DELPHI Coll.), Z. Phys. **C73** (1996) 11.
[33] U. Heinz, *Hanbury Brown - Twiss interferometry for relativistic heavy ion collisions: theoretical aspects*, Proc. of Int. Summer School on Correlations and Clustering Phenomena in Subatomic Physics, Dronten, Netherlands (1996) 137.
[34] K. Geiger et al., Phys. Rev. **D61** (2000) 054002.
[35] T. Csörgo and S. Pratt, Proc. of the Budapest Workshop on Relativistic Heavy Ion Physics at Present and Future Accelerators, edited by T. Csörgo et al., CRIP preprint KFKI-1991-28/A (1991) 75.
[36] M. Gyulassy et al., Phys. Rev. **C20** (1979) 2267.
[37] M. Biyajima et al., Phys. Lett. **B353** (1995) 340.
[38] http://aleph.web.cern.ch/aleph/
[39] http://delphiwww.cern.ch/index.html
[40] http://l3.web.cern.ch/l3/
[41] http://opal.web.cern.ch/Opal/PPwelcome.html
[42] D. Decamp et al., (ALEPH Coll.), Z. Phys. **C54** (1992) 75.
[43] P. Abreu et al., (DELPHI Coll.), Phys. Lett. **B286** (1992) 201.
[44] P. Achard et al., (L3 Coll.), Phys. Lett. **B524** (2002) 55.
[45] G. Alexander et al., (OPAL Coll.), Z. Phys. **C72** (1996) 389.
[46] G. Abbiendi et al., Phys. Lett. **B559** (2003) 131.
[47] P. Abreu et al., (DELPHI Coll.), Phys. Lett. **B379** (1996) 330.
[48] G. Abbiendi et al., (OPAL Coll.), Eur. Phys. J. **C21** (2001) 23.
[49] D. Buskulic et al., (ALEPH Coll.), Z. Phys. **C64** (1994) 361.
[50] S. Schael et al., (ALEPH Coll.), preprint CERN-PH-EP/2004-033, submitted to Phys. Lett. **B**.
[51] R. Akers et al., (OPAL Coll.), Z. Phys. **C67** (1995) 389.
[52] OPAL Coll., preprint CERN-EP/2001.
[53] R. Barate et al., (ALEPH Coll.), Phys. Lett. **B475** (2000) 395.
[54] T. Lesiak, H. Palka, preprint CERN-EP/98-114.
[55] G. Alexander et al., (OPAL Coll.), Phys. Lett. **B384** (1996) 377.
[56] H. J. Lipkin, Phys. Lett. **B219** (1989) 474.
[57] A. Heister et al., (ALEPH Coll.), Eur. Phys. J. **C36** (2004) 147.
[58] P. Abreu et al., (DELPHI Coll.), Phys. Lett. **B471** (2000) 460.
[59] M. Acciarri et al., (L3 Coll.), Phys. Lett. **B458** (1999) 517.
[60] G. Abbiendi et al., (OPAL Coll.), Eur. Phys. J. **C16** (2000) 423.
[61] S. Y. Lee, *Accelerator Physics*, World Scientific Pub Co, ISBN: 981023709.
[62] S. Myers, *The LEP collider from design to approval and commissioning*, Proceedings of CERN Accelerator School, CERN yellow report 91-08.
[63] S. Glashow, Nucl. Phys. **B22** (1961) 579.
[64] S. Weinberg, Phys. Rev. Lett. **19** (1967) 1264.
[65] http://public.web.cern.ch/Public/Content/Chapters/AboutCERN/CERNFuture/WhatLHC/WhatLHC-en.html
[66] P. Aarnio et al., (DELPHI Coll.), Nucl. Instr. and Meth. **A303** (1991) 223.
[67] P. Abreu et al., (DELPHI Coll.), Nucl. Instr. and Meth. **A378** (1996) 57.
[68] M. Battaglia, P. Kluit, preprint CERN-EP/96-133.
[69] Z. Albrecht, M. Feindt and M. Moch, preprint CERN-EP/99-150 (1999).
[70] *DELANA User's Guide*, note DELPHI 89-44/PROG 137 (1989).
[71] *TANAGRA User's Guide*, note DELPHI 87-95/PROG 98 (1989).

[72] *DELSIM User Manual*, note DELPHI 87-96/PROG 99 (1989).
[73] T. Sjöstrand, Comp. Phys. Comm. **82** (1994) 74.
[74] M. Kucharczyk, T. Lesiak and H. Palka (DELPHI Coll.), note DELPHI 2003-064 CONF-681.
[75] Private correspondence with A. Białas.
[76] F. James and M. Goosens, *MINUIT, Function Minimalization and Error Analysis, Reference Manual*, CERN Program Library Long Writeup **D506** (1992).
[77] A. Apostolakis et al., (CPLEAR Coll.), Eur. Phys. J. **C18** (2000) 41.
[78] N. van Remortel et al., *Bose-Einstein Correlations in W^+W^- events at LEP2*, DELPHI 2003-058 CONF 678.
[79] M. Kucharczyk and H. Palka (DELPHI Coll.), note DELPHI 2004-003 CONF-684.
[80] M. Kucharczyk and H. Palka (DELPHI Coll.), note DELPHI 2004-038 CONF-713.
[81] M. Kucharczyk, *Fermi-Dirac correlations in $Z^0 \to ppX$*, Proceedings to 39th Rencontres de Moriond on QCD and High-Energy Hadronic Interactions, La Thuile, Italy, 28 Mar - 4 Apr 2004.
[82] OPAL Coll., preprint CERN-EP/2001.
[83] G. Alexander, I. Cohen and E. Levin, Phys. Lett. **B452** (1999) 159.
[84] A. Bialas and K. Zalewski, Acta. Phys. Pol. **B30** (1999) 359.
[85] A. Bialas, M. Kucharczyk, H. Palka, K. Zalewski, Phys Rev. **D62** (2000) 114007.
[86] A. Bialas, M. Kucharczyk, H. Palka, K. Zalewski, Acta Phys. Pol. **B32** (2001) 2901.
[87] C. Cohen-Tannoudji, B. Diu and F. Laloë, *Quantum Mechanics*, John Wiley and Sons publ. Co., 1990.
[88] Ya. I. Azimov, Y. L. Dokshitzer, V. A. Khoze and S. I. Troyan, Z. Phys. **C27** (1985) 65.
[89] V. A. Khoze and W. Ochs, Int. J. Mod. Phys. **A12** (1997) 2949.
[90] Ya. I. Azimov et al., Z. Phys. **C13** (1986) 213.
[91] M. R. Ahmady, R. R. Mendel and J. D. Talman, Phys. Rev. **D55** (1997) 419.
[92] K. Gottfried, Acta Phys. Pol. **B3** (1972) 769; Phys. Rev. Lett. bf 32 (1974) 957.
[93] F. E. Low and K. Gottfried, Phys. Rev. **D17** (1978) 2487.
[94] J. D. Björken, Phys. Rev. **D7** (1973) 282, ibid. **D27** (1983) 140.
[95] X. Artru and G. Menessier, Nucl. Phys. **B70** (1974) 93.
[96] B. Andersson et al., Phys. Rep. **97** (1983) 31.
[97] T. Csörgo, Phys. Lett. **B347** (1995) 354.
[98] S. Pratt, Phys. Rev. Lett. **53** (1984) 13.